

DISS. ETH NO. 28032

EXTENDED LATTICE BOLTZMANN MODELS  
FOR GAS DYNAMICS

A thesis submitted to attain the degree of  
DOCTOR OF SCIENCES of ETH ZURICH  
(Dr. sc. ETH Zurich)

presented by  
MOHAMMAD HOSSEIN SAADAT  
MSc in Aerospace Engineering,  
Sharif University of Technology

born on 18.08.1990  
citizen of Iran

accepted on the recommendation of  
Prof. Dr. Ilya. V. Karlin, examiner  
Prof. Dr. Patrick Jenny, co-examiner  
Prof. Dr. Kai Luo, co-examiner  
Dr. Benedikt Dorschner, co-examiner

2021



To my parents





## ABSTRACT

---

The lattice Boltzmann method (LBM) is a powerful alternative paradigm in computational fluid dynamics, based on a Boltzmann-type kinetic equation on a discrete velocity set. While LBM has seen rapid developments in the past three decades, its success has been mainly limited to a subclass of incompressible flows, with applications ranging from turbulence to multi-phase and multi-component flows, and has only partially succeeded in the compressible high Mach number regime. In particular, conventional lattice Boltzmann models for the simulation of fluid dynamics are restricted by an error in the stress tensor that is negligible only for small flow velocity and at a singular value of the temperature, thus preventing LBM from going to higher velocities as well as incorporating temperature dynamics. In this context, the aim of this thesis is to address this issue and develop extended lattice Boltzmann models that enable high-fidelity simulations of fundamental and engineering applications in thermal and compressible regime.

Two extended compressible lattice Boltzmann models on standard lattices are realized within the two-population framework by introducing appropriate correction terms into the kinetic equations. It is shown that resulting models restore the full Navier–Stokes–Fourier equations with adjustable Prandtl number and adiabatic exponent in the hydrodynamic limit. The operating range of models is then extended to supersonic flows involving shock waves following two strategies, namely the use of shifted lattices and upwind discretization of correction terms. The former, results in a wider operating domain; however, comes at the price of losing the exact on-lattice propagation. The latter, maintains the accuracy and simplicity of on-lattice propagation, but is only applicable to moderately supersonic flows.

The model formulation is then extended to fully unstructured body-fitted meshes for handling complex geometries. To that end, semi-Lagrangian propagation is performed on a second-order finite element mesh. The model is studied extensively for different benchmark simulations including subsonic/supersonic flow over NACA0012 airfoil and shock-vortex interaction in Schardin’s problem.

The applicability of the extended compressible model is studied for the simulation of moving objects by employing the so-called Arbitrary Lagrangian-Eulerian (ALE) technique. Important applications such as plunging/pitching

airfoil with different amplitudes and frequencies are thoroughly investigated.

Finally, the predictive capabilities of the newly developed model are demonstrated by a thorough investigation of a compressible turbulent flow. Simulation of decaying of compressible homogeneous isotropic turbulence is conducted and the results are compared with the direct numerical simulation (DNS) results. A good agreement in the statistics of mean and fluctuating variables is observed and it is demonstrated that the present model provides an accurate representation of compressible flows, even in the presence of turbulence and shock waves.

To conclude, the promising results of the proposed models on standard lattices with a minimal number of discrete speeds, open interesting prospects towards the numerical simulation of more complex industrial applications in compressible regime.

## ZUSAMMENFASSUNG

---

Die Gitter-Boltzmann-Methode (LBM) ist ein leistungsfähiges alternatives Paradigma in der numerischen Strömungsmechanik, das auf einer kinetischen Gleichung vom Boltzmann-Typ auf einem diskreten Geschwindigkeitssatz basiert. Während LBM in den letzten drei Jahrzehnten eine rasante Entwicklung erlebt hat, beschränkte sich sein Erfolg hauptsächlich auf eine Unterklasse inkompressibler Strömungen mit Anwendungen, die von Turbulenzen bis hin zu Mehrphasen- und Mehrkomponentenströmungen reichen, und war nur teilweise erfolgreich bei der kompressiblen hohen Mach Zahlenregime. Insbesondere konventionelle Gitter-Boltzmann-Modelle zur Simulation der Strömungsdynamik werden durch einen nur bei kleinen Strömungsgeschwindigkeiten und einem singulären Temperaturwert vernachlässigbaren Fehler des Spannungstensors eingeschränkt und verhindern so, dass LBM auf höhere Geschwindigkeiten sowie Temperaturdynamik einbeziehen. In diesem Zusammenhang ist es das Ziel dieser Dissertation, dieses Problem anzugehen und ein erweitertes Gitter-Boltzmann-Modell zu entwickeln, das High-Fidelity-Simulationen von grundlegenden und technischen Anwendungen in thermischen und kompressibles Regime.

Zwei erweiterte kompressible Gitter-Boltzmann-Modelle auf Standardgittern werden innerhalb des Zwei-Populations-Frameworks realisiert, indem entsprechende Korrekturterme in die kinetischen Gleichungen eingeführt werden. Es wird gezeigt, dass die resultierenden Modelle die vollständigen Navier-Stokes-Fourier-Gleichungen mit einstellbarer Prandtl-Zahl und adiabatischem Exponenten im hydrodynamischen Limes wiederherstellen. Der Arbeitsbereich der Modelle wird dann auf Überschallströmungen mit Stoßwellen erweitert, wobei zwei Strategien verfolgt werden, nämlich die Verwendung von verschobenen Gittern und die Diskretisierung von Korrekturtermen gegen den Wind. Ersteres führt zu einem breiteren Betriebsbereich; Dies geht jedoch um den Preis, dass die genaue Ausbreitung auf dem Gitter verloren geht. Letzteres behält die Genauigkeit und Einfachheit der Ausbreitung auf dem Gitter bei, ist jedoch nur auf Strömungen mit mäßigem Überschall anwendbar.

Die Modellformulierung wird dann auf vollständig unstrukturierte körperangepasste Netze zur Handhabung komplexer Geometrien erweitert. Zu diesem Zweck wird eine semi-Lagrangesche Ausbreitung auf einem Finite-Elemente-Netz zweiter Ordnung durchgeführt. Das Modell wird ausführ-

lich für verschiedene Benchmark-Simulationen untersucht, einschließlich Unterschall-/Überschallströmung über NACA0012-Profil und Stoß-Wirbel-Interaktion im Scharadin-Problem.

Die Anwendbarkeit des erweiterten kompressiblen Modells wird für die Simulation bewegter Objekte untersucht, indem die sogenannte Arbitrary Lagrangean-Eulerian (ALE)-Technik verwendet wird. Wichtige Anwendungen wie Tauch-/Pitching-Profil mit unterschiedlichen Amplituden und Frequenzen werden eingehend untersucht.

Schließlich werden die Vorhersagefähigkeiten des neu entwickelten Modells durch eine gründliche Untersuchung eines kompressiblen turbulenten Problems demonstriert. Die Simulation des Zerfalls kompressibler homogener isotroper Turbulenzen wird betrachtet und die Ergebnisse werden mit den Ergebnissen der direkten numerischen Simulation (DNS) verglichen. Es wird eine gute Übereinstimmung in der Statistik der mittleren und fluktuierenden Variablen beobachtet und es wird gezeigt, dass das vorliegende Modell eine genaue Darstellung kompressibler Strömungen liefert, selbst in Gegenwart von Turbulenzen und Stoßwellen.

Zusammenfassend eröffnen die vielversprechenden Ergebnisse der vorgeschlagenen Modelle zu Standardgittern interessante Perspektiven für die numerische Simulation komplexerer industrieller Anwendungen im kompressiblen Bereich.

## ACKNOWLEDGEMENTS

---

First and foremost, I would like to thank my PhD supervisor, Prof. Dr. Ilya Karlin without whom this thesis could never have been accomplished. I want to thank him for giving me the opportunity to join his group and for always believing in me. I am hugely grateful for his wise guidance and insight, his enthusiasm for ideas, and his continuous support and encouragement throughout the entire thesis.

I am also immensely grateful to Dr. Benedikt Dorschner and Dr. Fabian Bösch for their help, enthusiasm and invaluable contributions. Fabian's help and guidance at the early stage of this work were specially important.

I would also like to thank Prof. Dr. Patrick Jenny and Prof. Dr. Kai Luo for accepting to be part of my PhD thesis committee and for reading and reviewing my work.

Special thanks go to a number of friends and colleagues, with whom I was able to have a great time at the office: Ehsan Reyhanian, Nilesh Sawant, Nikolaos Kallikounis, Seyed Ali Hosseini and Abhimanyu Bhadauria. Many thanks to Ali, Nilesh and Nikos for the good times we spent together and for interesting talks and discussions. Also, I want to thank all my friends outside ETH that have been around me, and with them I have enjoyed spending time.

Last but not least, a special thank goes to my family for their never ending love, unconditional support and patience.

The work presented in this thesis was accomplished in the computational kinetics group, at the Swiss Federal Institute of Technology (ETH Zürich), Switzerland, under the financial support of the ETH research Grant No. ETH-13 17-1 and the European Research Council (ERC) Advanced Grant No. 834763-PonD. The computational resources at the Swiss National Super-Computing Center CSCS were provided under Grant No. s897.

Zürich, December 2021

Mohammad Hossein Saadat



# CONTENTS

---

1	INTRODUCTION	1
1.1	Outline of thesis	3
2	LATTICE KINETIC THEORY	7
2.1	The Boltzmann equation	7
2.1.1	Equilibrium distribution and local Maxwellian	9
2.1.2	$\mathcal{H}$ -Theorem	10
2.1.3	BGK approximation of collision term	10
2.1.4	Kinetic simulation approaches	11
2.2	Lattice Boltzmann method	13
2.2.1	Velocity space discretization	13
2.2.2	Space-time discretization	14
2.2.3	Basic features of the standard LBM	15
2.2.4	Lattice Boltzmann models for compressible flows	16
3	EXTENDED LATTICE BOLTZMANN MODELS FOR COMPRESSIBLE FLOWS	19
3.1	Introduction	19
3.2	Kinetic equations	20
3.2.1	Moment requirements	21
3.2.2	Discrete velocities, factorization and anomaly of the standard lattices	23
3.3	Extended compressible model I	25
3.3.1	Hydrodynamic limit	28
3.3.2	Equations of gas dynamics	32
3.3.3	Summary of the extended model I	33
3.3.4	Numerical validation	34
3.4	Extended compressible model II	38
3.4.1	Hydrodynamic limit	43
3.4.2	Equations of gas dynamics	47
3.4.3	Summary of the extended model II	48
3.4.4	Numerical validation	49
3.4.5	Application of extended equilibrium to incompressible iso-thermal flows	50
3.5	Conclusion	64
4	EXTENSION TO SUPERSONIC FLOWS	67
4.1	Introduction	67

4.2	Concept of the shifted lattices	67
4.2.1	Shock-vortex interaction	70
4.3	Upwind discretization of correction term in model II	72
4.3.1	Shock-vortex interaction with on-lattice model II	74
4.4	Conclusion	74
5	UNSTRUCTURED AND MOVING MESHES	77
5.1	Introduction	77
5.2	Semi-Lagrangian propagation	78
5.2.1	Wall boundary conditions	80
5.2.2	Numerical results	82
5.3	Arbitrary Lagrangian Eulerian approach for moving geometries	90
5.3.1	ALE formulation of LBM	93
5.3.2	Geometric conservation law	96
5.3.3	Numerical results	97
5.4	Conclusion	109
6	COMPRESSIBLE TURBULENT SIMULATIONS	111
6.1	Introduction	111
6.2	Decaying of compressible homogeneous isotropic turbulence	112
6.3	Conclusion	122
7	KINETIC THEORY IN A CO-MOVING REFERENCE FRAME: A PROMISING APPROACH	125
7.1	Introduction	125
7.2	Kinetic theory in a co-moving reference frame	125
7.3	The shock structure problem	128
7.4	Conclusion	131
8	SUMMARY AND FUTURE WORKS	133
8.1	Summary	133
8.2	Future works	135
A	APPENDIX	137
A.1	Comparison of extended LBGK to locally corrected LBM [44]	137
A.2	Transfer matrix for equilibrium populations with D2Q9 lattice	143
	List of Tables	145
	List of Figures	146
	BIBLIOGRAPHY	154



## INTRODUCTION

---

*[In science] each paradigm will be shown to satisfy more or less the criteria that it dictates for itself and to fall short of a few of those dictated by its opponent!*

— Thomas Kuhn

Fluids are everywhere. We are living in a world where applications related to fluid dynamics play a crucial role in important areas such as health, energy, transportation, defense, etc. A classical model for description of fluid dynamics is called the Navier-Stokes (NS) equations, for which no analytical solutions are present except for very specific simple configurations. Consequently, the study of fluid dynamics was mostly experimental and theoretical until 1960s, when the rise of powerful computers made it possible to carry out complex numerical simulations. This marks the beginning of computational fluid dynamics (CFD) as a discipline which aims at developing numerical algorithms capable of capturing flow physics with good accuracy and efficiency. Ever since, CFD has been a complementary tool in understanding the physics of fluid flows as well as in engineering design [1].

Developing accurate and efficient numerical schemes, however, is not an easy task due to non-linear nature of NS equations. Such challenges are prominent in compressible flows with shock waves in the flow field. Shock waves are sharp discontinuities of the flow properties across a thin region with the thickness of the order of mean free path. Since in practical simulations, it is impossible to use a grid size fine enough to resolve the physical shock structure defined by the molecular viscosity, most numerical schemes rely on some numerical dissipation to stabilize the simulation and capture the shock over a few grid points [2, 3].

Another computational complexity emerges when the flow becomes turbulent. Turbulence is of great importance in many flows of practical interests and is characterized by the presence of a wide range of length and time scales in the flow. One approach to turbulence is direct numerical simulation (DNS), which resolves all time and length scales in turbulent flows. However, the severe computational cost limits this method to fundamental applications with simple geometries. On the other hand, the Reynolds–

Average–Navier–Stokes (RANS) is the approach most commonly used in the industry, where turbulence models are used to mimic the effect of the entire turbulence spectrum on the mean flow field. Large eddy simulation (LES) is an alternative approach to DNS and RANS, which exploits the universal behaviour of small scales in turbulent flows in order to reduce the computational requirement of DNS. In LES, a low–dissipative flow solver is typically used to resolve the large scales in the flow field, while a proper subgrid model is employed to model the effect of small (subgrid) scales on large scales. LES is now a promising tool for the simulation of realistic flows in industrial scale.

Out of this context, the lattice Boltzmann method (LBM) emerged as an alternative to conventional CFD solvers, with its first realization in 1988 [4, 5]. Historically, LBM developed independently from the Boltzmann equation, through a method called the lattice gas automata (LGA) [6, 7]. LGA was a particle based flow solver, where particles were allowed to move on discrete lattices and collide locally. LBM was able to remove the statistical noise of LGA, by replacing discrete particles with the so-called particle distribution function. However, it was later shown that LBM can also be viewed as a discretization of the Boltzmann equation at discrete velocities correspond to the roots of the Hermite polynomials (Gauss–Hermite quadratures) [8–10]. Since its inception, LBM has been proved to be a viable and efficient tool for the simulation of complex fluid flows [11–13] and has been applied to a wide range of fluid dynamics problems including, but not limited to, turbulence [14–22], multi-phase and multi-component flows [23–27], flows in porous media [28–30], acoustics [31–33], magnetohydrodynamics [12, 34–36] and relativistic hydrodynamics [37–39]. The attractiveness of the LBM over conventional CFD methods, lies in the simplicity and locality of its underlying numerical algorithm, which can be summarized as "stream populations  $f_i(\mathbf{x}, t)$  along the discrete velocities  $\mathbf{c}_i$  and equilibrate at the nodes  $\mathbf{x}$ ". The simple *streaming and collision* algorithm of the standard LBM, makes it a good candidate for parallel implementation and high performance computing, as in each time step only the information of nearest neighboring nodes is required. Furthermore, the kinetic nature of LBM, opens the possibility of designing implicit turbulence models in under-resolved scenarios, thus avoids the need of explicit turbulence models. As such, LBM is now entering the mainstream engineering practice [40–43].

In spite of all these advantages of the LBM, it is well known that LBM on standard lattices ( $D2Q9$  in two dimensions and  $D3Q27$  in three dimensions). Here, the  $DdQn$  model refers to  $d$  dimension model with  $n$  discrete speeds)

faces stiff challenges in dealing with high-speed flows [44] and its success has been mainly limited to low-speed incompressible flow applications. Development of LB models for compressible flows is a somewhat recent effort. Multiple models have been proposed and employed in the literature to extend the operating range of LBM to high-speed compressible flows. Nevertheless, an accurate LB model on standard lattices capable of capturing the complex physics of compressible flows involving shock waves is still needed. This PhD thesis will address this issue with the aim of developing a LB framework on standard lattices which enables high-fidelity simulations of fundamental and engineering applications in thermal and compressible regime.

## 1.1 OUTLINE OF THESIS

The present thesis is organized as follows:

- Chapter 2: Mathematical and physical foundations of the kinetic theory of gases and the Boltzmann equation along with a detailed derivation of the lattice Boltzmann method are presented. Then, an overview over the existing compressible lattice Boltzmann models in the literature is provided.
- Chapter 3: Two extended lattice Boltzmann models for compressible flows on standard lattices are presented. Both models are based on the idea of introducing correction terms into the kinetic equations within the two-population framework. They are different in the implementation of correction terms as well as construction of the energy equilibrium distribution function. It is shown that both models are isotropic, Galilean invariant and can recover the full Navier–Stokes–Fourier equations with adjustable Prandtl number and adiabatic exponent in the hydrodynamic limit. In the last part of the chapter, the benefits of using the extended model in the incompressible iso-thermal regime is briefly discussed.
- Chapter 4: Possibilities of extending the operating range of the models developed in Chapter 3 to supersonic flows involving shock waves, are investigated following two ideas. The first one is the concept of the shifted lattices, which relies on formulating the kinetic equations in a reference frame moving with a constant predefined velocity. The second one is based on a proper discretization of spatial derivatives in

the correction term in order to provide enough numerical dissipation for removing nonphysical oscillations. Sound generation in shock-vortex interaction is simulated for validation.

- Chapter 5: The model formulation is extended to fully unstructured body-fitted mesh over complex geometries using the semi-Lagrangian propagation with a second-order accurate finite-element interpolation to reconstruct solution at the grid points. This type of propagation not only removes the restriction related to the regular lattice, but is less dissipative compared to other off-LB schemes (such as finite-difference or finite-volume LB schemes). Consistent boundary conditions based on the Grad's approximation is then implemented and the model is tested and validated through simulation of different benchmarks, including subsonic and supersonic flow over airfoil and shock-vortex interaction in Schardin's problem.

In the next step, we extend the applicability of the proposed model for the simulation of moving objects. This is achieved by employing the so-called Arbitrary Lagrangian-Eulerian method, which has the advantage of handling moving and deforming objects with body-fitted mesh. Interesting applications such as plunging/pitching airfoil with different amplitudes and frequencies are thoroughly investigated.

- Chapter 6: The accuracy and performance of the extended model in dealing with compressible turbulent flows is investigated through simulation of decaying of compressible homogeneous isotropic turbulence. This challenging test-case can be considered as a rigorous test for the validity of the present model, as it contains both compressibility effects and shocks, as well as turbulent structures in the flow field. Different scenarios with different turbulent Mach number and Reynolds number are thoroughly investigated and it is demonstrated that the model is able to accurately predict the relevant features of compressible turbulent flows even at high turbulent Mach number, where eddy-shocklets exist in the flow field and interact with turbulence.
- Chapter 7: Preliminary results of a new representation of the kinetic theory named particles-on-demand (PonD) method are presented. The distinctive feature of PonD is that the kinetic equations are formulated in the local co-moving reference frame in which the local equilibria do not depend on flow velocity and temperature. This makes the PonD a suitable candidate for simulation of high-speed nonequilibrium flows,

since there is no error proportional to fluid velocity in the equilibrium moments. To demonstrate that, the classical shock structure problem is considered and it is shown that PonD is able to resolve the structure of shock wave with reasonable accuracy.



## LATTICE KINETIC THEORY

*The true logic of this world is in the calculus of probabilities.*

— James C. Maxwell

The aim of this chapter is, first, to provide basic mathematical and physical foundations of the kinetic theory of gases and the Boltzmann equation. Interested readers are referred to Chapman & Cowling [45], Cercignani, Illner & Pulvirenti [46], Villani [47], and Grad [48] for a detailed discussion on the Boltzmann equation. The chapter will then go by introducing the essential components of the lattice Boltzmann method. Finally, the limitations and challenges of LBM in the compressible regime is discussed and a review of existing compressible LB models is given.

## 2.1 THE BOLTZMANN EQUATION

Kinetic theory deals with modeling of the systems (e.g., a gas) made up of large number of particles. Since describing the dynamics of all individual particles is a formidable task, kinetic theory is based on the concept of a distribution function, i.e., large particle ensembles in terms of a phase space. The phase space includes macroscopic variables (the position in physical space) and also microscopic variables, which describe the “state” of the particles [47]. That is why kinetic models are sometimes called mesoscopic models, as they lie between microscopic models and macroscopic or continuum models that describe a material with a finite number of macroscopic quantities [49]. The whole goal of kinetic theory is, then, to find out the equations, typically integro-differential equations, that govern the evolution of the distribution function in time.

Suppose, we have a system of dilute gas with  $\mathcal{N}$  particles, in thermal equilibrium. The “state” of the particles can be described by specifying particles’ position  $\mathbf{x} = (x, y, z)$  and velocity  $\mathbf{c} = (c_x, c_y, c_z)$  at any given time  $t$ . The distribution function is denoted by  $f(\mathbf{x}, \mathbf{c}, t)$ . Intuitively,  $f(\mathbf{x}, \mathbf{c}, t)d\mathbf{x}d\mathbf{c}$  represents the number of particles within the infinitesimal control volume of size  $d\mathbf{x}d\mathbf{c}$  (i.e., with position within the range  $\mathbf{x}$  and  $\mathbf{x} + d\mathbf{x}$  and velocity

in the range  $c$  and  $c + dc$ , at time  $t$ . Consequently, the total number of particles in the system can be computed as,

$$\mathcal{N} = \iiint f(\mathbf{x}, \mathbf{c}, t) d\mathbf{x} d\mathbf{c}. \quad (2.1)$$

The distribution function  $f$  also allows us to express hydrodynamic quantities as "moments" of the  $f$ . For example, the local density  $\rho$ , momentum  $\rho u$  and energy  $\rho E$  are zeroth-, first- and second-order moments of the distribution function, respectively,

$$\rho(\mathbf{x}, t) = \int f(\mathbf{x}, \mathbf{c}, t) d\mathbf{c}, \quad (2.2)$$

$$\rho u(\mathbf{x}, t) = \int \mathbf{c} f(\mathbf{x}, \mathbf{c}, t) d\mathbf{c}, \quad (2.3)$$

$$\rho E(\mathbf{x}, t) = \int \frac{c^2}{2} f(\mathbf{x}, \mathbf{c}, t) d\mathbf{c}. \quad (2.4)$$

With the concept of the distribution function in hand, the task is to find the time evolution of  $f$ , given the proper initial and boundary conditions.

We first consider the case with no interaction between particles, i.e., no collision. The conservation of particles within the control volume  $d\mathbf{x} d\mathbf{c}$  requires that,

$$f(\mathbf{x}, \mathbf{c}, t) d\mathbf{x} d\mathbf{c} = f(\mathbf{x} + \mathbf{c}\delta t, \mathbf{c} + \mathbf{F}\delta t, t + \delta t) d\mathbf{x} d\mathbf{c}, \quad (2.5)$$

where  $\mathbf{F}$  is an external force acting on the particles per unit mass. Considering the limit of infinitesimal time interval,  $\delta t \rightarrow 0$ , we can write the Taylor expansion of both sides,

$$\partial_t f(\mathbf{x}, \mathbf{c}, t) + \mathbf{c} \cdot \nabla_{\mathbf{x}} f(\mathbf{x}, \mathbf{c}, t) + \mathbf{F} \cdot \nabla_{\mathbf{c}} f(\mathbf{x}, \mathbf{c}, t) = 0, \quad (2.6)$$

where  $\partial_t = \frac{\partial}{\partial t}$ . This equation is sometimes called the *linear Vlasov* equation and describes the evolution of  $f$  under the action of the external force  $\mathbf{F}$ .

But the collision-less situation is far from the truth, as there certainly are collisions and the equilibration itself occurs due to collisions. We, therefore, re-write (2.6) as,

$$\partial_t f(\mathbf{x}, \mathbf{c}, t) + \mathbf{c} \cdot \nabla_{\mathbf{x}} f(\mathbf{x}, \mathbf{c}, t) + \mathbf{F} \cdot \nabla_{\mathbf{c}} f(\mathbf{x}, \mathbf{c}, t) = \Omega. \quad (2.7)$$

where  $\Omega$  is the collision operator and represents the net number of particles that leave/come into the control volume  $d\mathbf{x} d\mathbf{c}$  due to the collision. Boltzmann derived the collision operator under the following assumptions:



- Collisions are binary and elastic.
  - The velocities of two particles that are about to collide are uncorrelated.
- This assumption is also known as the *molecular chaos* assumption.

Without going into details, the collision operator can be written as an integral over particle velocities,

$$\Omega = \iiint \mathcal{W}(c'_1, c'_2 | c_1, c_2) [f(c'_1)f(c'_2) - f(c_1)f(c_2)] dc_2 dc'_1 dc'_2, \quad (2.8)$$

where  $\mathcal{W}(c'_1, c'_2 | c_1, c_2)$  is a probability that a pair of particles with initial velocity  $c_1$  and  $c_2$  changes its velocity to  $c'_1$  and  $c'_2$ , due to the scattering process. Consequently, it depends on the details about intermolecular forces.

Note that, without a loss of generality, we assume no external force (i.e.,  $F = 0$ ) in the remaining of this chapter.

### 2.1.1 Equilibrium distribution and local Maxwellian

If we take the distribution function  $f(x, c, t)$  and let it tend to infinity, then we get the equilibrium distribution  $f^{\text{eq}}(c)$ . As such, we expect the equilibrium distribution to be independent of time and position (in case without external force). Imposing these conditions on the Boltzmann equation (2.7) implies that,

$$\Omega = 0 \longrightarrow f^{\text{eq}}(c_2)f^{\text{eq}}(c_1) = f^{\text{eq}}(c'_2)f^{\text{eq}}(c'_1). \quad (2.9)$$

If we take the natural log of both sides,

$$\ln f^{\text{eq}}(c_1) + \ln f^{\text{eq}}(c_2) = \ln f^{\text{eq}}(c'_1) + \ln f^{\text{eq}}(c'_2). \quad (2.10)$$

This means that the log of equilibrium distribution is conserved during the scattering process. Therefore, equilibrium should be some function of conserved quantities (i.e., momentum and kinetic energy). This condition is satisfied by a class of functions of the form,

$$f^{\text{eq}} = \exp(\mathcal{X} + \xi \cdot c + \lambda c^2), \quad (2.11)$$

where  $\mathcal{X}$ ,  $\lambda$  and  $\xi$  are arbitrary constant scalars or vectors. There exist a physically relevant solution based on the constraints on the conserved moments, known as the *Maxwell-Boltzmann* distribution or the *local Maxwellian* distribution,

$$f^{\text{eq}}(c) = \rho \left( \frac{m}{2\pi k_B T} \right)^{(D/2)} \exp \left\{ -\frac{m(c - u)^2}{2k_B T} \right\}, \quad (2.12)$$

where  $D$  is the dimension of the physical space,  $m$  is the particles mass,  $T$  is the local temperature and  $k_B$  is the Boltzmann's constant.

### 2.1.2 $\mathcal{H}$ -Theorem

Boltzmann introduced a quantity  $\mathcal{H}$  defined as,

$$\mathcal{H}(f) = \int f \ln f d\mathbf{c}, \quad (2.13)$$

and proved the  $\mathcal{H}$ -Theorem in 1872 which states that  $\mathcal{H}$  always decreases with time, i.e.,

$$\frac{d\mathcal{H}}{dt} = \int \partial_t f [1 + \ln f] \leq 0. \quad (2.14)$$

This is one of the outstanding contributions of the Boltzmann to the statistical mechanics which provides a quantitative measure for the irreversibility and extends the concept of entropy to nonequilibrium processes, where the local entropy is defined as,

$$S(\mathbf{x}, t) = -k_B \mathcal{H}(\mathbf{x}, t). \quad (2.15)$$

Using (2.14) one can also observe that the equilibrium distribution happens when  $\frac{d\mathcal{H}}{dt} = 0$ .

### 2.1.3 BGK approximation of collision term

Given the complexity of the collision operator 2.8 in the Boltzmann equation, several approximations have been proposed. The most famous one was proposed by Bhatnagar, Gross and Krook [50] in 1954 based on the assumption that the main effect of the collision term is to bring the distribution function closer to the equilibrium distribution (2.12) [51]. The BGK collision term reads,

$$\Omega^{BGK} = \frac{1}{\tau} (f^{\text{eq}} - f), \quad (2.16)$$

where  $\tau$  is called the relaxation rate and can be interpreted as a characteristic time required for the relaxation towards the local Maxwellian. One can

also verify that the BGK operator satisfies the  $\mathcal{H}$ -theorem and also exactly conserves the mass, momentum and energy,

$$\frac{1}{\tau} \int (f^{\text{eq}} - f) d\mathbf{c} = 0, \quad (2.17)$$

$$\frac{1}{\tau} \int \mathbf{c} (f^{\text{eq}} - f) d\mathbf{c} = 0, \quad (2.18)$$

$$\frac{1}{\tau} \int \frac{c^2}{2} (f^{\text{eq}} - f) d\mathbf{c} = 0. \quad (2.19)$$

#### 2.1.4 Kinetic simulation approaches

Kinetic theory based on the Boltzmann equation can perfectly describe the dynamics of gas flows at all degrees of rarefaction. However, the high dimensionality of the particle distribution function and complex structure of the collision operator make use of the Boltzmann equation a non-trivial task. Different approaches have been proposed to deal with the Boltzmann equation. Two prominent examples are moment systems [see 52, 53] inspired by the idea of Grad [48] and the direct simulation Monte Carlo method [54].

##### 2.1.4.1 Grad's moments method

One approach, first introduced by Grad [48], is based on deriving moment systems of the Boltzmann equation (2.7),

$$\partial_t \left( \int \mathbf{\Psi}(\mathbf{c}) f(\mathbf{x}, \mathbf{c}, t) d\mathbf{c} \right) + \nabla \cdot \left( \int \mathbf{c} \mathbf{\Psi}(\mathbf{c}) f(\mathbf{x}, \mathbf{c}, t) d\mathbf{c} \right) = \left( \int \Omega \mathbf{\Psi}(\mathbf{c}) d\mathbf{c} \right), \quad (2.20)$$

where  $\mathbf{\Psi}(\mathbf{c})$  is a vector of polynomial functions of the velocity space variable  $\mathbf{c}$ . For example, the original 13-moment equations of Grad, include a coupled set of first-order partial differential equations for the evolution of density, momentum, stress tensor and heat flux vector. However, higher-order moments appear in the resulting system that need closure. The non-closed moments are computed by expanding the particle distribution functions in terms of Hermite polynomials. Following Grad's idea, several moment systems have been proposed in the literature, two prominent examples are the regularized 13-moment equations (R13) [52, 55, 56] and the maximum entropy closure [57]. Nevertheless, moment systems generally suffer from the limited hyperbolicity and moreover, the implementation of boundary conditions for higher-order moments (which lack physical

intuition) is not a straightforward task [58]. For a comprehensive review of moment methods see Torrilhon [53].

#### 2.1.4.2 *Direct simulation Monte Carlo*

Another approach for dealing with the Boltzmann equation is the direct simulation Monte Carlo (DSMC) method proposed by Bird [59], in which stochastic particles mimic the dynamics of the Boltzmann equation by undergoing propagation and collision steps. DSMC has been validated and successfully applied to a wide range of complex rarefied flows and it has been shown that its solution converges to that of the Boltzmann equation [60] in the limit of infinite particles. DSMC, however, loses its effectiveness in the low Mach number regime and also in flows near the continuum regime, where large number of particles are needed and time step size is restricted. The computational time of DSMC is, in general, 30 – 50 times more than that of solving the moment equations [61]. Recent studies have partly addressed these issues [see 62–65].

#### 2.1.4.3 *Chapman-Enskog method*

A famous approach to find a set of balance equations, for the hydrodynamic variables, resulting from the Boltzmann equation is called the Chapman-Enskog method. This method was developed in 1917 by Enskog [66] and Chapman [67]. In this method, the idea is to expand the distribution function as a power series of a smallness parameter  $\varepsilon$ ,

$$f = f^{(0)} + \varepsilon f^{(1)} + \varepsilon^2 f^{(2)} + \dots, \quad (2.21)$$

and substitute the expansion into the Boltzmann equation to obtain the solutions for different orders of  $\varepsilon$ . Considering the equations up to  $\varepsilon$  corresponds to the linear constitutive relations of the Navier–Stokes–Fourier equations for the stress tensor and heat flux vector. Using the Chapman-Enskog method, one can also derive higher-order constitutive relations, where the stress and heat flux are expressed in terms of higher-order gradients of the flow velocity and temperature [68]. However, the resulting Burnett and super-Burnett equations have been shown to be linearly unstable in both space and time [69].

Given that the Chapman-Enskog method will be thoroughly discussed in Chapter 3, it is not further detailed here.

## 2.2 LATTICE BOLTZMANN METHOD

In the past decades, as an alternative kinetic approach, the lattice Boltzmann (LB) method has received considerable attention for computational fluid dynamics and is now a versatile tool for simulation of complex fluid flows. While historically LB developed independently from the Boltzmann equation, it has been shown that, LB models can be viewed as a discretization of the Boltzmann equation at certain discrete velocities and the hierarchy of LB models can be considered as a way to approximate the Boltzmann equation [10] and thus, as an alternative to more standard approaches such as moment systems or DSMC.

### 2.2.1 Velocity space discretization

In the LBM, the continuous velocity space is first discretized into a finite number of velocity sets,

$$\mathcal{C} = \{c_1, c_2, \dots, c_Q\}, \quad (2.22)$$

where  $Q$  is the total number of discrete velocities. A corresponding distribution function (population) associated with each discrete velocity is then defined as,

$$\mathbf{f} = \{f_1, f_2, \dots, f_Q\}. \quad (2.23)$$

The discretized Boltzmann equation with the BGK collision for each population  $f_i$  can be written as,

$$\partial_t f_i(\mathbf{x}, t) + c_i \cdot \nabla f_i(\mathbf{x}, t) = \Omega_i^{BGK}. \quad (2.24)$$

The simplest choice of discrete velocities in one dimension is  $\mathcal{C} = \{-1, 0, +1\}$ , which is known as the standard lattice. In a higher dimension  $D$ , the discrete velocity set is constructed via tensor product of  $D$  copies of the one-dimensional velocity set. This will result in a well-known  $D2Q9$  lattice in 2D and  $D3Q27$  in 3D, which are most commonly used in the LB community for incompressible flow simulations.

Higher-order velocity sets can also be systematically constructed. One way to do that is through the roots of Hermite polynomials. In this method, the velocity set is defined as nodes of the high-order Gauss–Hermite quadrature [9]. Table 2.1 shows the discrete velocities (roots of Hermite polynomials), weights of the Gauss–Hermite quadrature  $W_{i\alpha}$  and also reference temperature  $T_L$  (which will be defined later) of three different lattice

models in one dimension, namely  $D1Q3$ ,  $D1Q4$  and  $D1Q5$ . The corresponding models in two dimensions are  $D2Q9$ ,  $D2Q16$  and  $D2Q25$ , respectively.

Quadrature	$c_{i\alpha}$	$W_{i\alpha}$
$D1Q3$ ( $T_L = 1/3$ )	0	2/3
	$\pm 1$	1/6
$D1Q4$ ( $T_L = 1.81649658$ )	$\pm 1$	0.454124145231932
	$\pm 3.14626437$	0.045875854768068
$D1Q5$ ( $T_L = 0.544144111$ )	0	0.533337122831274
	$\pm 1$	0.222074600148481
	$\pm 2.10749103$	0.011256838435882

TABLE 2.1: Roots of Hermite polynomials  $c_{i\alpha}$ , weights of the Gauss–Hermite quadrature  $W_{i\alpha}$  and lattice reference temperature  $T_L$ .

Another systematic approach for the construction of high-order lattices for the LBM is based on the *entropic construction* which tries to approximate the local Maxwellian on integer-valued discrete velocity sets [70].

### 2.2.2 Space–time discretization

After discretizing the velocity space, we integrate the discrete Boltzmann equation (2.24) along the the characteristic lines (discrete velocity directions) over the time step  $\delta t$ ,

$$f_i(\mathbf{x} + \mathbf{c}_i \delta t, t + \delta t) - f_i(\mathbf{x}, t) = \int_t^{t+\delta t} \Omega_i^{BGK}(\mathbf{x}(t'), t') dt'. \quad (2.25)$$

Integral of the collision term is evaluated using the second–order trapezoidal rule,

$$\int_t^{t+\delta t} \Omega_i^{BGK}(\mathbf{x}(t'), t') dt' = \frac{\delta t}{2} \left( \Omega_i^{BGK}(\mathbf{x}, t) + \Omega_i^{BGK}(\mathbf{x} + \mathbf{c}_i \delta t, t + \delta t) \right), \quad (2.26)$$

which results in an implicit scheme. In order to remove the implicitness of the scheme, the following transformations are applied,

$$\bar{f}_i = f_i - \frac{\delta t}{2} \Omega_i^{BGK}, \quad (2.27)$$

$$\bar{f}_i^{\text{eq}} = f_i^{\text{eq}}, \quad (2.28)$$

$$\Omega_i^{BGK} = \frac{1}{\tau + \delta t/2} \left( \bar{f}_i^{\text{eq}} - \bar{f}_i \right), \quad (2.29)$$

which leads to an explicit scheme, called the *lattice Boltzmann BGK (LBGK)* equation,

$$\boxed{\bar{f}_i(\mathbf{x} + \mathbf{c}_i \delta t, t + \delta t) - \bar{f}_i(\mathbf{x}, t) = \omega \left( \bar{f}_i^{\text{eq}} - \bar{f}_i \right)}. \quad (2.30)$$

Here, the left hand side is the shift operator representing propagation (advection) of populations, and the right hand side is the collision, with the new relaxation parameter  $\omega$  defined as,

$$\omega = \frac{\delta t}{\tau + \delta t/2}. \quad (2.31)$$

The flow variables can be computed as follows,

$$\rho = \sum_i \bar{f}_i = \sum_i f_i, \quad (2.32)$$

$$\rho \mathbf{u} = \sum_i \mathbf{c}_i \bar{f}_i = \sum_i \mathbf{c}_i f_i. \quad (2.33)$$

Note that, the overbars on the re-defined discrete populations will be omitted for the rest of the manuscript for the sake of simplicity.

### 2.2.3 Basic features of the standard LBM

It was shown that the LBM (2.30) can be derived by two consecutive discretizations of the Boltzmann equation. Here, we review some of the basic features of the standard LBM:

- The lattice Boltzmann equation (2.30) describes the dynamics of the populations  $f_i(\mathbf{x}, t)$  due to free streaming along the direction of discrete velocities  $\mathbf{c}_i$  (which form a space-filling lattice) and equilibrate at the nodes  $\mathbf{x}$ . This will result in the simple *streaming and collision* algorithm of the LBM.

- The streaming (propagation) is, then, simply the transfer of populations from node to node without loss of information [40]. This means that on regular Cartesian meshes, the propagation is exact.
- While propagation is linear, all non-linearity lies on the right hand side (collision) of (2.30), which is local in space. In other words, in the LBM, the non-local propagation is linear, and the non-linear collision is entirely local.
- While LBM has gained significant success in the incompressible regime, it is commonly known that the finite number of discrete particle velocities prevents LBM from going to high Mach number flows. In the next section, some of the models proposed to extend LBM to high-speed flows is reviewed.

#### 2.2.4 Lattice Boltzmann models for compressible flows

While LBM is now a well-established tool for low-speed incompressible flow simulations, development of LB models beyond that regime is a somewhat recent effort. The restrictions of LBM comes from the geometry of the discrete velocities, where the standard LBM velocities ( $D2Q9$  in two dimensions and  $D3Q19$  or  $D3Q27$  in three dimensions) yield a persistent error in the fluid stress tensor, which breaks Galilean invariance and limits the operation range of LBM to small flow velocities and a singular value of the temperature, known as the *lattice reference temperature*. Only under these conditions, the error in the stress tensor can be ignored. While one can cope with this error in most incompressible flow applications [71, 72], it prevents LBM from going to high-speed compressible flows as well as incorporating temperature dynamics. In other words, the number of discrete velocities of the standard lattices is too low to reproduce all the moments required for obtaining the full compressible Navier–Stokes–Fourier (NSF) equations [73]. For this reason, development of LB models capable of simulating thermal and compressible flows is still an open and active area of research.

Two general approaches have been proposed in the literature to address this issue. One approach is to include more discrete velocities and use the hierarchy of admissible high-order (or multi-speed) lattices [9, 70] to ensure the Galilean invariance and temperature independence of the stress tensor. Employing higher-order lattices result in adequately representing all the moments pertinent to the recovery of the full NSF equations. Many of the high-order models, however, are based on the Eulerian discretization



of the discrete Boltzmann equation (2.24) using standard schemes such as finite-difference or finite-volume schemes, see e.g. the models by Alexander, Chen & Sterling [74], Kataoka & Tsutahara [75], Li *et al.* [76], Watari [77] and Lin & Luo [78]. Thus, one of the most important advantages of LBM, the exact space discretization of propagation step on lattice nodes, is completely lost with those methods. Recently, a high-order on-lattice entropic LB model has been proposed by Frapolli, Chikatamarla & Karlin [79], which successfully covers a wide range of fluid flows, from low Mach weakly compressible [80] to transonic and supersonic regimes [81] with shock waves. However, high-order lattices increase computational cost significantly, which quickly becomes prohibitive for three-dimensional simulations. Furthermore, a limited temperature range is another restriction of high-order lattices [82].

Another approach for extension of LBM beyond its classical operation domain, maintains the simplicity and efficiency of the standard lattices and introduces correction terms in order to remove the aforementioned spurious terms in the stress tensor [83, 84]. Due to intrinsic non-uniqueness of the correction term, different implementations exist in the literature, all recover the same equations in the hydrodynamic limit [85–87]. See Hosseini, Darabiha & Thévenin [88] for a detailed review of different implementations. Besides correction term, to fully recover the NSF equations, one also needs to incorporate the energy equation. For doing that different models have been proposed in the literature which, in general, can be categorized into two main groups: hybrid and two-population methods.

Hybrid methods [89–92] rely on solving the total energy/entropy equation using conventional numerical schemes like finite-difference or finite-volume. Furthermore, multi-relaxation time collision operators, such as the hybrid regularized recursive model, are required to achieve high subsonic and supersonic regimes [92]. The majority of hybrid LB schemes also suffer from lack of energy conservation, as the energy equation is solved in a non-conservative form [93], and resolving this issue is still an on-going research [93–95]. In the two-population approach [85, 87, 96, 97], however, another population is used for the conservation of total energy. The latter, thus, provides a fully conservative and unified kinetic framework for the compressible flows. Earlier models [85, 96, 97] within the two-population framework on standard lattices, however, were limited to low-Mach thermal applications.

Given the previously mentioned advantages of the two-population approach, the goal of this project was to extend it to high-speed flows so that

it can capture the complex physics of compressible flows involving shock waves. By sticking to standard lattices and keeping the number of discrete speeds to a minimal, the resulting model substantially increases computational efficiency and makes high-fidelity simulations of compressible flows feasible.

## EXTENDED LATTICE BOLTZMANN MODELS FOR COMPRESSIBLE FLOWS

---

*Everything should be made as simple as possible, but no simpler.*

— Albert Einstein

### 3.1 INTRODUCTION

The development of accurate and efficient numerical methods for the simulation of compressible fluid flows remains a highly active research field in computational fluid dynamics, and is of great importance to many natural phenomena and engineering applications. Compressibility is usually measured by the Mach number,  $Ma = u/c_s$ , defined as the ratio of the flow velocity to the speed of sound and is mainly characterized by the importance of density and temperature variations and a dilatational velocity component. Furthermore, the presence of shock waves in compressible flows imposes severe challenges for an accurate numerical simulation.

As discussed in the previous chapter, while LBM on standard lattices recovers the Navier–Stokes equations in the hydrodynamic limit, there exist Galilean non-invariant error terms in the stress tensor which are negligible only in the limit of vanishing velocities and at a singular lattice temperature. This prevents LBM from going to higher velocities as well as incorporating temperature dynamics.

The extension of LBM beyond its classical operation domain has been so far addressed with different techniques. Introducing lattices with more velocities (high-order or multi-speed lattices) [98] is one technique, which has been shown to be successful in simulating compressible flows to some extent, but comes at the price of significantly increase of computational cost and a limited temperature range [98].

Another approach is based on introducing correction terms in the kinetic equations, which are designed to eliminate the error terms in the momentum equations resulting from the constraints of the standard lattices. Starting from the work of Prasianakis & Karlin [83], this approach has received considerable attention in recent years, as it maintains the simplicity and efficiency of the standard lattices. Furthermore, simulation

of compressible flows with the LBM also requires the incorporation of the temperature dynamics in some way. Energy equation can be solved directly using conventional numerical schemes [89–92]. However, a kinetically consistent approach is to employ additional set of populations for the conservation of total energy [85, 87, 96, 97]. Earlier models [85, 96, 97] within the two-population framework on standard lattices were limited to low-Mach thermal applications.

In this chapter, we follow this strategy and propose two different realizations of the extended LB model that deal with compressible flows on standard lattices. Both models are based on the two-population framework, where the conservation laws are split between the two sets. A set of  $f$ -populations  $f_i$  represents mass and momentum while another set of  $g$ -populations  $g_i$  is earmarked for the energy conservation. The models are different in the construction of correction terms as well as the energy equilibrium distribution function, as shall be described below.

### 3.2 KINETIC EQUATIONS

In the two-population approach,  $f_i$  are populations responsible for the mass and momentum conservation and  $g_i$  are used for the energy conservation. Following Karlin, Sichau & Chikatamarla [97], we consider a single relaxation time lattice Bhatnagar–Gross–Krook (LBGK) equations for the  $f$ -populations and a quasi-equilibrium LBM equation for the  $g$ -populations, corresponding to discrete velocities  $c_i$ , where  $i = 0, \dots, Q-1$ ,

$$f_i(\mathbf{x} + c_i \delta t, t + \delta t) - f_i(\mathbf{x}, t) = \omega(f_i^{\text{eq}} - f_i), \quad (3.1)$$

$$g_i(\mathbf{x} + c_i \delta t, t + \delta t) - g_i(\mathbf{x}, t) = \omega_1(g_i^{\text{eq}} - g_i) + (\omega - \omega_1)(g_i^{\text{eq}} - g_i^*). \quad (3.2)$$

The equilibrium  $f_i^{\text{eq}}$ ,  $g_i^{\text{eq}}$  and the quasi-equilibrium  $g_i^*$  satisfy the local conservation laws for the density  $\rho$ , momentum  $\rho \mathbf{u}$  and energy  $\rho E$ ,

$$\rho = \sum_{i=0}^{Q-1} f_i^{\text{eq}} = \sum_{i=0}^{Q-1} f_i, \quad (3.3)$$

$$\rho \mathbf{u} = \sum_{i=0}^{Q-1} c_i f_i^{\text{eq}} = \sum_{i=0}^{Q-1} c_i f_i, \quad (3.4)$$

$$\rho E = \sum_{i=0}^{Q-1} g_i^{\text{eq}} = \sum_{i=0}^{Q-1} g_i^* = \sum_{i=0}^{Q-1} g_i. \quad (3.5)$$

We consider a general caloric equation of state of ideal gas. Without loss of generality, the reference temperature is set at  $T = 0$  and the internal energy at unit density,  $U$ , is written as,

$$U = \int_0^T C_v(T) dT, \quad (3.6)$$

where  $T$  is the temperature and  $C_v(T)$  is the mass-based specific heat at constant volume. The energy at unit density  $E$  is,

$$E = U + \frac{u^2}{2}. \quad (3.7)$$

The relaxation parameters  $\omega$  and  $\omega_1$  are related to viscosity and thermal conductivity, as it will be shown below.

### 3.2.1 Moment requirements

In order for the system (3.1), (3.2) to recover the NSF equations, equilibrium population  $f_i^{\text{eq}}$  is required to reproduce the pertinent moments of the Maxwell-Boltzmann (MB) equilibrium distribution,

$$f^{\text{eq}} = \rho(2\pi RT)^{(-D/2)} e^{-\frac{(\mathbf{c}-\mathbf{u})^2}{2RT}}, \quad (3.8)$$

computed as,

$$F_{lmn}^{\text{MB}} = \rho(2\pi RT)^{-\frac{3}{2}} \int c_x^l c_y^m c_z^n e^{-\frac{(\mathbf{c}-\mathbf{u})^2}{2RT}} d\mathbf{c}, \quad (3.9)$$

where  $l, m$  and  $n$  are integer numbers correspond to linearly independent moments. In three dimensions ( $D = 3$ ), these moments can be written compactly as,

$$F_{lmn}^{\text{eq}} = \mathcal{O}_x^l \mathcal{O}_y^m \mathcal{O}_z^n \rho, \quad (3.10)$$

where operators  $\mathcal{O}_\alpha$  ( $\alpha = x, y, z$ ) acting on any smooth function  $A(\rho, \mathbf{u}, T)$  are defined as [97],

$$\mathcal{O}_\alpha A = RT \frac{\partial A}{\partial u_\alpha} + u_\alpha A. \quad (3.11)$$

In particular, the equilibrium pressure tensor  $\mathbf{P}^{\text{MB}}$  and the third-order equilibrium tensor  $\mathbf{Q}^{\text{MB}}$  computed using (3.10) as,

$$\mathbf{P}^{\text{MB}} = \int \mathbf{c} \otimes \mathbf{c} f^{\text{eq}} d\mathbf{c} = \mathbf{P}\mathbf{I} + \rho \mathbf{u} \otimes \mathbf{u}, \quad (3.12)$$

$$\mathbf{Q}^{\text{MB}} = \int \mathbf{c} \otimes \mathbf{c} \otimes \mathbf{c} f^{\text{eq}} d\mathbf{c} = \text{sym}(\mathbf{P}\mathbf{I} \otimes \mathbf{u}) + \rho \mathbf{u} \otimes \mathbf{u} \otimes \mathbf{u}, \quad (3.13)$$

are pertinent to the analysis of hydrodynamic limit. Here,  $P = \rho RT$  is the pressure,  $\text{sym}(\dots)$  denotes symmetrization and  $\mathbf{I}$  is the unit tensor.

Moving now onto the energy populations. The moments of the Maxwell–Boltzmann energy distribution function,

$$G_{lmn}^{\text{MB}} = \rho(2\pi RT)^{-\frac{3}{2}} \int c_x^l c_y^m c_z^n \left( \frac{c^2}{2} e^{-\frac{(c-\mathbf{u})^2}{2RT}} \right) d\mathbf{c}. \quad (3.14)$$

can similarly be written in a compact form using the operator (3.11) as follows,

$$G_{lmn}^{\text{MB}} = \rho \mathcal{O}_x^l \mathcal{O}_y^m \mathcal{O}_z^n E^{\text{MB}}, \quad (3.15)$$

where the generating function  $E^{\text{MB}}$  is the energy of the ideal monatomic gas at unit density (three translational degrees of freedom,  $C_v = (3/2)R$ ),

$$E^{\text{MB}} = \frac{3}{2}RT + \frac{u^2}{2}. \quad (3.16)$$

Next, we extend the Maxwell–Boltzmann energy moments (3.15) to a general caloric ideal gas equation of state (3.7). This amounts to replacing the generating function (3.16) with the energy (3.7),

$$G_{lmn}^{\text{eq}} = \rho \mathcal{O}_x^l \mathcal{O}_y^m \mathcal{O}_z^n E. \quad (3.17)$$

Among the higher-order moments (3.17), we recognize those pertinent to the hydrodynamic limit of the energy equation to be analyzed below. These are the equilibrium energy flux  $\mathbf{q}^{\text{MB}}$  and the flux of the energy flux tensor  $\mathbf{R}^{\text{MB}}$ ,

$$\mathbf{q}^{\text{MB}} = \left( H + \frac{u^2}{2} \right) \rho \mathbf{u}, \quad (3.18)$$

$$\mathbf{R}^{\text{MB}} = \left( H + \frac{u^2}{2} \right) \mathbf{P}^{\text{MB}} + P \mathbf{u} \otimes \mathbf{u}, \quad (3.19)$$

Here  $H$  is the specific enthalpy,

$$H = \int_0^T C_p(T) dT, \quad (3.20)$$

while  $C_p$  is the specific heat at constant pressure, satisfying Mayer’s relation,  $C_p - C_v = R$ .

Finally, similarly to [97], the quasi-equilibrium populations  $g_i^*$  are needed for adjusting the Prandtl number of the model. To that end, the quasi-equilibrium  $g_i^*$  differs from  $g_i^{\text{eq}}$  by the non-equilibrium energy flux only,

$$\mathbf{q}^* = \mathbf{q}^{\text{eq}} + \mathbf{u}(\mathbf{P} - \mathbf{P}^{\text{MB}} + \mathbf{q}^{*, \text{corr}}), \quad (3.21)$$

with  $\mathbf{P}$  being the pressure tensor,

$$\mathbf{P} = \int \mathbf{c} \otimes \mathbf{c} f d\mathbf{c}, \quad (3.22)$$

and  $\mathbf{q}^{*, \text{corr}}$  is an additional term required for consistency of the viscous heat dissipation and will be specified below.

### 3.2.2 Discrete velocities, factorization and anomaly of the standard lattices

We consider the  $D3Q27$  set of three-dimensional discrete velocities  $\mathbf{c}_i$ , where  $D = 3$  is the space dimension and  $Q = 27$  is the number of discrete speeds,

$$\mathbf{c}_i = (c_{ix}, c_{iy}, c_{iz}), \quad c_{i\alpha} \in \{-1, 0, 1\}, \quad i = 0, \dots, 26. \quad (3.23)$$

Below, we follow Karlin & Asinari [73] and consider a triplet of functions in two variables  $\xi$  and  $\mathcal{P}$ ,

$$\Psi_0(\xi, \mathcal{P}) = 1 - \mathcal{P}, \quad (3.24)$$

$$\Psi_1(\xi, \mathcal{P}) = \frac{1}{2}(\xi + \mathcal{P}), \quad (3.25)$$

$$\Psi_{-1}(\xi, \mathcal{P}) = \frac{1}{2}(-\xi + \mathcal{P}). \quad (3.26)$$

For vector-parameters  $(\xi_x, \xi_y, \xi_z)$  and  $(\mathcal{P}_{xx}, \mathcal{P}_{yy}, \mathcal{P}_{zz})$ , we consider a product associated with the speeds  $\mathbf{c}_i$  (3.23),

$$\Psi_i = \Psi_{c_{ix}}(\xi_x, \mathcal{P}_{xx}) \Psi_{c_{iy}}(\xi_y, \mathcal{P}_{yy}) \Psi_{c_{iz}}(\xi_z, \mathcal{P}_{zz}). \quad (3.27)$$

The moments of the product-form (3.27),

$$\mathcal{M}_{lmn} = \sum_{i=0}^{26} c_{ix}^l c_{iy}^m c_{iz}^n \Psi_i, \quad (3.28)$$

are readily computed thanks to the factorization,

$$\mathcal{M}_{lmn} = \mathcal{M}_{l00} \mathcal{M}_{0m0} \mathcal{M}_{00n}, \quad (3.29)$$

where  $\mathcal{M}_{000} = 1$ , and

$$\mathcal{M}_{l00} = \begin{cases} \xi_x, & l \text{ odd} \\ \mathcal{P}_{xx}, & l \text{ even} \end{cases}, \quad (3.30)$$

$$\mathcal{M}_{0m0} = \begin{cases} \xi_y, & m \text{ odd} \\ \mathcal{P}_{yy}, & m \text{ even} \end{cases}, \quad (3.31)$$

$$\mathcal{M}_{00n} = \begin{cases} \xi_z, & n \text{ odd} \\ \mathcal{P}_{zz}, & n \text{ even} \end{cases}. \quad (3.32)$$

The equilibrium  $f_i^{\text{eq}}$  is defined by setting,

$$\xi_\alpha = u_\alpha, \quad (3.33)$$

$$\mathcal{P}_{\alpha\alpha}^{\text{eq}} = RT + u_\alpha^2. \quad (3.34)$$

Substituting (3.33) and (3.34) into (3.27), we obtain,

$$f_i^{\text{eq}} = \rho \Psi_{c_{ix}}(u_x, \mathcal{P}_{xx}^{\text{eq}}) \Psi_{c_{iy}}(u_y, \mathcal{P}_{yy}^{\text{eq}}) \Psi_{c_{iz}}(u_z, \mathcal{P}_{zz}^{\text{eq}}). \quad (3.35)$$

The factorization (3.29) implies that equilibrium (3.35) verifies the maximal number  $Q = 27$  of the moment relations established by the Maxwell-Boltzmann (MB) distribution,

$$\sum_{i=0}^{26} c_{ix}^l c_{iy}^m c_{iz}^n f_i^{\text{eq}} = F_{lmn}^{\text{MB}}, \quad l, m, n \in \{0, 1, 2\}. \quad (3.36)$$

However, the third-order moment tensor at the equilibrium (3.35),

$$\mathbf{Q}^{\text{eq}} = \sum_{i=0}^{26} \mathbf{c}_i \otimes \mathbf{c}_i \otimes \mathbf{c}_i f_i^{\text{eq}} = \mathbf{Q}^{\text{MB}} + \tilde{\mathbf{Q}}, \quad (3.37)$$

contains an anisotropic deviation part  $\tilde{\mathbf{Q}} = \mathbf{Q}^{\text{eq}} - \mathbf{Q}^{\text{MB}}$  in (3.37), where only the diagonal elements are non-vanishing,

$$\tilde{Q}_{\alpha\beta\gamma} = \begin{cases} \rho u_\alpha (1 - 3RT) - \rho u_\alpha^3, & \text{if } \alpha = \beta = \gamma, \\ 0, & \text{otherwise.} \end{cases} \quad (3.38)$$

The origin of the diagonal anomaly (3.38) is the geometric constraint featured by the discrete speeds (3.23),  $c_{i\alpha}^3 = c_{i\alpha}$ , for any  $i = 0, \dots, 26$ . Put



differently, the equilibrium pressure tensor (3.12) and the off-diagonal elements of the equilibrium third-order moments (3.13) are included in the set of independent moments (3.36), hence they verify the Maxwell–Boltzmann moment relations by the product-form. Contrary to that, the diagonal components  $Q_{\alpha\alpha\alpha}^{\text{eq}}$  are not among the set of moments (3.23), hence the anomaly. A remedy, commonly employed in the conventional LBM for incompressible flow simulations, is to minimize the spurious effects of the said anisotropy by fixing the lattice reference temperature,  $RT_L = 1/3$  in order to eliminate the linear term  $O(u_\alpha)$  in (3.38).

Thus, the use of the equilibrium (3.35) in the LBGK equation (3.1) imposes a two-fold restriction: the temperature cannot be chosen differently from  $T_L$  while at the same time the flow velocity has to be maintained asymptotically vanishing. While the equilibrium (3.35) can still be used for the thermal LBM in the Bussinesq approximation [97], they make (3.35) insufficient for a compressible flow setting.

The above considerations can be summarized as follows: Because of the third-order moment anomaly (3.38), the LBGK equation (3.1) with the product-form equilibrium (3.35) is restricted in several ways, namely:

- The temperature is restricted to a single value, the lattice reference temperature  $T_L = 1/3$ .
- The flow velocity has to be asymptotically vanishing.

In the next parts, we propose two different models that address the restrictions mentioned above and extend the operating range of LBM to compressible flows.

### 3.3 EXTENDED COMPRESSIBLE MODEL I

As we shall see below through the Chapman-Enskog analysis, the anomaly in the diagonal third-order equilibrium moments (3.38) introduces spurious error terms into the momentum equations of the form,

$$X_\alpha = -\partial_\beta \left[ \left( \frac{1}{\omega} - \frac{1}{2} \right) \partial_\gamma \tilde{Q}_{\alpha\beta\gamma} \right] \delta t^2. \quad (3.39)$$

In the extended model I, a non-local correction terms  $\phi_i$  is directly introduced into the  $f_i$  kinetic equations (3.1) as a force term,

$$f_i(\mathbf{x} + \mathbf{c}_i \delta t, t + \delta t) - f_i(\mathbf{x}, t) = \omega(f_i^{\text{eq}} - f_i) + \phi_i, \quad (3.40)$$

in order to remove those error terms. This implies the following condition,

$$\sum_{i=0}^{Q-1} c_{i\alpha} \phi_i = X_\alpha, \quad (3.41)$$

while all other linearly independent moments of  $\phi_i$  are vanishing. For example, in 2D,  $\phi_i$  is

$$\phi_i = -A_{ix} \partial_x \left[ \left( \frac{1}{\omega} - \frac{1}{2} \right) \partial_x \tilde{Q}_{xxx} \right] \delta t^2 - A_{iy} \partial_y \left[ \left( \frac{1}{\omega} - \frac{1}{2} \right) \partial_y \tilde{Q}_{yyy} \right] \delta t^2, \quad (3.42)$$

where  $A_{ix}$  and  $A_{iy}$  are computed using,

$$A_{i\alpha} = c_{i\alpha} - \frac{1}{2} c_{i\alpha} c_i^2, \quad (3.43)$$

and for D2Q9 lattice model, we have

$$\begin{aligned} \phi_0 &= \phi_5 = \phi_6 = \phi_7 = \phi_8 = 0, \\ \phi_1 &= -0.5 \partial_x \left[ \left( \frac{1}{\omega} - \frac{1}{2} \right) \partial_x \tilde{Q}_{xxx} \right] \delta t^2, \\ \phi_2 &= -0.5 \partial_y \left[ \left( \frac{1}{\omega} - \frac{1}{2} \right) \partial_y \tilde{Q}_{yyy} \right] \delta t^2, \\ \phi_3 &= 0.5 \partial_x \left[ \left( \frac{1}{\omega} - \frac{1}{2} \right) \partial_x \tilde{Q}_{xxx} \right] \delta t^2, \\ \phi_4 &= 0.5 \partial_y \left[ \left( \frac{1}{\omega} - \frac{1}{2} \right) \partial_y \tilde{Q}_{yyy} \right] \delta t^2. \end{aligned} \quad (3.44)$$

In three dimensions (D3Q27 lattice),

$$A_{i\alpha} = \begin{cases} \frac{1}{2} c_{i\alpha}, & \text{for } c_i^2 = 1, \\ 0, & \text{otherwise.} \end{cases}$$

Furthermore, the populations  $g_i^{eq}$ ,  $g_i^*$  are constructed using the following second-order polynomial form,

$$G_i = W_i \left( M_0 + \frac{M_\alpha c_{i\alpha}}{T} + \frac{(M_{\alpha\beta} - M_0 T \delta_{\alpha\beta})(c_{i\alpha} c_{i\beta} - T \delta_{\alpha\beta})}{2T^2} \right) + \psi_i, \quad (3.45)$$

$G_i$	$M_0$	$M_\alpha$	$M_{\alpha\beta}$
$g_i^{eq}$	$\rho E$	$q_\alpha^{MB}$	$R_{\alpha\beta}^{MB}$
$g_i^*$	$\rho E$	$q_\alpha^{MB} + u_\beta \left( P_{\alpha\beta} - P_{\alpha\beta}^{eq} + \frac{1}{\omega} \partial_\alpha \tilde{Q}_{\alpha\alpha\alpha} \right)$	$R_{\alpha\beta}^{MB}$

TABLE 3.1: Moments needed for the computation of  $g_i^{eq}$  and  $g_i^*$ .

where  $W_i$  are temperature-dependent weights,

$$W_i = W_{c_{ix}} W_{c_{iy}} W_{c_{iz}}, \quad (3.46)$$

with

$$W_{-1} = \frac{T}{2}, \quad (3.47)$$

$$W_0 = 1 - T, \quad (3.48)$$

$$W_{+1} = \frac{T}{2}, \quad (3.49)$$

and

$$\psi_i = B_{i\alpha} Z_\alpha, \quad (3.50)$$

$$Z_\alpha = \frac{(1 - 3T)}{2T} (M_{\alpha\alpha} - TM_0), \text{ no summation} \quad (3.51)$$

$$B_{i\alpha} = \begin{cases} 1, \text{ for } c_i^2 = 0, \\ -\frac{1}{2} |c_{i\alpha}|, \text{ for } c_i^2 = 1 \\ 0, \text{ otherwise.} \end{cases}$$

Other terms required for the computations are listed in Table 3.1. Note that, summation convention is used in above equations. One can verify that the energy equilibrium population  $g_i^{eq}$  satisfies the pertinent moments (3.18) and (3.19) required for recovering the correct energy equation in the hydrodynamic limit.

### 3.3.1 Hydrodynamic limit

In order to derive the hydrodynamic equations of model I, we perform the Chapman–Enskog analysis for the kinetic equations (3.40) and (3.2). We start by expanding the shifted populations to second order,

$$\left[ \delta t D_i + \frac{\delta t^2}{2} D_i D_i \right] f_i = \omega (f_i^{\text{eq}} - f_i) + \phi_i \quad (3.52)$$

$$\begin{aligned} \left[ \delta t D_i + \frac{\delta t^2}{2} D_i D_i \right] g_i &= \omega_1 (g_i^{\text{eq}} - g_i) \\ &+ (\omega - \omega_1) (g_i^{\text{eq}} - g_i^*), \end{aligned} \quad (3.53)$$

where  $D_i$  is the derivative along the characteristics,

$$D_i = \partial_t + \mathbf{c}_i \cdot \nabla. \quad (3.54)$$

Now, we introduce a multi-scale expansion,

$$f_i = f_i^{(0)} + \delta t f_i^{(1)} + \delta t^2 f_i^{(2)} + O(\delta t^3), \quad (3.55)$$

$$\phi_i = \phi_i^{(0)} + \delta t \phi_i^{(1)} + \delta t^2 \phi_i^{(2)} + O(\delta t^3), \quad (3.56)$$

$$g_i = g_i^{(0)} + \delta t g_i^{(1)} + \delta t^2 g_i^{(2)} + O(\delta t^3), \quad (3.57)$$

$$g_i^* = g_i^{*(0)} + \delta t g_i^{*(1)} + \delta t^2 g_i^{*(2)} + O(\delta t^3), \quad (3.58)$$

$$\partial_t = \partial_t^{(1)} + \delta t \partial_t^{(2)} + O(\delta t^2), \quad (3.59)$$

and substitute them into (3.52) and (3.53). Using the notation,

$$D_i^{(1)} = \partial_t^{(1)} + \mathbf{c}_i \cdot \nabla, \quad (3.60)$$

we obtain, from zeroth through second order in the time step  $\delta t$ , for the  $f$ -populations,

$$f_i^{(0)} = f_i^{\text{eq}}, \quad (3.61)$$

$$\phi_i^{(0)} = 0, \quad (3.62)$$

$$D_i^{(1)} f_i^{(0)} = -\omega f_i^{(1)}, \quad (3.63)$$

$$\phi_i^{(1)} = 0, \quad (3.64)$$

$$\begin{aligned} \partial_t^{(2)} f_i^{(0)} + \mathbf{c}_i \cdot \nabla f_i^{(1)} - \frac{\omega}{2} D_i^{(1)} f_i^{(1)} \\ = -\omega f_i^{(2)} + \phi_i^{(2)}, \end{aligned} \quad (3.65)$$

and similarly for the  $g$ -populations,

$$g_i^{(0)} = g_i^{*(0)} = g_i^{\text{eq}}, \quad (3.66)$$

$$D_i^{(1)} g_i^{(0)} = -\omega_1 g_i^{(1)} - (\omega - \omega_1) g_i^{*(1)}, \quad (3.67)$$

$$\begin{aligned} \partial_t^{(2)} g_i^{(0)} + \mathbf{c}_i \cdot \nabla g_i^{(1)} - \frac{\omega_1}{2} D_i^{(1)} g_i^{(1)} - \frac{\omega - \omega_1}{2} D_i^{(1)} g_i^{*(1)} \\ = -\omega_1 g_i^{(2)} - (\omega - \omega_1) g_i^{*(2)}. \end{aligned} \quad (3.68)$$

With (3.61) and (3.66), the mass, momentum and energy conservation (3.3), (3.4) and (3.5) imply the solvability conditions,

$$\sum_{i=0}^{26} f_i^{(k)} = 0, \quad k = 1, 2, \dots; \quad (3.69)$$

$$\sum_{i=0}^{26} \mathbf{c}_i f_i^{(k)} = 0, \quad k = 1, 2, \dots; \quad (3.70)$$

$$\sum_{i=0}^{26} g_i^{*(k)} = \sum_{i=0}^{26} g_i^{(k)} = 0, \quad k = 1, 2, \dots \quad (3.71)$$

With the  $f$ -equilibrium (3.35) and the  $g$ -equilibrium (3.45), while taking into account the solvability conditions (3.69), (3.70) and (3.71), and also making use of the equilibrium pressure tensor (3.12), and the equilibrium energy flux (3.18), the first-order kinetic equations (3.63) and (3.67) imply the following first-order balance equations for the density, momentum and energy,

$$\partial_t^{(1)} \rho = -\nabla \cdot (\rho \mathbf{u}), \quad (3.72)$$

$$\partial_t^{(1)} (\rho \mathbf{u}) = -\nabla \cdot (P \mathbf{I} + \rho \mathbf{u} \otimes \mathbf{u}). \quad (3.73)$$

$$\partial_t^{(1)} (\rho E) = -\nabla \cdot \mathbf{q}^{\text{eq}}. \quad (3.74)$$

Using (3.72) and (3.73), The first-order energy equation (3.74) can be written in terms of the temperature as,

$$\rho C_v \partial_t^{(1)} T = -\rho C_v \mathbf{u} \cdot \nabla T - P(\nabla \cdot \mathbf{u}). \quad (3.75)$$

Thus, to first order, the LBM recovers the compressible Euler equations for a generic ideal gas.

Moreover, the first-order constitutive relation for the nonequilibrium pressure tensor  $\mathbf{P}^{(1)}$  is found from (3.63) as follows, using (3.12), (3.37), (3.13) and (3.38),

$$-\omega \mathbf{P}^{(1)} = \partial_t^{(1)} \mathbf{P}^{\text{MB}} + \nabla \cdot \mathbf{Q}^{\text{MB}} + \nabla \cdot \tilde{\mathbf{Q}}, \quad (3.76)$$

where

$$\mathbf{P}^{(1)} = \sum_{i=0}^{Q-1} \mathbf{c}_i \otimes \mathbf{c}_i f_i^{(1)}. \quad (3.77)$$

Using (3.72), (3.73) and (3.75), we find in (3.76),

$$\partial_t^{(1)} \mathbf{P}^{\text{MB}} + \nabla \cdot \mathbf{Q}^{\text{MB}} = \mathbf{Z}, \quad (3.78)$$

where we have introduced a short-hand notation for the total stress, including both the shear and the bulk contributions,

$$\begin{aligned} \mathbf{Z} = & P \left( \nabla \mathbf{u} + \nabla \mathbf{u}^\dagger - \frac{2}{3} (\nabla \cdot \mathbf{u}) \mathbf{I} \right) \\ & + P \left( \frac{2}{3} - \frac{R}{C_v} \right) (\nabla \cdot \mathbf{u}) \mathbf{I}, \end{aligned} \quad (3.79)$$

and where  $(\cdot)^\dagger$  denotes transposition. With (3.78) and (3.79), the nonequilibrium pressure tensor (3.76) becomes,

$$\mathbf{P}^{(1)} = -\frac{1}{\omega} \mathbf{Z} - \frac{1}{\omega} \nabla \cdot \tilde{\mathbf{Q}}. \quad (3.80)$$

A comment is in order. In (3.80), the first term is the conventional contribution from both the shear and the bulk stress. The second term is anomalous due to the diagonal anisotropy (3.38) and will be canceled out by the counter-term  $\phi_i^{(2)}$ , as we shall see below.

Similarly, the first-order constitutive relation for the nonequilibrium energy flux  $\mathbf{q}^{(1)}$  is found from (3.67),

$$-\omega_1 \mathbf{q}^{(1)} - (\omega - \omega_1) \mathbf{q}^{*(1)} = \partial_t^{(1)} \mathbf{q}^{\text{eq}} + \nabla \cdot \mathbf{R}^{\text{eq}}. \quad (3.81)$$

Evaluating the right hand side of (3.81) with the help of the first-order relations (3.72), (3.73) and (3.75), we obtain,

$$\partial_t^{(1)} \mathbf{q}^{\text{eq}} + \nabla \cdot \mathbf{R}^{\text{eq}} = PC_p \nabla T + (\mathbf{u} \cdot \mathbf{Z}). \quad (3.82)$$

With (3.82), the nonequilibrium energy flux (3.81) becomes,

$$\mathbf{q}^{(1)} = -\frac{1}{\omega_1} P C_p \nabla T - \frac{1}{\omega_1} (\mathbf{u} \cdot \mathbf{Z}) - \frac{\omega - \omega_1}{\omega_1} \mathbf{q}^{*(1)}. \quad (3.83)$$

The quasi-equilibrium energy flux  $\mathbf{q}^{*(1)}$  is evaluated according to (3.45) and by taking into account the first-order constitutive relation for the pressure tensor (3.80),

$$\mathbf{q}^{*(1)} = \mathbf{u} \cdot \left( \mathbf{P}^{(1)} + \frac{1}{\omega} \nabla \cdot \tilde{\mathbf{Q}} \right) = -\frac{1}{\omega} (\mathbf{u} \cdot \mathbf{Z}). \quad (3.84)$$

We comment that the first term in the nonequilibrium energy flux (3.83) is a precursor of the Fourier law of thermal conductivity while the second and the third terms combine to the viscous heating contribution, as we shall see it below. The quasi-equilibrium flux (3.84) is required for consistency of the viscous heating with the prescribed Prandtl number [97].

With the first-order constitutive relations for the nonequilibrium fluxes (3.80) and (3.83) in place, we proceed to the second-order approximation. Applying the solvability condition (3.69) and (3.70) to the second-order  $f$ -equation (3.65), we obtain,

$$\partial_t^{(2)} \rho = 0, \quad (3.85)$$

$$\partial_t^{(2)} (\rho \mathbf{u}) = -\nabla \cdot \left[ \left( 1 - \frac{\omega}{2} \right) \mathbf{P}^{(1)} \right] + \sum_i c_i \phi_i^{(2)}. \quad (3.86)$$

The second-order momentum equation (3.86) is transformed by virtue of (3.80) to give,

$$\partial_t^{(2)} (\rho \mathbf{u}) = -\nabla \cdot \left[ -\left( \frac{1}{\omega} - \frac{1}{2} \right) \mathbf{Z} - \left( \frac{1}{\omega} - \frac{1}{2} \right) \nabla \cdot \tilde{\mathbf{Q}} \right] + \sum_i c_i \phi_i^{(2)}. \quad (3.87)$$

Note that, the anomalous terms

$$\mathbf{X} = -\nabla \cdot \left[ \left( \frac{1}{\omega} - \frac{1}{2} \right) \nabla \cdot \tilde{\mathbf{Q}} \right], \quad (3.88)$$

are canceled out by setting,

$$\sum_i c_i \phi_i^{(2)} = \mathbf{X}, \quad (3.89)$$

and the final result (3.90),

$$\partial_t^{(2)} (\rho \mathbf{u}) = -\nabla \cdot \left[ -\left( \frac{1}{\omega} - \frac{1}{2} \right) \mathbf{Z} \right], \quad (3.90)$$

is isotropic.

Finally, applying solvability condition (3.71) to the second-order  $g$ -equation (3.68), we find

$$\partial_t^{(2)}(\rho E) = -\nabla \cdot \left[ \left(1 - \frac{\omega_1}{2}\right) \mathbf{q}^{(1)} - \frac{\omega - \omega_1}{2} \mathbf{q}^{*(1)} \right]. \quad (3.91)$$

Taking into account the first-order energy flux (3.83) and the quasi-equilibrium energy flux (3.84), we obtain in (3.91),

$$\begin{aligned} \partial_t^{(2)}(\rho E) = & -\nabla \cdot \left[ -\left(\frac{1}{\omega_1} - \frac{1}{2}\right) C_p P \nabla T \right] \\ & -\nabla \cdot \left[ -\left(\frac{1}{\omega} - \frac{1}{2}\right) (\mathbf{u} \cdot \mathbf{Z}) \right]. \end{aligned} \quad (3.92)$$

While the first term leads to the Fourier law, it is important to note that the second term represents viscous heating consistent with the momentum equation (3.90). The latter consistency is implied by the construction of the quasi-equilibrium energy flux (3.84). This concludes the second-order accurate analysis of the hydrodynamic limit of the LBM system (3.40) and (3.2), and we proceed with a summary of the gas dynamics equations thereby recovered.

### 3.3.2 Equations of gas dynamics

Combining the first- and second-order contributions to the density, the momentum and the energy equation, (3.72) and (3.85), (3.73) and (3.90), and (3.74) and (3.92), respectively, and using a notation,  $\partial_t = \partial_t^{(1)} + \delta t \partial_t^{(2)}$ , we arrive at the continuity, the flow and the energy equations of gas dynamics as follows,

$$\partial_t \rho + \nabla \cdot (\rho \mathbf{u}) = 0, \quad (3.93)$$

$$\partial_t (\rho \mathbf{u}) + \nabla \cdot (\rho \mathbf{u} \otimes \mathbf{u}) + \nabla \cdot \boldsymbol{\pi} = 0, \quad (3.94)$$

$$\partial_t (\rho E) + \nabla \cdot (\rho E \mathbf{u}) + \nabla \cdot \mathbf{q} + \nabla \cdot (\boldsymbol{\pi} \cdot \mathbf{u}) = 0. \quad (3.95)$$

Here,  $\boldsymbol{\pi}$  is the pressure tensor

$$\boldsymbol{\pi} = P \mathbf{I} - \mu \left( \mathbf{S} - \frac{2}{3} (\nabla \cdot \mathbf{u}) \mathbf{I} \right) - \zeta (\nabla \cdot \mathbf{u}) \mathbf{I}, \quad (3.96)$$

with  $P$  the pressure of ideal gas,

$$P = \rho RT, \quad (3.97)$$



with the strain rate tensor

$$\mathbf{S} = \nabla \mathbf{u} + \nabla \mathbf{u}^\dagger, \quad (3.98)$$

and the dynamic viscosity  $\mu$  and the bulk viscosity  $\varsigma$ ,

$$\mu = \left( \frac{1}{\omega} - \frac{1}{2} \right) P \delta t, \quad (3.99)$$

$$\varsigma = \left( \frac{2}{3} - \frac{R}{C_v} \right) \mu. \quad (3.100)$$

The heat flux  $\mathbf{q}$  in the energy equation (3.95) reads

$$\mathbf{q} = -\kappa \nabla T, \quad (3.101)$$

with the thermal conductivity coefficient  $\kappa$ ,

$$\kappa = \left( \frac{1}{\omega_1} - \frac{1}{2} \right) C_p P \delta t. \quad (3.102)$$

The Prandtl number due to (3.99) and (3.102) is,

$$\text{Pr} = \frac{C_p \mu}{\kappa} = \frac{\omega_1 (2 - \omega)}{\omega (2 - \omega_1)}, \quad (3.103)$$

while the adiabatic exponent,

$$\gamma = \frac{C_p}{C_v}, \quad (3.104)$$

is defined by the choice of the caloric equations of state (3.6) and Mayer's relation,  $C_p - C_v = R$ . The mass, momentum and energy equations, (3.93), (3.94) and (3.95) are the standard equations of the macroscopic gas dynamics.

### 3.3.3 Summary of the extended model I

The kinetic equations for the momentum  $f$  and energy  $g$  populations are [87]

$$f_i(\mathbf{x} + \mathbf{c}_i \delta t, t + \delta t) - f_i(\mathbf{x}, t) = \omega (f_i^{\text{eq}} - f_i) + \phi_i,$$

$$g_i(\mathbf{x} + \mathbf{c}_i \delta t, t + \delta t) - g_i(\mathbf{x}, t) = \omega_1 (g_i^{\text{eq}} - g_i) + (\omega - \omega_1) (g_i^{\text{eq}} - g_i^*).$$

(3.105)

The equilibrium population  $f_i^{eq}$  is computed using (3.35) and the energy equilibrium and quasi-equilibrium populations are computed with (3.45). Furthermore, the relaxation parameters  $\omega$  and  $\omega_1$  are related to dynamic viscosity and thermal conductivity as follows,

$$\mu = \left( \frac{1}{\omega} - \frac{1}{2} \right) P \delta t, \quad (3.106)$$

$$\kappa = \left( \frac{1}{\omega_1} - \frac{1}{2} \right) C_p P \delta t. \quad (3.107)$$

### 3.3.4 Numerical validation

In this section, we shall assess the accuracy and performance of the proposed LB model. In all simulations, the gas constant was set to  $R = 1$ , the time step is  $\delta t = 1$  and the spatial derivatives in the correction term  $\phi_i$  are evaluated using a second-order central difference scheme.

#### 3.3.4.1 Galilean invariance, isotropy and speed of sound

The first numerical experiment tests the Galilean invariance of the model by measuring the kinematic viscosity  $\nu = \mu/\rho$  and thermal diffusivity  $\alpha = \kappa/C_p\rho$  for the decay of a plane shear wave. For viscosity measurement, the initial conditions of the flow are

$$\rho = \rho_0, \quad u_x = a_0 \sin(2\pi y/L_y), \quad u_y = \text{Ma} \sqrt{\gamma T}, \quad (3.108)$$

where  $\text{Ma} = u_0/\sqrt{\gamma T}$  is the advection Mach number,  $\gamma = 1.4$ ,  $a_0 = 0.001$  is the amplitude and  $L_y = 200$  is number of nodes in the  $y$  direction,  $\rho_0 = 1$  and  $T = 0.1$ . Periodic boundary conditions are applied in both  $x$  and  $y$  directions. The numerical viscosity ( $\nu_{num}$ ) is measured by fitting an exponential to the time decay of maximum flow velocity  $u_{x,\max} \sim e^{-\nu t(2\pi/L_y)^2}$ .

In Fig. 3.1, measured viscosity is compared with the imposed viscosity at different advection Mach numbers. It is evident that the measured viscosity is in good agreement with the theoretical values, and is independent of the frame velocity. However, in this special case, the diagonal anomaly (3.38) is dormant and does not trigger any spurious effects because the derivatives  $\partial_x \tilde{Q}_{xxx}$  and  $\partial_y \tilde{Q}_{yyy}$  both vanish. Consequently, in order to trigger the anisotropy of the deviation terms (3.38) and to show the necessity of using the correction term, the shear wave is rotated by  $\pi/4$ . The temperature

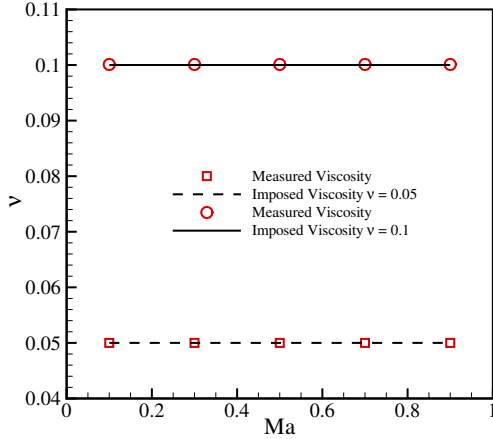


FIGURE 3.1: Numerical measurement of the fluid viscosity for axis-aligned shear wave setup at temperature  $T = 0.1$  for different velocities.

is kept at  $T = 0.1$ . The viscosity measurement is shown in Fig. 3.2 for different advection Mach numbers. It can be observed that the model lacks Galilean invariance when using the product-form equilibrium (3.35) without correction  $\phi_i$ . However, once the correction term is included, the present model recovers the imposed viscosity, independent of the frame velocity.

Similarly, for thermal diffusivity  $\alpha$ , the initial conditions are

$$\rho = \rho_0 + a_0 \sin(2\pi y / L_y), u_x = u_0, u_y = 0.0, T = \rho_0 T_0 / \rho, \quad (3.109)$$

and thermal diffusivity is measured through the time decay of temperature, where advection Mach number and adiabatic exponent are defined as in previous case. Simulation results are illustrated in Fig. 3.3 for two different Prandtl numbers, where excellent agreement between theory and numerical results can be observed up to  $Ma = 0.9$ . This demonstrates the Galilean invariance for both the momentum and energy equations.

Finally, in order to validate temperature independence of the present model, the speed of sound  $c_s$  is measured and compared to the theoretical value  $c_s = \sqrt{\gamma T}$  for different values of  $\gamma$  in Fig. 3.4. A quasi-one-dimensional setup is separated into two regions with a pressure difference  $\Delta P = 10^{-4}$  at uniform temperature. Then, the speed of sound is measured numerically by tracking the shock front of the propagated sound wave.

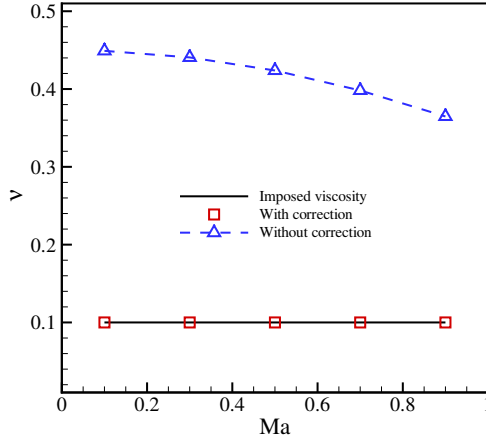


FIGURE 3.2: Numerical measurement of the fluid viscosity for rotated shear wave setup at temperature  $T = 0.1$  for different velocities.

The Prandtl number is set to  $Pr = 0.71$ . From Fig. 3.4 it is evident that the present model can correctly predict the speed of sound in a wide range of temperatures.

#### 3.3.4.2 Shock Tube

The setup for this problem is similar to that of sound speed measurement and the initial conditions are as follows,

$$(\rho, u_x, u_y, T) = \begin{cases} (0.5, 0, 0, 0.2), & x/L_x \leq 0.5, \\ (2.0, 0, 0, 0.025), & x/L_x > 0.5. \end{cases} \quad (3.110)$$

A  $3000 \times 5$  grid was used with  $\mu = 0.025$ , and  $\gamma = 2.0$ . Simulation results for the density, temperature and pressure at time  $t = 1273$ , in lattice units, are shown in Fig. 3.5. It can be observed that the present results are in excellent agreement with the analytical solutions [99], apart from a minor oscillatory pattern at the shock front, also present in other models [89].

#### 3.3.4.3 Thermal Couette flow

The thermal Couette flow between two parallel plates is considered to test the viscous heat dissipation. In this problem, the upper lid with higher

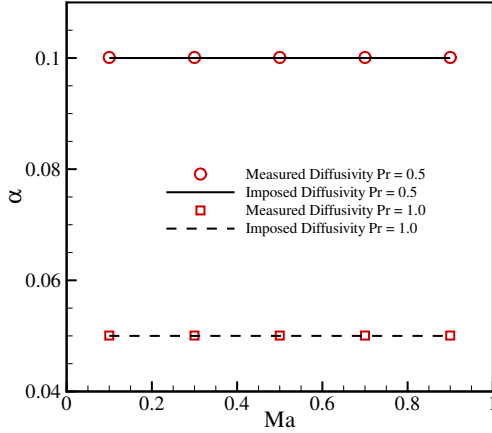


FIGURE 3.3: Numerical measurement of the fluid thermal diffusivity for axis-aligned shear wave setup at Prandtl numbers  $Pr = 0.5$ ,  $Pr = 1.0$ .

temperature  $T_H$  is moving at a constant speed of  $u_0$ , while the lower wall is kept at rest with a temperature  $T_C$ . The analytical solution for the reduced temperature can be written as,

$$\frac{T - T_C}{T_H - T_C} = \frac{y}{L_y} + \frac{Pr Ec}{2} \frac{y}{L_y} \left(1 - \frac{y}{L_y}\right), \quad (3.111)$$

where  $Ec = u_0^2 / (C_p \Delta T)$  is the Eckert number and  $\Delta T = T_H - T_C$ . Periodic boundary conditions are applied in the horizontal direction and the Tamm-Mott-Smith (TMS) boundary conditions, as described in [97], are used for the top and bottom walls. The simulations are performed at  $Ma = u_0 / \sqrt{\gamma T_C} = 0.5$  and with the following parameters:  $L_y = 50$ ,  $Re = \rho u_0 L_y / \mu = 100$ ,  $T_C = 1/3$ ,  $\gamma = 1.4$ . Figures 3.6 and 3.7 show the temperature profile of thermal Couette flow, at different Eckert and Prandtl numbers, respectively, which are in excellent agreement with the analytical solution.

To show the effect of correction terms, the solutions obtained for  $Ec = 4.0$  and  $Pr = 0.71$  with and without correction terms are compared in Fig. 3.8, which demonstrates that correction terms have significant effect on the viscous heating in this problem and that the present model with the correction terms can recover the analytical solution with excellent accuracy.

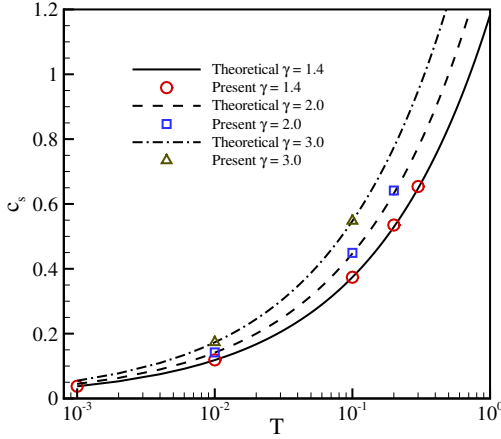


FIGURE 3.4: Numerical measurement of the speed of sound at three different adiabatic exponents  $\gamma$ .

### 3.4 EXTENDED COMPRESSIBLE MODEL II

In the previous model, the anomalous term in the momentum equation was canceled out at the level of second-order kinetic equations. That, in turn, results in an expression for the correction term that contains the second derivative of the deviation  $\tilde{Q}$ , see Eq. (3.39). Different from the previous model, the spurious anisotropy effects can also be canceled out by extending the equilibrium such that the third-order moment anomaly is compensated in the hydrodynamic limit. Because the anomaly only concerns the diagonal (unidirectional) elements of the third-order moments, the cancellation can be achieved by redefining the diagonal elements of the second-order moments. The advantage of this approach, as demonstrated below, is that it requires only the computation of first derivative of  $\tilde{Q}$ , thus provides a simpler formulation compared to model I. Another advantage, which will be explored in Chapter 4, is that it can easily be extended to supersonic flows by proper treatment of spatial derivatives in the correction term.

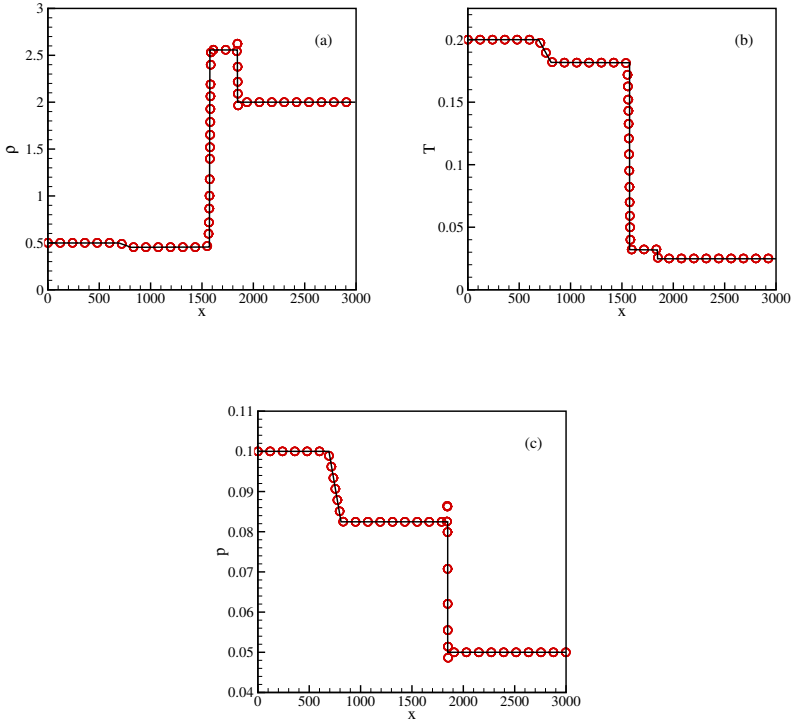


FIGURE 3.5: Shock tube simulation results after  $t = 1273$  time steps. (a) Density, (b) temperature and (c) pressure. Line: analytical solution; symbols: present model.

In model II, the  $f_i$  kinetic equations are modified using the extended equilibrium  $f_i^{\text{ex}}$ ,

$$f_i(\mathbf{x} + \mathbf{c}_i \delta t, t + \delta t) - f_i(\mathbf{x}, t) = \omega(f_i^{\text{ex}} - f_i). \quad (3.112)$$

As described below through the Chapman-Enskog expansion, in order to cancel the errors, the diagonal elements  $\mathcal{P}_{\alpha\alpha}^{\text{ex}}$  must be extended as

$$\mathcal{P}_{\alpha\alpha}^{\text{ex}} = \mathcal{P}_{\alpha\alpha}^{\text{eq}} + \delta t \left( \frac{2 - \omega}{2\rho\omega} \right) \partial_\alpha \tilde{Q}_{\alpha\alpha\alpha}, \quad (3.113)$$

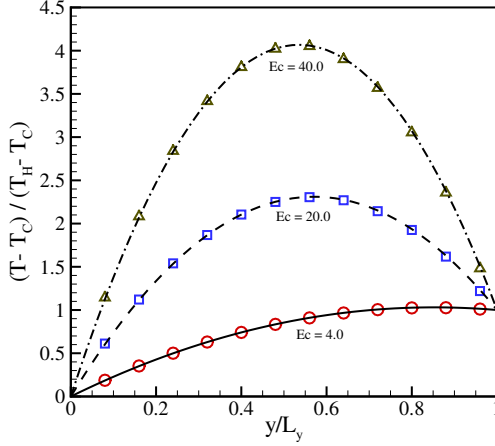


FIGURE 3.6: Temperature profile for the thermal Couette flow at various Eckert numbers and fixed Prandtl number  $Pr = 0.71$ . Lines: analytical solution; symbols: present model.

where  $\tilde{Q}_{\alpha\alpha\alpha}$  is the diagonal element of the anomaly (3.38),

$$\tilde{Q}_{\alpha\alpha\alpha} = \rho u_{\alpha}(1 - 3RT) - \rho u_{\alpha}^3. \quad (3.114)$$

With (3.113) instead of (3.34), the extended equilibrium  $f_i^{\text{ex}}$  is defined using the product-form as before,

$$f_i^{\text{ex}} = \rho \Psi_{c_{ix}}(u_x, \mathcal{P}_{xx}^{\text{ex}}) \Psi_{c_{iy}}(u_y, \mathcal{P}_{yy}^{\text{ex}}) \Psi_{c_{iz}}(u_z, \mathcal{P}_{zz}^{\text{ex}}). \quad (3.115)$$

The pressure tensor of the extended equilibrium is thus

$$\mathbf{P}^{\text{ex}} = \mathbf{P}^{\text{eq}} + \delta t \left( \frac{2 - \omega}{2\omega} \right) \nabla \cdot \tilde{\mathbf{Q}}. \quad (3.116)$$

Model II, thus, provides a consistent and simpler formulation for canceling the anisotropy effect of standard lattices.

The construction of  $g$ -equilibrium and  $g$ -quasi-equilibrium populations is also improved in model II, by using the product-form formulation of equilibrium which recovers all Maxwell–Boltzmann moments supported by the stencil. This is achieved by considering the operator version of



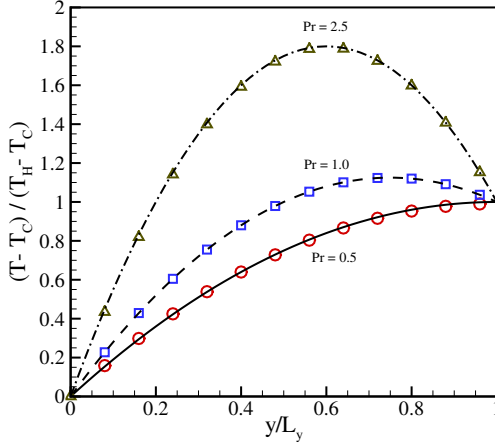


FIGURE 3.7: Temperature profile for the thermal Couette flow at various Prandtl numbers and fixed Eckert number  $Ec = 4.0$ . Lines: analytical solution; symbols: present model.

the product-form (3.27) and defining parameters  $\xi_\alpha$  and  $\mathcal{P}_{\alpha\alpha}$  as operator symbols,

$$\xi_\alpha = \mathcal{O}_\alpha, \quad (3.117)$$

$$\mathcal{P}_{\alpha\alpha} = \mathcal{O}_\alpha^2. \quad (3.118)$$

With the operators (3.117) and (3.118) substituted into the product form (3.27), the equilibrium populations  $g_i^{\text{eq}}$  are written using the generating function (3.7),

$$g_i^{\text{eq}} = \rho \Psi_{c_{ix}}(\mathcal{O}_x, \mathcal{O}_x^2) \Psi_{c_{iy}}(\mathcal{O}_y, \mathcal{O}_y^2) \Psi_{c_{iz}}(\mathcal{O}_z, \mathcal{O}_z^2) E. \quad (3.119)$$

With (3.29), it is straightforward to see that the equilibrium (3.119) verifies a subset of the equilibrium energy moments (3.17),

$$\sum_{i=0}^{26} c_{ix}^l c_{iy}^m c_{iz}^n g_i^{\text{eq}} = G_{lmn}^{\text{eq}}, \quad l, m, n \in \{0, 1, 2\}. \quad (3.120)$$

Thus, by construction, the  $g$ -equilibrium (3.119) recovers the maximal number  $Q = 27$  of the energy moments (3.17), including the energy flux (3.18)

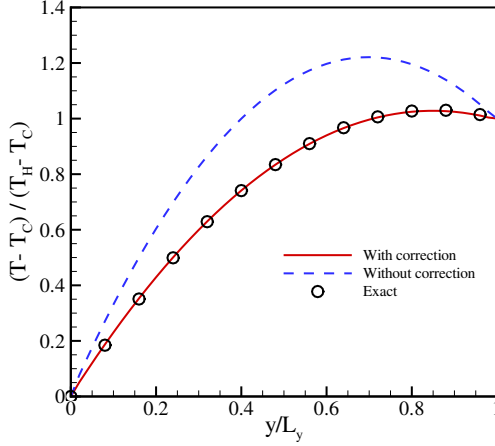


FIGURE 3.8: Comparison of temperature profile for the thermal Couette flow with and without correction terms at  $Ec = 4.0$  and  $Pr = 0.71$ .

and the flux of the energy flux (3.19), as opposed to equilibrium for model I.

As before, the quasi-equilibrium  $g_i^*$  differs from  $g_i^{eq}$  by the non-equilibrium energy flux only,

$$g_i^* = \begin{cases} g_i^{eq} + \frac{1}{2}c_i \cdot (q^* - q^{eq}), & \text{if } c_i^2 = 1, \\ g_i^{eq}, & \text{otherwise.} \end{cases} \quad (3.121)$$

Here  $q^*$  is a specified quasi-equilibrium energy flux. Indeed, (3.121) and (3.120) imply for  $l, m, n \in \{0, 1, 2\}$ ,

$$\sum_{i=0}^{26} c_{ix}^l c_{iy}^m c_{iz}^n g_i^* = \begin{cases} q_x^*, & \text{if } l = 1, m = 0, n = 0 \\ q_y^*, & \text{if } l = 0, m = 1, n = 0 \\ q_z^*, & \text{if } l = 0, m = 0, n = 1 \\ G_{lmn}^{eq}, & \text{otherwise.} \end{cases} \quad (3.122)$$

While the above construction holds for any specified  $\mathbf{q}^*$ , the quasi-equilibrium flux required for the consistent realization of the adjustable Prandtl number by the LBM system (3.112) and (3.2) reads,

$$\mathbf{q}^* = \mathbf{q}^{\text{eq}} + \mathbf{u} \cdot \left( \mathbf{P} - \mathbf{P}^{\text{eq}} + \frac{\delta t}{2} \nabla \cdot \tilde{\mathbf{Q}} \right), \quad (3.123)$$

where  $\mathbf{P}$  is the pressure tensor,

$$\mathbf{P} = \sum_{i=0}^{26} \mathbf{c}_i \otimes \mathbf{c}_i f_i. \quad (3.124)$$

With all the elements of the LBM system (3.112) and (3.2) specified, we now proceed with working out its hydrodynamic limit.

#### 3.4.1 Hydrodynamic limit

Taylor expansion of the shift operator in (3.112) and (3.2) to second order gives,

$$\left[ \delta t D_i + \frac{\delta t^2}{2} D_i D_i \right] f_i = \omega (f_i^{\text{ex}} - f_i), \quad (3.125)$$

$$\begin{aligned} \left[ \delta t D_i + \frac{\delta t^2}{2} D_i D_i \right] g_i &= \omega_1 (g_i^{\text{eq}} - g_i) \\ &+ (\omega - \omega_1) (g_i^{\text{eq}} - g_i^*). \end{aligned} \quad (3.126)$$

Introducing a multi-scale expansion,

$$f_i = f_i^{(0)} + \delta t f_i^{(1)} + \delta t^2 f_i^{(2)} + O(\delta t^3), \quad (3.127)$$

$$f_i^{\text{ex}} = f_i^{\text{ex}(0)} + \delta t f_i^{\text{ex}(1)} + \delta t^2 f_i^{\text{ex}(2)} + O(\delta t^3), \quad (3.128)$$

$$g_i = g_i^{(0)} + \delta t g_i^{(1)} + \delta t^2 g_i^{(2)} + O(\delta t^3), \quad (3.129)$$

$$g_i^* = g_i^{*(0)} + \delta t g_i^{*(1)} + \delta t^2 g_i^{*(2)} + O(\delta t^3), \quad (3.130)$$

$$\partial_t = \partial_t^{(1)} + \delta t \partial_t^{(2)} + O(\delta t^2), \quad (3.131)$$

substituting into (3.125) and (3.126), we obtain, from zeroth through second order in the time step  $\delta t$ , for the  $f$ -populations,

$$f_i^{(0)} = f_i^{\text{ex}(0)} = f_i^{\text{eq}}, \quad (3.132)$$

$$D_i^{(1)} f_i^{(0)} = -\omega \left( f_i^{(1)} - f_i^{\text{ex}(1)} \right), \quad (3.133)$$

$$\begin{aligned} \partial_t^{(2)} f_i^{(0)} + \mathbf{c}_i \cdot \nabla f_i^{(1)} - \frac{\omega}{2} D_i^{(1)} \left( f_i^{(1)} - f_i^{\text{ex}(1)} \right) \\ = -\omega f_i^{(2)} + \omega f_i^{\text{ex}(2)}, \end{aligned} \quad (3.134)$$

and similarly for the  $g$ -populations,

$$g_i^{(0)} = g_i^{*(0)} = g_i^{\text{eq}}, \quad (3.135)$$

$$D_i^{(1)} g_i^{(0)} = -\omega_1 g_i^{(1)} - (\omega - \omega_1) g_i^{*(1)}, \quad (3.136)$$

$$\begin{aligned} \partial_t^{(2)} g_i^{(0)} + \mathbf{c}_i \cdot \nabla g_i^{(1)} - \frac{\omega_1}{2} D_i^{(1)} g_i^{(1)} - \frac{\omega - \omega_1}{2} D_i^{(1)} g_i^{*(1)} \\ = -\omega_1 g_i^{(2)} - (\omega - \omega_1) g_i^{*(2)}. \end{aligned} \quad (3.137)$$

With (3.132) and (3.135), the mass, momentum and energy conservation (3.3), (3.4) and (3.5) imply the solvability conditions,

$$\sum_{i=0}^{26} f_i^{\text{ex}(k)} = \sum_{i=0}^{26} f_i^{(k)} = 0, \quad k = 1, 2, \dots; \quad (3.138)$$

$$\sum_{i=0}^{26} \mathbf{c}_i f_i^{\text{ex}(k)} = \sum_{i=0}^{26} \mathbf{c}_i f_i^{(k)} = 0, \quad k = 1, 2, \dots; \quad (3.139)$$

$$\sum_{i=0}^{26} g_i^{*(k)} = \sum_{i=0}^{26} g_i^{(k)} = 0, \quad k = 1, 2, \dots \quad (3.140)$$

With the  $f$ -equilibrium (3.35) and the  $g$ -equilibrium (3.119), while taking into account the solvability conditions (3.138), (3.139) and (3.140), and also making use of the equilibrium pressure tensor (3.12), and the equilibrium energy flux (3.18), the first-order kinetic equations (3.133) and (3.136) imply the following first-order balance equations for the density, momentum and energy,

$$\partial_t^{(1)} \rho = -\nabla \cdot (\rho \mathbf{u}), \quad (3.141)$$

$$\partial_t^{(1)} (\rho \mathbf{u}) = -\nabla \cdot (P \mathbf{I} + \rho \mathbf{u} \otimes \mathbf{u}). \quad (3.142)$$

$$\partial_t^{(1)} (\rho E) = -\nabla \cdot \mathbf{q}^{\text{eq}}. \quad (3.143)$$

The first-order energy equation (3.143) can be recast into the temperature equation by virtue of (3.141) and (3.142),

$$\rho C_v \partial_t^{(1)} T = -\rho C_v \mathbf{u} \cdot \nabla T - P(\nabla \cdot \mathbf{u}). \quad (3.144)$$

Thus, to first order, the LBM recovers the compressible Euler equations for a generic ideal gas.

Moreover, the first-order constitutive relation for the nonequilibrium pressure tensor  $\mathbf{P}^{(1)}$  is found from (3.133) as follows,

$$-\omega \mathbf{P}^{(1)} + \omega \mathbf{P}^{\text{ex}(1)} = \partial_t^{(1)} \mathbf{P}^{\text{MB}} + \nabla \cdot \mathbf{Q}^{\text{MB}} + \nabla \cdot \tilde{\mathbf{Q}}, \quad (3.145)$$

where

$$\mathbf{P}^{(1)} = \sum_{i=0}^{Q-1} \mathbf{c}_i \otimes \mathbf{c}_i f_i^{(1)}, \quad (3.146)$$

$$\mathbf{P}^{\text{ex}(1)} = \sum_{i=0}^{Q-1} \mathbf{c}_i \otimes \mathbf{c}_i f_i^{\text{ex}(1)}. \quad (3.147)$$

Using (3.141), (3.142) and (3.144), we find in (3.145),

$$\partial_t^{(1)} \mathbf{P}^{\text{MB}} + \nabla \cdot \mathbf{Q}^{\text{MB}} = \mathbf{Z}, \quad (3.148)$$

where we have introduced a short-hand notation for the total stress, including both the shear and the bulk contributions,

$$\begin{aligned} \mathbf{Z} = & P \left( \nabla \mathbf{u} + \nabla \mathbf{u}^\dagger - \frac{2}{3} (\nabla \cdot \mathbf{u}) \mathbf{I} \right) \\ & + P \left( \frac{2}{3} - \frac{R}{C_v} \right) (\nabla \cdot \mathbf{u}) \mathbf{I}, \end{aligned} \quad (3.149)$$

and where  $(\cdot)^\dagger$  denotes transposition. With (3.148) and (3.149), the nonequilibrium pressure tensor (3.145) becomes,

$$\mathbf{P}^{(1)} = -\frac{1}{\omega} \mathbf{Z} - \frac{1}{\omega} \nabla \cdot \tilde{\mathbf{Q}} + \mathbf{P}^{\text{ex}(1)}. \quad (3.150)$$

In (3.150), the first term is the conventional contribution from both the shear and the bulk stress. The second term is anomalous due to the diagonal anisotropy (3.38) while the third is the counter-term required to annihilate the spurious contribution in the next, second-order approximation. According to (3.116),

$$\mathbf{P}^{\text{ex}(1)} = \left( \frac{2-\omega}{2\omega} \right) \nabla \cdot \tilde{\mathbf{Q}}. \quad (3.151)$$

Similarly, the first-order constitutive relation for the nonequilibrium energy flux  $\mathbf{q}^{(1)}$  is found from (3.136),

$$-\omega_1 \mathbf{q}^{(1)} - (\omega - \omega_1) \mathbf{q}^{*(1)} = \partial_t^{(1)} \mathbf{q}^{\text{eq}} + \nabla \cdot \mathbf{R}^{\text{eq}}. \quad (3.152)$$

Evaluating the right hand side of (3.152) with the help of the first-order relations (3.141), (3.142) and (3.144), we obtain,

$$\partial_t^{(1)} \mathbf{q}^{\text{eq}} + \nabla \cdot \mathbf{R}^{\text{eq}} = PC_p \nabla T + (\mathbf{u} \cdot \mathbf{Z}). \quad (3.153)$$

With (3.153), the nonequilibrium energy flux (3.152) becomes,

$$\mathbf{q}^{(1)} = -\frac{1}{\omega_1} PC_p \nabla T - \frac{1}{\omega_1} (\mathbf{u} \cdot \mathbf{Z}) - \frac{\omega - \omega_1}{\omega_1} \mathbf{q}^{*(1)}. \quad (3.154)$$

The quasi-equilibrium energy flux  $\mathbf{q}^{*(1)}$  is evaluated according to (3.123) and by taking into account the first-order constitutive relation for the pressure tensor (3.150),

$$\mathbf{q}^{*(1)} = \mathbf{u} \cdot \left( \mathbf{P}^{(1)} + \frac{1}{2} \nabla \cdot \hat{\mathbf{Q}} \right) = -\frac{1}{\omega} (\mathbf{u} \cdot \mathbf{Z}). \quad (3.155)$$

The first term in the nonequilibrium energy flux (3.154) is a precursor of the Fourier law of thermal conductivity while the second and the third terms combine to the viscous heating contribution, as we shall see it below. The quasi-equilibrium flux (3.155) is required for consistency of the viscous heating with the prescribed Prandtl number [97].

With the first-order constitutive relations for the nonequilibrium fluxes (3.150) and (3.154) in place, we proceed to the second-order approximation. Applying the solvability condition (3.138) and (3.139) to the second-order  $f$ -equation (3.134), we obtain,

$$\partial_t^{(2)} \rho = 0, \quad (3.156)$$

$$\partial_t^{(2)} (\rho \mathbf{u}) = -\nabla \cdot \left[ \left( 1 - \frac{\omega}{2} \right) \mathbf{P}^{(1)} + \frac{\omega}{2} \mathbf{P}^{\text{ex}(1)} \right]. \quad (3.157)$$

The second-order momentum equation (3.157) is transformed by virtue of (3.150) and (3.151) to give,

$$\partial_t^{(2)} (\rho \mathbf{u}) = -\nabla \cdot \left[ -\left( \frac{1}{\omega} - \frac{1}{2} \right) \mathbf{Z} \right]. \quad (3.158)$$

Note that, the anomalous terms cancel out and the result (3.158) is manifestly isotropic.

Finally, applying solvability condition (3.140) to the second-order  $g$ -equation (3.137), we find

$$\partial_t^{(2)}(\rho E) = -\nabla \cdot \left[ \left(1 - \frac{\omega_1}{2}\right) \mathbf{q}^{(1)} - \frac{\omega - \omega_1}{2} \mathbf{q}^{*(1)} \right]. \quad (3.159)$$

Taking into account the first-order energy flux (3.154) and the quasi-equilibrium energy flux (3.155), we obtain in (3.159),

$$\begin{aligned} \partial_t^{(2)}(\rho E) = & -\nabla \cdot \left[ -\left(\frac{1}{\omega_1} - \frac{1}{2}\right) C_p P \nabla T \right] \\ & -\nabla \cdot \left[ -\left(\frac{1}{\omega} - \frac{1}{2}\right) (\mathbf{u} \cdot \mathbf{Z}) \right]. \end{aligned} \quad (3.160)$$

While the first term leads to the Fourier law, it is important to note that the second term represents viscous heating consistent with the momentum equation (3.158). The latter consistency is implied by the construction of the quasi-equilibrium energy flux (3.123) and (3.155). This concludes the second-order accurate analysis of the hydrodynamic limit of the LBM system (3.112) and (3.2), and we proceed with a summary of the gas dynamics equations thereby recovered.

### 3.4.2 Equations of gas dynamics

By combining the first- and second-order contributions to the density, momentum and the energy equation, (3.141) and (3.156), (3.142) and (3.158), and (3.143) and (3.160), respectively, we arrive at the continuity, the momentum and the energy equations of gas dynamics as follows,

$$\partial_t \rho + \nabla \cdot (\rho \mathbf{u}) = 0, \quad (3.161)$$

$$\partial_t (\rho \mathbf{u}) + \nabla \cdot (\rho \mathbf{u} \otimes \mathbf{u}) + \nabla \cdot \boldsymbol{\pi} = 0, \quad (3.162)$$

$$\partial_t (\rho E) + \nabla \cdot (\rho E \mathbf{u}) + \nabla \cdot \mathbf{q} + \nabla \cdot (\boldsymbol{\pi} \cdot \mathbf{u}) = 0, \quad (3.163)$$

where  $\boldsymbol{\pi}$  is the pressure tensor

$$\boldsymbol{\pi} = P \mathbf{I} - \mu \left( \mathbf{S} - \frac{2}{3} (\nabla \cdot \mathbf{u}) \mathbf{I} \right) - \varsigma (\nabla \cdot \mathbf{u}) \mathbf{I}, \quad (3.164)$$

with  $P$  the pressure of ideal gas,

$$P = \rho R T, \quad (3.165)$$

with the strain rate tensor,

$$\mathbf{S} = \nabla \mathbf{u} + \nabla \mathbf{u}^\dagger, \quad (3.166)$$

and the dynamic viscosity  $\mu$  and the bulk viscosity  $\zeta$ ,

$$\mu = \left( \frac{1}{\omega} - \frac{1}{2} \right) P \delta t, \quad (3.167)$$

$$\zeta = \left( \frac{2}{3} - \frac{R}{C_v} \right) \mu. \quad (3.168)$$

The heat flux  $\mathbf{q}$  in the energy equation (3.163) reads,

$$\mathbf{q} = -\kappa \nabla T, \quad (3.169)$$

with the thermal conductivity coefficient  $\kappa$ ,

$$\kappa = \left( \frac{1}{\omega_1} - \frac{1}{2} \right) C_p P \delta t. \quad (3.170)$$

The Prandtl number is,

$$\text{Pr} = \frac{C_p \mu}{\kappa} = \frac{\omega_1 (2 - \omega)}{\omega (2 - \omega_1)}, \quad (3.171)$$

while the adiabatic exponent,

$$\gamma = \frac{C_p}{C_v}, \quad (3.172)$$

is defined by the choice of the caloric equations of state (3.6) and Mayer's relation,  $C_p - C_v = R$ . The mass, momentum and energy equations, (3.161), (3.162) and (3.163) are the standard equations of the macroscopic gas dynamics. We shall conclude the model development with a summary of the key elements of the compressible extended LB model II.

### 3.4.3 Summary of the extended model II

The kinetic equations for the momentum  $f$  and energy  $g$  populations are [100]

$$\begin{aligned} f_i(\mathbf{x} + \mathbf{c}_i \delta t, t + \delta t) - f_i(\mathbf{x}, t) &= \omega (f_i^{\text{ex}} - f_i), \\ g_i(\mathbf{x} + \mathbf{c}_i \delta t, t + \delta t) - g_i(\mathbf{x}, t) &= \omega_1 (g_i^{\text{eq}} - g_i) + (\omega - \omega_1) (g_i^{\text{eq}} - g_i^*). \end{aligned}$$

(3.173)



The extended equilibrium population  $f_i^{\text{ex}}$  is computed using (3.115) and the energy equilibrium and quasi-equilibrium populations are computed with (3.119) and (3.121), respectively. The relaxation parameters  $\omega$  and  $\omega_1$  are related to dynamic viscosity and thermal conductivity as follows,

$$\mu = \left( \frac{1}{\omega} - \frac{1}{2} \right) P \delta t, \quad (3.174)$$

$$\kappa = \left( \frac{1}{\omega_1} - \frac{1}{2} \right) C_p P \delta t. \quad (3.175)$$

We shall proceed with the numerical validation of the compressible lattice Boltzmann model II.

#### 3.4.4 Numerical validation

Similar to previous model, the simulations here are performed with gas constant  $R = 1$ , time step  $\delta t = 1$  and second-order central difference evaluation of the spatial derivatives. The results of the Galilean invariance, speed of sound and thermal Couette flow for this model are identical to the previous one presented in Sec. (3.3.4), and are not shown here for the sake of brevity.

##### 3.4.4.1 Sod's shock tube

Sod's shock tube benchmark [101] is a classical Riemann problem, which is often used to test capability of a compressible flow solver in capturing shock waves, contact discontinuities and expansion fans. The initial flow field is given by,

$$(\rho, u_x, P) = \begin{cases} (1.0, 0, 0.15), & x/L_x \leq 0.5, \\ (0.125, 0, 0.015), & x/L_x > 0.5, \end{cases} \quad (3.176)$$

where  $L_x = 600$  is the number of grid points. Simulation results with the viscosity  $\mu = 0.015$  for the density and reduced velocity  $u^* = u/\sqrt{T_l}$ , where  $T_l$  is temperature on the left half of tube, at non-dimensional time  $t^* = t\sqrt{T_l}/L_x = 0.2$ , are shown in Fig. 3.9. It can be seen that, apart from a small oscillation, the results match the non-viscous exact solution well.

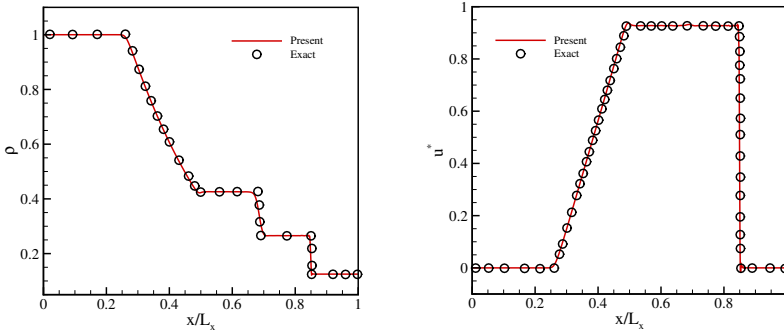


FIGURE 3.9: Density (left) and reduced velocity (right) profiles for Sod's shock tube simulation at non-dimensional time  $t^* = 0.2$ . Symbols: present model; line: exact solution.

### 3.4.5 Application of extended equilibrium to incompressible iso-thermal flows

The extended equilibrium introduced in the previous section can also be beneficial in incompressible iso-thermal applications by turning-off the second population and use a constant temperature instead. This would result in a fully Galilean invariant kinetic model in the incompressible regime. The resulting model extends LB models to simulations with higher values of the flow velocity and can be used at temperatures that are higher than the lattice reference temperature, which enhances computational efficiency by decreasing the number of required time steps [102].

Furthermore, the extended equilibrium (3.115) can be extended to cases with stretched (rectangular) lattices. Rectangular lattices may improve the computational efficiency of the LBM by using a coarser mesh in the direction of smaller gradients in the flow. Unlike other approaches of handling non-uniform grids (e.g. Eulerian [103, 104] and semi-Lagrangian off-lattice LBM [105–108] or grid refinement techniques [109, 110]), stretched lattices do not require a substantial change in the standard LBM algorithm. Recent works on the stretched LBM restore isotropy of the stress tensor by using multi-relaxation time LBM models [111–113]. However, these approaches do not address the flow velocity and temperature restrictions.

In this section, we show that the concept of extended equilibrium provides a unified view on the three aspects of the Galilean invariance problem in the LBM: the velocity range, the temperature range and grid stretching,

which all stem from the same error, induced by constraints of the discrete velocity set.

We begin with a brief review of kinetic equations. We consider the LBGK equation for the populations  $f_i$ , associated to the discrete velocities  $\mathbf{v}_i$  for  $i = 0, \dots, Q-1$ ,

$$f_i(\mathbf{x} + \mathbf{v}_i \delta t, t + \delta t) - f_i(\mathbf{x}, t) = \omega(f_i^{\text{ex}} - f_i), \quad (3.177)$$

where,

$$\rho = \sum_{i=0}^{Q-1} f_i^{\text{ex}} = \sum_{i=0}^{Q-1} f_i, \quad (3.178)$$

$$\rho \mathbf{u} = \sum_{i=0}^{Q-1} \mathbf{v}_i f_i^{\text{ex}} = \sum_{i=0}^{Q-1} \mathbf{v}_i f_i. \quad (3.179)$$

The relaxation parameter  $\omega$  is related to the kinematic viscosity  $\nu$ ,

$$\nu = \left( \frac{1}{\omega} - \frac{1}{2} \right) RT \delta t, \quad (3.180)$$

with  $T$  being the temperature and  $R$  is the gas constant.

With (3.23), we define the particles' velocities  $\mathbf{v}_i$  in a stretched cell as,

$$\mathbf{v}_i = (\lambda_x c_{ix}, \lambda_y c_{iy}, \lambda_z c_{iz}), \quad (3.181)$$

where  $\lambda_\alpha$  is the stretching factor in the direction  $\alpha$ . To maintain on-lattice propagation, the cell size is changed accordingly to  $\delta x_\alpha = \lambda_\alpha \delta t$ .

The (normalized,  $\mathcal{M}_{000} = 1$ ) moments  $\mathcal{M}_{lmn}$  are defined using the convention,

$$l \rightarrow x, m \rightarrow y, n \rightarrow z; l, m, n = 0, 1, 2, \dots, \quad (3.182)$$

and thus,

$$\rho \mathcal{M}_{lmn} = \sum_{i=0}^{Q-1} v_{ix}^l v_{iy}^m v_{iz}^n f_i. \quad (3.183)$$

For convenience, we use a more specific notation for the first-order and the diagonal second-order moments,

$$\mathcal{M}_{100} = u_x, \mathcal{M}_{010} = u_y, \mathcal{M}_{001} = u_z, \quad (3.184)$$

$$\mathcal{M}_{200} = \mathcal{P}_{xx}, \mathcal{M}_{020} = \mathcal{P}_{yy}, \mathcal{M}_{002} = \mathcal{P}_{zz}. \quad (3.185)$$

As before, we essentially follow [73] and consider a class of factorized populations. To that end, we define a triplet of functions in the three variables,  $u_\alpha$ ,  $\mathcal{P}_{\alpha\alpha}$  and  $\lambda_\alpha$ ,

$$\Psi_0(u_\alpha, \mathcal{P}_{\alpha\alpha}, \lambda_\alpha) = 1 - \frac{\mathcal{P}_{\alpha\alpha}}{\lambda_\alpha^2}, \quad (3.186)$$

$$\Psi_1(u_\alpha, \mathcal{P}_{\alpha\alpha}, \lambda_\alpha) = \frac{1}{2} \left( \frac{u_\alpha}{\lambda_\alpha} + \frac{\mathcal{P}_{\alpha\alpha}}{\lambda_\alpha^2} \right), \quad (3.187)$$

$$\Psi_{-1}(u_\alpha, \mathcal{P}_{\alpha\alpha}, \lambda_\alpha) = \frac{1}{2} \left( -\frac{u_\alpha}{\lambda_\alpha} + \frac{\mathcal{P}_{\alpha\alpha}}{\lambda_\alpha^2} \right). \quad (3.188)$$

For the vectors  $\mathbf{u}$ ,  $\mathcal{P}$ , and  $\lambda$ ,

$$\mathbf{u} = (u_x, u_y, u_z), \quad (3.189)$$

$$\mathcal{P} = (\mathcal{P}_{xx}, \mathcal{P}_{yy}, \mathcal{P}_{zz}), \quad (3.190)$$

$$\lambda = (\lambda_x, \lambda_y, \lambda_z), \quad (3.191)$$

we consider a product-form, associated with the discrete velocities  $v_i$  (3.181),

$$\Psi_i(\mathbf{u}, \mathcal{P}, \lambda) = \prod_{\alpha=x,y,z} \Psi_{c_{i\alpha}}(u_\alpha, \mathcal{P}_{\alpha\alpha}, \lambda_\alpha). \quad (3.192)$$

The normalized moments of the product-form (3.192),

$$\mathcal{M}_{lmn} = \sum_{i=0}^{Q-1} v_{ix}^l v_{iy}^m v_{iz}^n \Psi_i, \quad (3.193)$$

are readily computed thanks to the factorization,

$$\mathcal{M}_{lmn} = \mathcal{M}_{l00} \mathcal{M}_{0m0} \mathcal{M}_{00n}, \quad (3.194)$$

where

$$\mathcal{M}_{000} = 1, \quad (3.195)$$

$$\mathcal{M}_{l00} = \begin{cases} \lambda_x^{l-1} u_x, & l \text{ odd} \\ \lambda_x^{l-2} \mathcal{P}_{xx}, & l \text{ even} \end{cases}, \quad (3.196)$$

$$\mathcal{M}_{0m0} = \begin{cases} \lambda_y^{m-1} u_y, & m \text{ odd} \\ \lambda_y^{m-2} \mathcal{P}_{yy}, & m \text{ even} \end{cases}, \quad (3.197)$$

$$\mathcal{M}_{00n} = \begin{cases} \lambda_z^{n-1} u_z, & n \text{ odd} \\ \lambda_z^{n-2} \mathcal{P}_{zz}, & n \text{ even} \end{cases}. \quad (3.198)$$

For any stretching (3.191), the six-parametric family of normalized populations (3.192) is identified by the flow velocity (3.189) and the diagonal of the pressure tensor at unit density (3.190), and was termed the unidirectional quasi-equilibrium in Ref. [73]. We make use of the product-form (3.192) to construct all pertinent populations, the equilibrium and the extended equilibrium.

The equilibrium  $f_i^{\text{eq}}$  is defined by setting  $\mathcal{P}_{\alpha\alpha}$  (3.185) equal to the equilibrium diagonal element of the pressure tensor at unit density,

$$\mathcal{P}_{\alpha\alpha}^{\text{eq}} = RT + u_\alpha^2. \quad (3.199)$$

Thus, we get

$$f_i^{\text{eq}} = \rho \Psi_i(u, \mathcal{P}^{\text{eq}}, \lambda). \quad (3.200)$$

With (3.193), we find the pressure tensor and the third-order moment tensor at the equilibrium (3.200) as follows,

$$\mathbf{P}^{\text{eq}} = \sum_{i=0}^{Q-1} \mathbf{v}_i \otimes \mathbf{v}_i f_i^{\text{eq}} = \mathbf{P}^{\text{MB}}, \quad (3.201)$$

$$\mathbf{Q}^{\text{eq}} = \sum_{i=0}^{Q-1} \mathbf{v}_i \otimes \mathbf{v}_i \otimes \mathbf{v}_i f_i^{\text{eq}} = \mathbf{Q}^{\text{MB}} + \tilde{\mathbf{Q}}. \quad (3.202)$$

The isotropic parts,  $\mathbf{P}^{\text{MB}}$  and  $\mathbf{Q}^{\text{MB}}$ , are the Maxwell–Boltzmann (MB) pressure tensor and the third-order moment tensor, respectively,

$$\mathbf{P}^{\text{MB}} = P\mathbf{I} + \rho \mathbf{u} \otimes \mathbf{u}, \quad (3.203)$$

$$\mathbf{Q}^{\text{MB}} = \text{sym}(P\mathbf{I} \otimes \mathbf{u}) + \rho \mathbf{u} \otimes \mathbf{u} \otimes \mathbf{u}, \quad (3.204)$$

where  $P = \rho RT$  is the pressure,  $\text{sym}(\dots)$  denotes symmetrization and  $\mathbf{I}$  is the unit tensor. The anisotropy of the equilibrium (3.200) manifests with the deviation  $\tilde{\mathbf{Q}} = \mathbf{Q}^{\text{eq}} - \mathbf{Q}^{\text{MB}}$  in (3.204), where only the diagonal elements are non-vanishing,

$$\tilde{Q}_{\alpha\beta\gamma} = \begin{cases} \rho u_\alpha (\lambda_\alpha^2 - 3RT) - \rho u_\alpha^3, & \text{if } \alpha = \beta = \gamma, \\ 0, & \text{otherwise.} \end{cases} \quad (3.205)$$

As before, the origin of the *diagonal anomaly* (3.38) is the geometric constraint,  $v_{i\alpha}^3 = \lambda_\alpha^2 v_{i\alpha}$ , which is imposed by the choice of the discrete speeds (3.23), and was discussed in the case of the standard (unstretched) lattice with

$\lambda_\alpha = 1$ . A remedy in the latter case is to minimize spurious effects of anisotropy by fixing the temperature  $T = T_L$ ,

$$RT_L = \frac{1}{3}. \quad (3.206)$$

In other words, the anomalous term cannot be canceled, rather, by choosing  $T = T_L$ , its effect can be ignored but only under the assumption of an asymptotically small flow velocity. Moreover, for a quasi-incompressible flow ( $\text{Ma} \rightarrow 0$ , density variation  $\nabla \rho \sim \text{Ma}^2$ , where  $\text{Ma}$  is a characteristic Mach number), it is possible to further reduce the effect of the anomaly by rescaling the relaxation parameter [44], see a discussion in Appendix A.1.

The extended equilibrium  $f_i^{\text{ex}}$  is specified by using the product-form,

$$f_i^{\text{ex}} = \rho \Psi_i(\mathbf{u}, \mathcal{P}^{\text{ex}}, \lambda), \quad (3.207)$$

where the diagonal elements  $\mathcal{P}_{\alpha\alpha}^{\text{ex}}$  for the extended equilibrium are chosen as

$$\mathcal{P}_{\alpha\alpha}^{\text{ex}} = \mathcal{P}_{\alpha\alpha}^{\text{eq}} + \delta t \left( \frac{2 - \omega}{2\rho\omega} \right) \partial_\alpha \tilde{Q}_{\alpha\alpha\alpha}. \quad (3.208)$$

Note that, spatial derivative is evaluated using a second-order central difference scheme.

In the next section, we shall assess the accuracy and performance of the proposed incompressible LB model with extended equilibrium in a variety of scenarios. First, we measure the numerical viscosity with both regular and rectangular lattices in the simulation of a decaying shear wave. Second, we validate the model for the complex case of decaying homogeneous isotropic turbulence and show the effectiveness of using higher temperatures in saving compute time. Third, we investigate the applicability of the proposed model with stretched lattices in a periodic double shear layer flow, in a laminar flow over a flat plate, and finally in the case of the turbulent channel flow. In the simulations below, the gas constant was set to  $R = 1$ , the time step is  $\delta t = 1$  and Grad's approximation, as proposed in [114], was used for wall boundary conditions.

#### 3.4.5.1 *Decaying shear wave*

Similar to the compressible case and in order to show the necessity of using the extended equilibrium, the rotated shear wave is considered to trigger the anisotropy of the deviation terms (3.205). The anisotropy is further

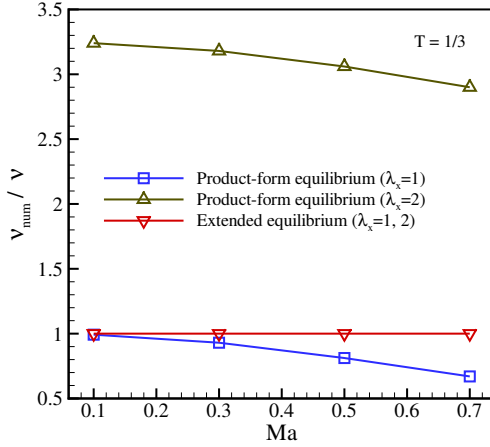


FIGURE 3.10: Numerical measurement of viscosity for rotated setup at temperature  $T = 1/3$  for different velocities and stretching ratios. The exact solution corresponds to  $v_{num}/\nu = 1$ .

increased by conducting simulations on a stretched grid with  $\lambda_x = 2$ . The temperature is at  $T = 1/3$ . The viscosity measurement is shown in Fig. 3.10 for different advection Mach numbers and stretching factors. It can be observed that the stretching factor  $\lambda_x = 2$  results in a significant hyper-viscosity since the deviation (3.205) in this case amounts to a large positive number. However, once the extended equilibrium (3.207) is used, the present model recovers the imposed viscosity, independent of the frame velocity and stretching factor.

#### 3.4.5.2 Decaying homogeneous isotropic turbulence

In order to validate the model as a reliable method for the simulation of complex flows and to show the application of using higher temperatures, decaying homogeneous isotropic turbulence was considered. The initial condition, in a box of the size  $L \times L \times L$ , was set at unit density and constant temperature along with a divergence-free velocity field, which follows the specified energy spectrum,

$$E(\kappa) = A\kappa^4 e^{-2(\kappa/\kappa_0)^2}, \quad (3.209)$$

where  $\kappa$  is the wave number,  $\kappa_0$  is the wave number at which the spectrum peaks and  $A$  is the parameter that controls the initial kinetic energy [115]. The initial velocity field is generated using a kinematic simulation as proposed in [116]. The turbulent Mach number is defined as,

$$\text{Ma}_t = \frac{\sqrt{\bar{\mathbf{u}} \cdot \bar{\mathbf{u}}}}{c_s}, \quad (3.210)$$

where  $c_s = \sqrt{T}$  is the speed of sound. The Reynolds number is based on the Taylor microscale,

$$\Lambda^2 = \frac{u_{\text{rms}}^2}{(\partial_x u_x)^2}, \quad (3.211)$$

and is given by

$$\text{Re}_\Lambda = \frac{\bar{\rho} u_{\text{rms}} \Lambda}{\mu}, \quad (3.212)$$

where  $u_{\text{rms}} = \sqrt{\bar{\mathbf{u}} \cdot \bar{\mathbf{u}}/3}$  is the root mean square (rms) of the velocity and overbar denotes the volume average over the entire computational domain.

Simulations were performed at  $\text{Ma}_t = 0.1$ ,  $\text{Re}_\Lambda = 72$ ,  $\kappa_0 = 16\pi/L$ , at two different temperatures,  $T = 1/3$  and  $T = 0.55$ , and with  $L = 256$  grid points. Fig. 3.11 shows a snapshot of the velocity magnitude  $\sqrt{\bar{\mathbf{u}} \cdot \bar{\mathbf{u}}}$  at time  $t^* = t/\tau = 1.0$ , where  $\tau = L_I/u_{\text{rms},0}$  is the eddy turnover time, which is defined based on the initial rms of the velocity and the integral length scale  $L_I = \sqrt{2\pi}/\kappa_0$ .

To quantitatively assess the accuracy of the model at different temperatures, the time evolution of the turbulent kinetic energy,

$$K = \frac{3}{2} u_{\text{rms}}^2, \quad (3.213)$$

normalized with its initial value ( $K_0$ ), and of the Taylor microscale Reynolds number are compared in Fig. 3.12 and Fig. 3.13 with results from direct numerical simulations (DNS) [115]. It is apparent that the two working temperatures yields almost identical results that agree well with the DNS simulation. This indicates that the correction terms do not degrade the accuracy of the model at higher temperatures, even though the magnitude of error term (3.205) is higher due to amplification of the linear term.

The immediate advantage of using the present model at a temperature higher than the lattice temperature  $T_L = 1/3$  is that it effectively increases



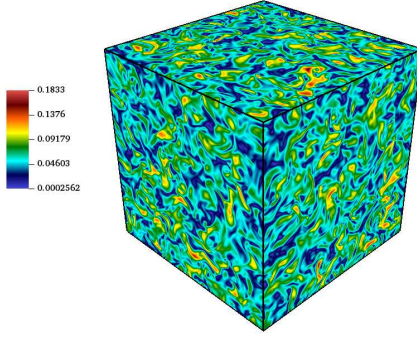


FIGURE 3.11: Velocity magnitude in lattice units for the decaying homogeneous isotropic turbulence at  $Ma_t = 0.1$ ,  $Re_\Lambda = 72$  and  $t^* = 1.0$  with temperature  $T = 0.55$ .

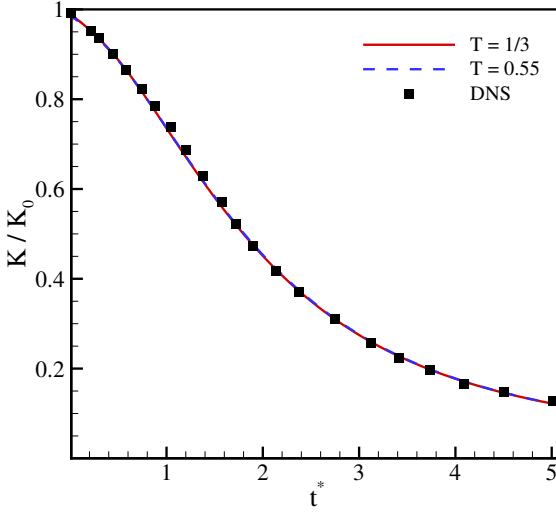


FIGURE 3.12: Time evolution of the turbulent kinetic energy for decaying isotropic turbulence at  $Ma_t = 0.1$ ,  $Re_\Lambda = 72$ . Lines: present model; symbol: DNS [115].

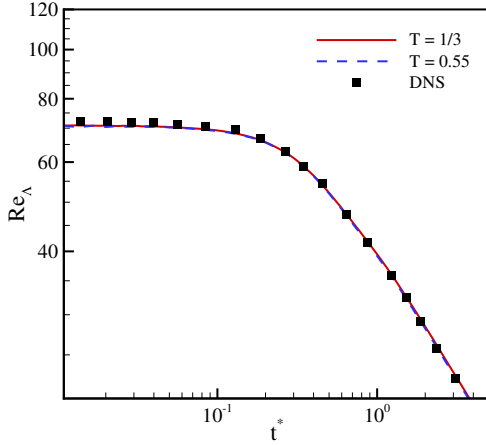


FIGURE 3.13: Time evolution of the Taylor microscale Reynolds number for decaying isotropic turbulence at  $Ma_t = 0.1$ ,  $Re_\Lambda = 72$ . Lines: present model; symbol: DNS [115]

the characteristic velocity (here  $u_{rms,0}$ ) and therefore the time step by a factor of  $\sqrt{T/T_L}$ . A larger time step is equivalent to fewer number of time steps. The present model, therefore, speeds up the simulation by a factor of  $\sqrt{T/T_L}$  compared to the conventional LBM, which can operate only at the lattice temperature  $T_L$ . Furthermore, this speedup strategy can be used for both steady and unsteady flows. This is in contrast to the preconditioned LBM [117], which works by altering the effective Mach number and therefore reduces the disparity between the speeds of the acoustic wave propagation and the waves propagating with the fluid velocity, cf. [117]. This makes preconditioned LBM restricted to steady state applications. In contrast, the present model enables us to increase the speed of sound without changing the Mach number. This increases the effective time step of the solver. Therefore, the present model increases the computational efficiency by decreasing the number of required time steps. Note that, the theoretical temperature range of the model (like any other models based on the D1Q3 lattice) is  $0 \leq T \leq 1$ , beyond that the populations become negative and the model is unstable. Therefore, while small temperature is possible but not beneficial, large temperature greater than 1 is out of the stability domain.

### 3.4.5.3 Periodic double shear layer

The next validation case to test the accuracy of the proposed model with the stretched lattice is the periodic double shear layer flow with the initial condition,

$$u_x = \begin{cases} u_0 \tanh(\alpha(y/L - 0.25)), & y \leq L/2, \\ u_0 \tanh(\alpha(0.75 - y/L)), & y > L/2, \end{cases} \quad (3.214)$$

$$u_y = \delta u_0 \sin(2\pi(x/L + 0.25)), \quad (3.215)$$

where  $L$  is the domain length in both  $x$  and  $y$  directions,  $u_0 = 0.1$  is characteristic velocity,  $\delta = 0.05$  is a perturbation of the  $y$ -velocity and  $\alpha = 80$  controls the width of the shear layer. The Reynolds number is set to  $Re = u_0 L / \nu = 10^4$  and the temperature is  $T = 1/3$ . Fig. 3.14 shows

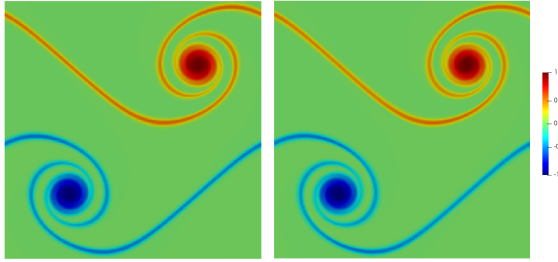


FIGURE 3.14: Vorticity field for double shear layer flow at  $t^* = 1$  with regular lattice (left) and stretched lattice (right). Vorticity magnitude is normalized by its maximum value.

the vorticity field at non-dimensional time  $t^* = tu_0/L = 1$  using the conventional square lattice  $\lambda_x = \lambda_y = 1$  and the rectangular lattice with  $\lambda_x = 2$ ,  $\lambda_y = 1$ . Both lattice models perform qualitatively same.

To quantify the effect of stretching on the accuracy, the time evolution of the mean kinetic energy and of the mean enstrophy  $\Omega = \overline{\omega^2} / \frac{u_0^2}{L^2}$ , with  $\omega$  the vorticity magnitude, are compared in Fig. 3.15. The results show only minor discrepancies, which indicates the validity of the model also on stretched meshes.

### 3.4.5.4 Laminar boundary layer over a flat plate

The next test case validates our model for wall-bounded flows with rectangular lattice. We consider the laminar flow over a flat plate with an

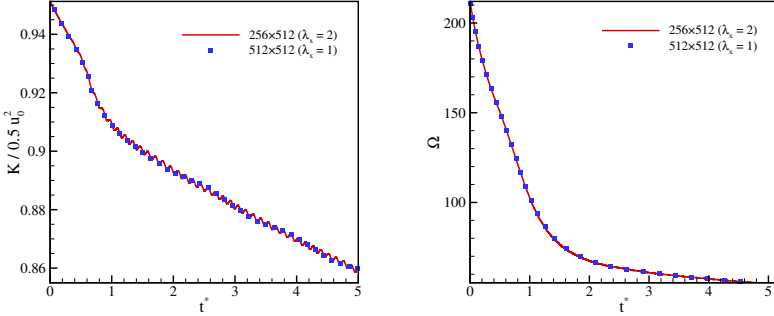


FIGURE 3.15: Evolution of kinetic energy (left) and enstrophy (right) for double shear layer flow at  $Re = 10^4$ .

incoming Mach number  $Ma_\infty = u_\infty / \sqrt{T_\infty} = 0.1$ , temperature  $T_\infty = 1/3$  and Reynolds number  $Re = \rho_\infty u_\infty L / \mu = 4000$ , where  $L$  is the length of flat plate. Since the flow gradients in the transverse  $y$ -direction are much larger compared to the gradients in the streamwise  $x$ -direction, the mesh can be stretched in  $x$ -direction without significantly affecting the accuracy of the results. The computational domain was set to  $[L_x \times L_y] = [200 \times 200]$  and a rectangular lattice with  $\lambda_x = 2$  was used. The flat plate starts at a distance of  $L_x/4$  from the inlet and symmetry boundary conditions were imposed at  $0 \leq x \leq L_x/4$ . In Fig. 3.16, the horizontal velocity profile at the end of the plate is compared with the results of a regular lattice and with the Blasius similarity solution, where  $\eta$  is the dimensionless coordinate [118],

$$\eta = y \sqrt{\frac{u_\infty}{\nu x}}. \quad (3.216)$$

It can be seen that results for the regular and the rectangular lattice nearly coincide and agree well with the Blasius solution. Thus, the model achieves accurate results with half of grid points compared to the regular lattice. Furthermore, the distribution of skin friction coefficient over the plate,

$$c_f = \frac{\tau_{\text{wall}}}{\frac{1}{2} \rho_\infty u_\infty^2}, \quad (3.217)$$

with the wall shear stress  $\tau_{\text{wall}} = \mu (\frac{\partial u}{\partial y})_{y=0}$ , is shown in Fig. 3.17 in comparison with the analytical solution  $c_f = 0.664 / \sqrt{Re_x}$ , where  $Re_x = u_\infty x / \nu$  [118]. Also here, the results of the model with the regular and the stretched

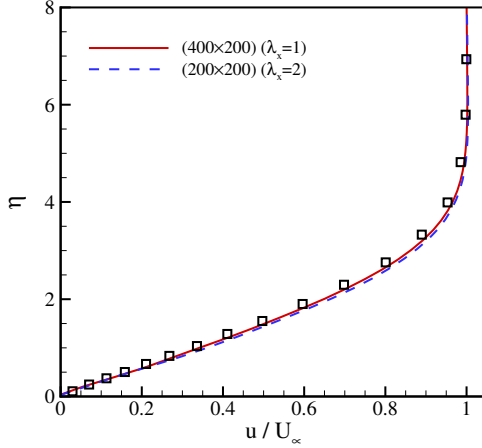


FIGURE 3.16: Comparison of the velocity profile at  $x = L_x$  for flow over a flat plate at different stretching ratios. Lines: present model; symbols: Blasius solution.

velocities are almost identical and in good agreement with the analytical solution.

#### 3.4.5.5 Turbulent channel flow

In the final test case, we assess the accuracy and performance of the incompressible extended LBM for the turbulent flow in a rectangular channel, for which many numerical [119–121] and experimental [122, 123] results are available. The channel geometry was chosen as  $[5.6H \times 2H \times 2H]$ , where  $H$  is the channel half-width. The friction Reynolds number,

$$\text{Re}_\tau = \frac{u_\tau H}{\nu}, \quad (3.218)$$

based on the friction velocity  $u_\tau = \sqrt{\tau_w / \rho}$ , was set to  $\text{Re}_\tau = 180$ . The initial friction velocity was estimated by

$$u_\tau = \frac{u_0}{\frac{1}{\mathcal{K}} \ln \text{Re}_\tau + 5.5}, \quad (3.219)$$

where  $\mathcal{K} = 0.41$  is the von Kármán constant and  $u_0 = 0.1$  is the mean center-line velocity. Periodic boundary conditions were imposed in the

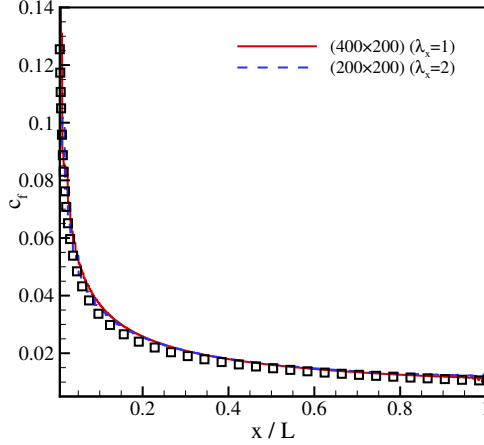


FIGURE 3.17: Comparison of the skin friction coefficient for flow over a flat plate at different stretching ratio. Lines: present model; symbols: analytical solution.

streamwise  $x$ -direction and the spanwise  $z$ -direction. The flow was driven by a constant body force in the  $x$ -direction,

$$g = \text{Re}_\tau^2 \nu^2 / H^3. \quad (3.220)$$

In order to accelerate the transition to turbulence, a non-uniform divergence-free forcing field as proposed in [124] was added to the flow for some period of time, until  $t^* = tH/u_\tau = 5$ .

Similar to the previous test case, grid stretching in  $x$ -direction with  $\lambda_x = 1.4$  was used in order to reduce the number of grid points in that direction while the temperature was set to  $T = 0.55$ , same as in Sec. 3.4.5.2. A snapshot of the velocity magnitude  $\sqrt{\mathbf{u} \cdot \mathbf{u}}$  is shown in Fig. 3.18. Quantitatively, we compare the mean velocity profile with the DNS results of [120] in Fig. 3.19. In wall units, the mean velocity is given by  $u^+ = \bar{u}/u_\tau$  and the spatial coordinate is  $y^+ = yu_\tau/\nu$ . The statistics are collected after 30 eddy turnover times, i.e., after  $t^* = 30$ . It is apparent that the viscous sublayer ( $y^+ < 5$ ), the buffer layer ( $5 < y^+ < 30$ ) and the log-law region ( $y^+ > 30$ ) are captured well with our model and the mean velocity profile agrees well with that of the DNS.

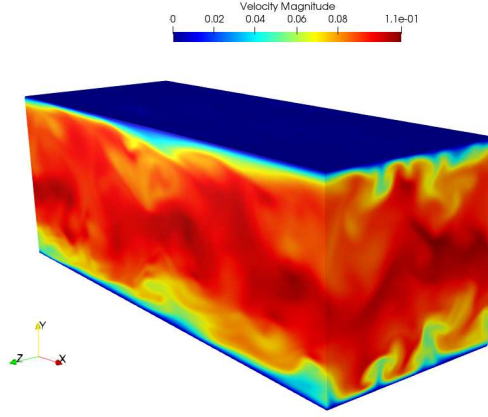


FIGURE 3.18: Snapshot of the velocity magnitude in lattice units for turbulent channel flow at  $Re_\tau = 180$  with  $\lambda_x = 1.4$ .

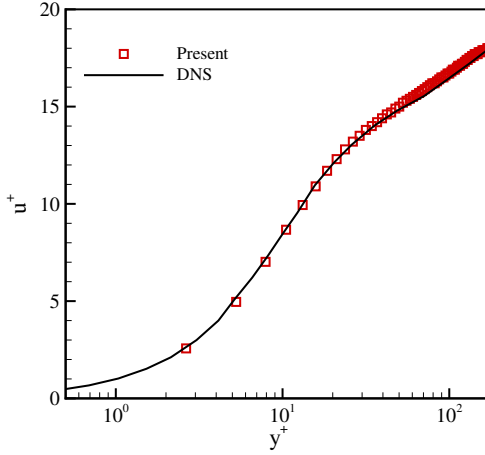


FIGURE 3.19: Comparison of the mean velocity profile in a turbulent channel flow at  $Re_\tau = 180$  with  $\lambda_x = 1.4$ .

For a more thorough analysis, we compare the root mean square of the velocity fluctuations with the DNS data in Fig. 3.20. Here,  $u_{x,rms} =$

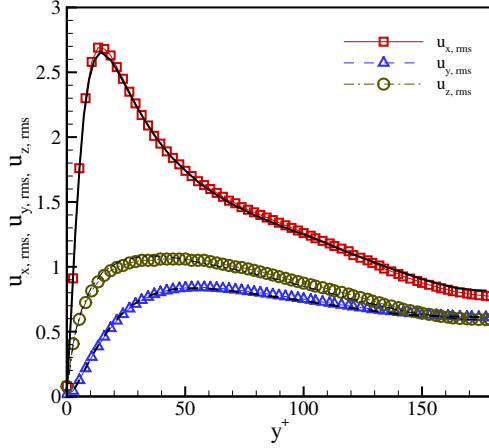


FIGURE 3.20: Comparison of the rms of the velocity fluctuations in a turbulent channel flow at  $Re_\tau = 180$  with  $\lambda_x = 1.4$ . Symbols: present model; lines: DNS [120].

$\sqrt{u'_x u'_x}$  and  $u_{y,rms}$  and  $u_{z,rms}$  are defined in a similar way. It can be seen that the results are in excellent agreement with the DNS results [120]. This demonstrates that the LBGK model, also in the presence of a severe anisotropy triggered by stretched velocities, can be used for the simulation of high Reynolds number wall-bounded flows once the corrections are incorporated with the extended equilibrium.

### 3.5 CONCLUSION

Two different realizations of extended lattice Boltzmann model for compressible flows have been proposed. Extended model I removes the anomalous term in the momentum equation at the level of second-order kinetic equations. This results in a force term that contains second derivative of the deviation.

Contrary to that, in extended model II, the spurious term is canceled out at the level of first-order kinetic equations by redefining the equilibrium (extended equilibrium) to correct the nonequilibrium pressure tensor. This results in a simpler formulation compared to model I, that will be easily extended to supersonic flows in the next chapter. Another modification in



model II is the use of the product-form formulation of equilibrium for the total energy population which recovers all Maxwell–Boltzmann moments supported by the stencil. It was shown that both models are Galilean invariant and isotropic and recover the same equations in the hydrodynamic limit.

Finally, the benefits of using the extended equilibrium in the incompressible regime were discussed.



## EXTENSION TO SUPERSONIC FLOWS

---

### 4.1 INTRODUCTION

The compressible lattice Boltzmann models described in the previous chapter can successfully simulate compressible flows in subsonic and transonic regimes with Mach number range up to  $\sim 0.9$ . However, supersonic flows involving shock waves are indispensable part of the compressible flows. In this chapter, we tackle the problem of supersonic flows using two approaches. First, is the concept of the *shifted lattices* [125], a general approach to increase the operating range of any LB model. With the shifted lattice, the Mach number range can be increased up-to  $\text{Ma} = 2.5$ . Its drawback when coupled with standard lattices, however, is loss of the exact space discretization and the need for interpolation during the propagation step.

The second approach works by using the first-order upwind scheme for the discretization of correction term as opposed to second-order central scheme. This approach is only applicable to model II, and thus provides a way to simulate moderately supersonic regime while maintaining the simplicity and accuracy of the on-lattice propagation.

### 4.2 CONCEPT OF THE SHIFTED LATTICES

It is well known that, at higher flow speeds and at temperatures other than the lattice temperature  $T_L = 1/3$ , the magnitude of the deviations (3.38) and consequently the correction terms become large, which leads to instability of the model. However, operating range of the compressible LB model can be extended to supersonic flows by applying the concept of shifted lattices [125]. With shifted lattices the local equilibria, and hence the corresponding deviations from the Maxwell-Boltzmann relations, are written in a reference frame moving with a constant predefined velocity  $U$ . Therefore, deviations in the equilibria (3.38) are minimized whenever the flow velocity is around  $U$ . In other words, the operating range of the model is shifted to a Mach number range of  $\sim 0.9$  around the reference frame velocity  $U$ .

Here, we consider the case  $\mathbf{U} = (U, 0)$  (moving reference frame in  $x$ -direction) and, therefore, the  $x$ -component of the discrete velocities becomes,

$$c'_{ix} = c_{ix} + U. \quad (4.1)$$

The local equilibria in a moving reference frame are computed assuming that moments are invariant with respect to the reference frame, as was recently suggested in [126]. Therefore, one can match  $Q$  linearly independent moments of the equilibrium in the rest and moving reference frames. For example, in 2D and for the  $f$ -populations, the matching conditions read [126],

$$\sum_{i=0}^{Q-1} f_i^{\text{eq}} c_{ix}^m c_{iy}^n = \sum_{i=0}^{Q-1} f_i'^{\text{eq}} c_{ix}^m c_{iy}^n, \quad (4.2)$$

where  $f_i'^{\text{eq}}$  is the equilibrium population in the moving reference frame and  $m$  and  $n$  are integers corresponding to linearly independent moments. The matching conditions (4.2) can be written in a matrix form as,

$$\mathcal{M} f^{\text{eq}} = \mathcal{M}' f'^{\text{eq}}, \quad (4.3)$$

where  $\mathcal{M}$  and  $\mathcal{M}'$  are  $Q \times Q$  matrix and equilibrium population in the moving reference frame is then computed as, [126]

$$f'^{\text{eq}} = \mathcal{G} f^{\text{eq}} = \mathcal{M}'^{-1} \mathcal{M} f^{\text{eq}}, \quad (4.4)$$

where  $\mathcal{G}$  is the transfer matrix that maps equilibrium populations from the rest reference frame to the moving reference frame (see Appendix A.2 for the explicit form of  $\mathcal{G}$ ). The explicit form of the  $f$ -equilibrium in the moving reference frame can be obtained by setting,

$$\zeta'_\alpha = u_\alpha - U_\alpha, \quad (4.5)$$

$$\mathcal{P}_{\alpha\alpha}'^{\text{eq}} = RT + (u_\alpha - U_\alpha)^2. \quad (4.6)$$

Substituting (4.5) and (4.6) into (3.27), we obtain,

$$\boxed{f_i'^{\text{eq}} = \rho \Psi_{c_{ix}}(u'_x, \mathcal{P}_{xx}'^{\text{eq}}) \Psi_{c_{iy}}(u'_y, \mathcal{P}_{yy}'^{\text{eq}}).} \quad (4.7)$$

The equilibrium and quasi-equilibrium of the  $g$ -populations in the moving reference frame are computed in the same way. The final form in 2D is

$$G_{(0,0)} = M_0 \left( 1 - U^2 - T + 2T^2 \right) + M_x 2U (1 - T) - M_{xx} \frac{1}{2} (1 + T) + M_{yy} \frac{1}{2} \left( 2U^2 - 1 - T \right), \quad (4.8)$$

$$G_{(\sigma,0)} = M_0 \left( \frac{U^2}{2} - \sigma \frac{U}{2} + \frac{1}{2} T - T^2 \right) - M_x \left( U - \frac{\sigma}{2} \right) (1 - T) + M_{xx} \frac{1}{4} (1 + T) + M_{yy} \frac{1}{4} \left( -2U^2 + 2\sigma U + T - 1 \right), \quad (4.9)$$

$$G_{(0,\lambda)} = M_0 \left( \frac{T}{2} - T^2 \right) + M_y \lambda \left( \frac{1}{2} - \frac{U^2}{2} - \frac{T}{2} \right) + M_x UT - M_{xx} \frac{1}{4} (1 - T) + M_{xy} \lambda (U) + M_{yy} \frac{1}{2} \left( \frac{1}{2} - U^2 + \frac{T}{2} \right), \quad (4.10)$$

$$G_{(\sigma,\lambda)} = M_0 \left( -\frac{T}{4} + \frac{T^2}{2} \right) + M_x T \left( -\frac{U}{2} + \sigma \frac{1}{4} \right) + M_y \left( \frac{\lambda}{4} \left( U^2 + T - \sigma U \right) \right) + M_{xx} \frac{1}{8} (1 - T) + M_{xy} \left( \sigma \lambda \frac{1}{4} - \lambda \frac{U}{2} \right) + M_{yy} \frac{1}{2} \left( \frac{U^2}{2} - \sigma \frac{U}{2} + \frac{1 - T}{4} \right), \quad (4.11)$$

where  $\sigma, \lambda = \{+1, -1\}$  and the two indices are identified with the components of the discrete velocity vectors  $G_{(c_{ix}, c_{iy})}$  and, thus, enumerate all nine populations. The moments required for the computations are provided in in Table 3.1.

In summary, the kinetic equations of model I, with shifted lattice can be written as,

$$f'_i(\mathbf{x} + \mathbf{c}'_i \delta t, t + \delta t) - f'_i(\mathbf{x}, t) = \omega(f_i^{\text{eq}} - f'_i) + \phi_i, \quad (4.12)$$

$$g'_i(\mathbf{x} + \mathbf{c}'_i \delta t, t + \delta t) - g'_i(\mathbf{x}, t) = \omega(g_i^{\text{eq}} - g'_i) + (\omega_1 - \omega)(g_i^{I*} - g_i^I). \quad (4.13)$$

The conservation laws are,

$$\rho = \sum_{i=0}^{Q-1} f'_i = \sum_{i=0}^{Q-1} f_i^{\text{eq}}, \quad (4.14)$$

$$\rho \mathbf{u} = \sum_{i=0}^{Q-1} \mathbf{c}'_i f'_i = \sum_{i=0}^{Q-1} \mathbf{c}'_i f_i^{\text{eq}}, \quad (4.15)$$

$$\rho E = \sum_{i=0}^{Q-1} g'_i = \sum_{i=0}^{Q-1} g_i^{\text{eq}}, \quad (4.16)$$

and equilibrium and quasi-equilibrium populations for  $f_i$   $g_i$  are computed using (4.7) and (4.8-4.11), respectively. The formulation of  $\phi_i$  correction terms do not change, with the note that the deviation  $\tilde{Q}_{xxx}$  should now be computed in the moving reference frame,

$$\tilde{Q}_{xxx} = \rho (u - U) (1 - 3RT) - \rho(u - U)^3. \quad (4.17)$$

#### 4.2.1 Shock-vortex interaction

Sound generation by a vortex passing through a shock wave [127] is studied to assess the performance and accuracy of the model I with shifted lattices for supersonic flows involving shock. This problem consists of an isentropic vortex, with vortex Mach number  $\text{Ma}_v$ , initially in the upstream shock region, which is passed through a stationary shock wave at advection Mach number  $\text{Ma}_a = 1.2$  with the left state  $(\rho, T, u_x, u_y)_l = (1, 0.05, \text{Ma}_a \sqrt{\gamma T_l}, 0)$  and Rankine-Hugoniot right state. The initial field with standing shock  $(\rho_\infty, P_\infty, u_{x,\infty}, u_{y,\infty})$  is perturbed with an isentropic vortex with radius  $r_v$  centered at  $(x_v, y_v)$  [127]

$$\rho = \rho_\infty \left[ 1 - \frac{\gamma - 1}{2} \text{Ma}_v^2 e^{(1-r^2)} \right]^{1/(\gamma-1)}, \quad (4.18)$$

$$P = P_\infty \left[ 1 - \frac{\gamma - 1}{2} \text{Ma}_v^2 e^{(1-r^2)} \right]^{\gamma/(\gamma-1)}, \quad (4.19)$$

$$u_x = u_{x,\infty} + \sqrt{\gamma T_l} \text{Ma}_v \frac{(y - y_v)}{r_v} e^{(1-r^2)/2}, \quad (4.20)$$

$$u_y = u_{y,\infty} - \sqrt{\gamma T_l} \text{Ma}_v \frac{(x - x_v)}{r_v} e^{(1-r^2)/2}, \quad (4.21)$$

where  $r = \sqrt{(x - x_v)^2 + (y - y_v)^2} / r_v$  is the reduced radius and the shock is initially located at  $x_s = 8r_v$ .

We perform a simulation with  $\text{Ma}_a = 1.2$ ,  $\text{Ma}_v = 0.25$ , where the Reynolds number is set to  $\text{Re} = \frac{\rho_l c_{s,l} r_v}{\mu} = 800$ ,  $c_{s,l}$  is the speed of sound upstream of the shock, and the Prandtl number is  $\text{Pr} = 0.75$ . The computational domain size is  $L_x \times L_y = 1680 \times 1440$ , the vortex radius is  $r_v = L_x/28$  and the vortex center is at  $(x_v, y_v) = (6r_v, L_y/2)$ .

Shifted velocity  $U$  should be chosen in such a way that the operating range of the model covers the Mach number range of the problem. For example, shifted lattice with velocity  $U = 1$  is not a good choice here, as it corresponds to the shifted Mach number  $\text{Ma}_{\text{shifted}} = U/\sqrt{\gamma T} \approx 2.6$ . Therefore, a shifted lattice with velocity  $U = 0.5$  ( $\text{Ma}_{\text{shifted}} \approx 1.3$ ) is considered for this problem. However, in this case we do not have a space filling lattice anymore and interpolation is required during the propagation step to reconstruct populations at the grid points [126]:

$$f'_i(\mathbf{x}, t) = \sum_{s=1}^k L_s(\mathbf{x} - \mathbf{x}_s) f'_i(\mathbf{x}_s, t), \quad (4.22)$$

where  $L_s$  are Lagrange polynomials using the collocation points  $\mathbf{x}_s, s = 1, \dots, k$  around point  $\mathbf{x}$  and  $k = 3$  (third-order accurate).

To quantify the accuracy of the computations, the distribution of radial sound pressure is plotted in Fig. 4.1 in comparison with the DNS results [127]. The sound pressure is defined as,  $\Delta P = (P - P_s)/P_s$ , where  $P_s$  is the pressure behind the shock wave and is measured in the radial direction with the origin at the vortex center, at an angle  $\theta = -45^\circ$  and at three different non-dimensional times  $t^* = 6, 8, 10$ , where  $t^* = tc_{s,l}/r_v$ . Excellent agreement is observed between the present model and the DNS [127]. Note that the sound pressure is typically a small perturbation (around 1%) on top of the hydrodynamic pressure. This shows that the present model with the LBGK collision term can accurately capture moderately supersonic shock waves.

Finally, Fig. 4.2 shows the sound pressure contours of a pair of vortices interacting with the shock wave at  $t^* = 5$ . The simulation parameters are the same as a single vortex and in accordance with [127]. The shock wave deformation caused by the interaction with the pair of vortices is evident and symmetry of the results further supports the accuracy of the present computation. Again, good agreement can be seen between the present model and DNS.

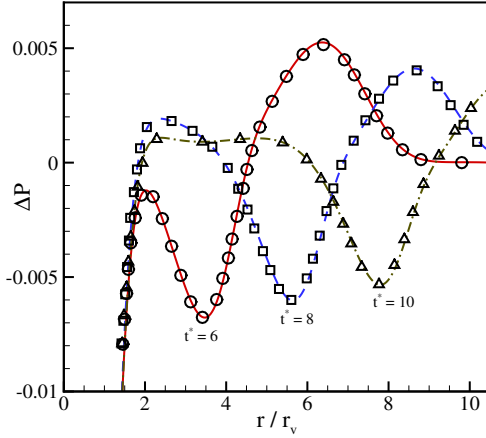


FIGURE 4.1: Comparison of radial sound pressure distribution  $\Delta P$  for  $\text{Ma}_a = 1.2$ ,  $\text{Ma}_v = 0.25$  and  $\text{Re} = 800$  with the DNS results at three different times  $t^* = 6, 8, 10$ . Lines: present model I; symbol: DNS [127].

#### 4.3 UPWIND DISCRETIZATION OF CORRECTION TERM IN MODEL II

The spatial discretization of the deviation  $\tilde{Q}$  in (3.116) and (3.123) has important effect on stability of the extended model II, especially in the case of supersonic flows where discontinuities emerge in the flow field. It has been shown through linear stability analysis [88] that, while second-order central difference scheme provides good stability domain in the subsonic regime, the first-order upwind scheme is necessary for maintaining the stability in the supersonic regime and capturing shock wave. We should emphasize that, this is only true for the model II, where the correction term contains first derivative of deviation. According to linear stability analysis [88], upwind discretization of corrections in model I, does not increase its stability domain. We, therefore, employ the first-order upwind scheme in model II, in order to have a wider stability domain.

For example, the  $x$ -derivative of the deviation  $\tilde{Q}_{xxx}$  at grid point  $x_{i,j,k}$  can be written as,

$$\partial_x \tilde{Q}_{xxx,i,j,k} = \frac{\tilde{Q}_{xxx,(i+1/2,j,k)} - \tilde{Q}_{xxx,(i-1/2,j,k)}}{\Delta x}, \quad (4.23)$$



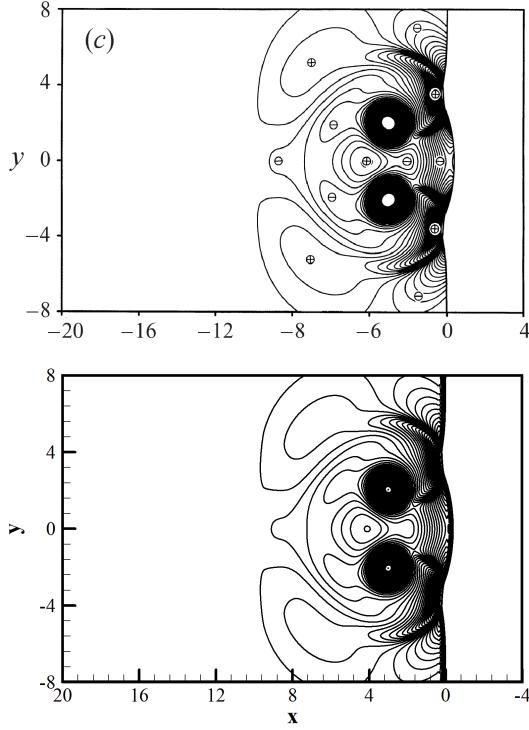


FIGURE 4.2: Snapshot of sound pressure  $\Delta p$  contours for a passing vortex pair with  $Ma_a = 1.2$ ,  $Ma_v = 0.25$  and  $Re = 800$  at  $t^* = 5$ . Contour levels are from  $\Delta P_{min} = -0.14$  to  $\Delta P_{max} = 0.12$  with an increment of 0.0039. Top: DNS [127],  $\oplus$  denotes the compression region ( $\Delta P > 0$ ) while  $\ominus$  denotes the rarefaction region ( $\Delta P < 0$ ); Bottom: present model I.

where (omitting  $xxx$  and  $j, k$  indices)  $\tilde{Q}_{i+1/2}$  and  $\tilde{Q}_{i-1/2}$  are upwind reconstruction of  $\tilde{Q}$  at the interface  $x_{i\pm 1/2, j, k}$ ,

$$\tilde{Q}_{i+1/2} = \begin{cases} \tilde{Q}_i, & \text{if } u_x > 0, \\ \tilde{Q}_{i+1}, & \text{otherwise,} \end{cases} \quad (4.24)$$

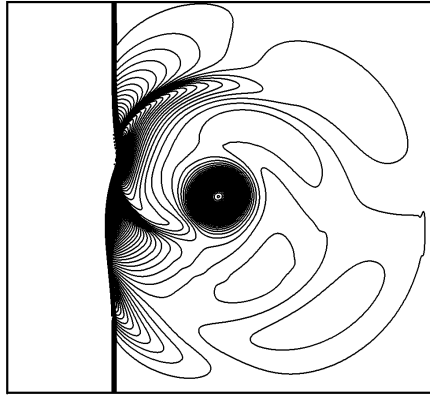


FIGURE 4.3: The sound pressure field  $\Delta P$  of model II for the shock-vortex interaction with  $Ma_a = 1.2$ ,  $Ma_v = 0.25$  and  $Re = 800$  at  $t^* = 6$ . The contour levels are from  $\Delta P_{min} = -0.48$  to  $\Delta P_{max} = 0.16$  with an increment of 0.003216.

#### 4.3.1 Shock-vortex interaction with on-lattice model II

We repeat the simulation of shock-vortex interaction, with the same setup presented above, but now with on-lattice model II. Fig. 4.3 shows the sound pressure contours at time  $t^* = 6$ . The shock wave deformation caused by the interaction with the vortex is observed. To quantify the accuracy of the computations, the radial sound pressure distribution is plotted in Fig. 4.4 in comparison with the DNS results [127]. Again, good agreement can be observed between the on-lattice model II and DNS.

## 4.4 CONCLUSION

Two strategies for extending the operating range of extended models, introduced in Chapter 3, to supersonic flows with shock waves have been discussed. First, use of shifted lattices, which shifts the operating range of any LB model in terms of Mach number, however, comes at the price of losing the exact on-lattice propagation. Moreover, this strategy is more effective in flows where the mean flow has a preferential direction, like flow

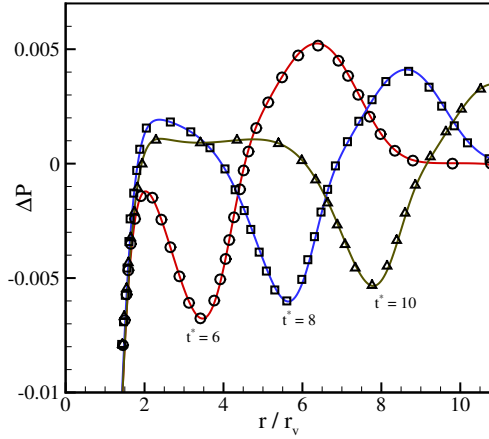


FIGURE 4.4: Comparison of radial sound pressure distribution  $\Delta P$  for  $Ma_q = 1.2$ ,  $Ma_v = 0.25$  and  $Re = 800$  with the DNS results at three different times  $t^* = 6, 8, 10$ . Lines: present model II; symbol: DNS [127].

over airfoil which will be presented in the next chapter.

The second strategy was based on upwind-discretization of correction terms in model II to enhance the stability of high Mach flows. With this strategy, the resulting on-lattice model covers a wide range of fluid flows, from low Mach weakly compressible to transonic and moderately supersonic regimes with shock waves.



UNSTRUCTURED AND MOVING MESHES

---

*Total science is like a field of force whose boundary conditions are experience. A conflict with experience at the periphery occasions readjustments in the interior of the field.*

— Willard Quine

## 5.1 INTRODUCTION

In this chapter, we extend the model formulation to unstructured finite element meshes using a semi-Lagrangian propagation scheme and introduce consistent wall boundary conditions for the simulation of complex geometries. Similar to the standard LBM, the semi-Lagrangian scheme follows the characteristics curve of the LB equation backward in time to find the departure point of each grid node. However, since the propagation is performed on an arbitrary non-uniform grid, interpolation is required to reconstruct the populations at the departure points. Finite element based interpolation schemes are good candidates as they allow to have body-conforming meshes which give more flexibility in handling complex geometries and are more efficient in capturing small scale structure of the flow near the wall. Another advantage of the semi-Lagrangian scheme is that the time step can be chosen arbitrarily and it remains stable at large Courant-Friedrichs-Lewy (CFL) numbers. This is at variance to many other off-lattice schemes (such as finite-difference or finite-volume LB schemes) which operate at restricted CFL number due to explicit time integration, see e.g., [128]. Note that, finite-element based semi-Lagrangian scheme has successfully been applied to incompressible LB models [105, 129]. Here, we apply the semi-Lagrangian scheme with second-order accurate finite element interpolation to the extended compressible LB model I [87] to test its capabilities for simulation of compressible flows on unstructured grid.

Although by using unstructured mesh it is not possible to take advantage of the exact on-lattice propagation, the computational overhead of performing interpolation in the present model with the  $D2Q9$  lattice and the BGK collision term, is largely, if not fully, compensated by the reduction in computational cost related to the smaller lattice and simple collision

term. Moreover, with the finite-element interpolation used in this work the computations in each element depend only on the values from itself and its next neighboring elements. This feature greatly simplifies the parallel implementation of the model, which is necessary for the large scale three dimensional simulations.

## 5.2 SEMI-LAGRANGIAN PROPAGATION

The semi-Lagrangian propagation is a practical generalization of standard LB propagation, which removes the restriction related to the regular lattice by performing interpolation in order to find the solution at the departure points [105]. Here, we employ the second-order finite element interpolation scheme to reconstruct solution at the departure points. An example of a semi-Lagrangian propagation on a second-order finite element mesh with nine collocation points is presented in Fig. 5.1. It has been shown that

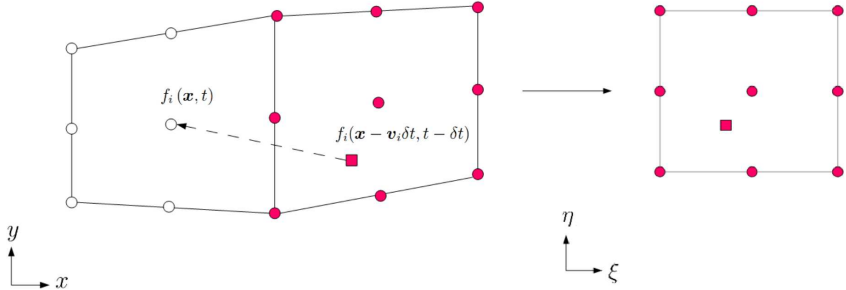


FIGURE 5.1: Schematic of a second-order finite element mesh, the semi-Lagrangian propagation along the discrete velocity  $v_i$  and mapping from the global coordinate  $(x, y)$  to local coordinate  $(\xi, \eta)$ .

this type of reconstruction is less dissipative compared to other off-lattice schemes [105] and also it has been applied successfully to LB for simulation of incompressible turbulent flows [129].

The semi-Lagrangian propagation at the departure point of characteristic lines  $x - c_i \delta t$  is then written as,

$$f_i(x, t) = f_i(x - c_i \delta t, t - \delta t) = \sum_{s=1}^9 f_i(\xi_s, t - \delta t) N_s(\xi_{dp}), \quad (5.1)$$

where  $N_s(\xi_{dp})$  denotes the values of the shape functions, written in the local coordinate system  $\xi = (\xi, \eta)$ ,  $(-1 \leq \xi, \eta \leq 1)$ , at the departure point

(red square in Fig. 5.1), and  $s = 9$  is number of collocation points. Here, the second-order quadratic shape functions are used as follows [130],

$$N_1 = \frac{1}{4}\xi\eta(\xi-1)(\eta-1), \quad N_2 = \frac{1}{4}\xi\eta(\xi+1)(\eta-1), \quad (5.2)$$

$$N_3 = \frac{1}{4}\xi\eta(\xi+1)(\eta+1), \quad N_4 = \frac{1}{4}\xi\eta(\xi-1)(\eta+1), \quad (5.3)$$

$$N_5 = \frac{1}{2}\eta(1-\xi^2)(\eta-1), \quad N_6 = \frac{1}{2}\xi(\xi+1)(1-\eta^2), \quad (5.4)$$

$$N_7 = \frac{1}{2}\eta(1-\xi^2)(\eta+1), \quad N_8 = \frac{1}{2}\xi(\xi-1)(1-\eta^2), \quad (5.5)$$

$$N_9 = (1-\xi^2)(1-\eta^2). \quad (5.6)$$

Therefore, semi-Lagrangian propagation on unstructured finite element mesh requires two steps:

First, computing the local coordinates of the departure point  $\xi_{dp}$  (see Fig. 5.1) which, for quadrilateral elements, involves solving a non-linear system of equations resulting from,

$$\mathbf{x}_{dp} = \sum_{s=1}^4 \mathbf{x}_s N_s(\xi_{dp}), \quad (5.7)$$

where in order to simplify the computation, four vertices are used to define shape functions,

$$N_1 = \frac{1}{4}(1-\xi)(1-\eta), \quad N_2 = \frac{1}{4}(1+\xi)(1-\eta), \quad (5.8)$$

$$N_3 = \frac{1}{4}(1+\xi)(1+\eta), \quad N_4 = \frac{1}{4}(1-\xi)(1+\eta). \quad (5.9)$$

Second, the values of the populations at the departure point are computed by means of the values of the populations at collocation points (red circles) using (5.1).

After the propagation, the correction terms  $\phi_i$  should be evaluated. However, the computation of correction terms requires the knowledge of spatial gradients for deviation terms (3.38). This is done using the finite element formula for the first-order derivative. For a generic variable  $Q$ , we can write,

$$\partial_x Q = \mathbf{J}^{-1} \sum_s Q_s \partial_\xi N_s, \quad (5.10)$$

where  $Q_s$  are the values of  $Q$  at collocation points and  $\mathbf{J}^{-1}$  is the inverse of the Jacobian matrix of transformation computed with,

$$\mathbf{J}^{-1} = \frac{1}{\det \mathbf{J}} \begin{bmatrix} \partial_\eta y & -\partial_\xi y \\ -\partial_\eta x & \partial_\xi x \end{bmatrix}, \quad (5.11)$$

and

$$\det \mathbf{J} = \partial_\xi x \partial_\eta y - \partial_\xi y \partial_\eta x, \quad (5.12)$$

is the determinant of the Jacobian matrix. The metrics of transformation  $\partial_\xi x, \partial_\eta x, \partial_\xi y, \partial_\eta y$  are computed with the following formula,

$$\partial_\xi x = \sum_s x_s \partial_\xi N_s. \quad (5.13)$$

Note that, the nodes on the element edges are assigned to the element with the larger area.

Finally, the post-collision populations are computed in the conventional way as in the standard LB method.

### 5.2.1 Wall boundary conditions

Semi-Lagrangian propagation on unstructured grid makes it possible to employ body-fitted mesh and simulate complex geometries. Therefore, an appropriate wall boundary condition (BC) is required. Here, we follow the approach proposed by [114, 131] and replace the missing populations during propagation with the following expression,

$$f_i^{\text{miss}} = f_i^{\text{eq}}(\rho_{tgt}, \mathbf{u}_{tgt}, T_{tgt}) + \delta t f_i^{(1)}(\rho_{tgt}, \mathbf{u}_{tgt}, T_{tgt}, \mathbf{u}_{tgt}, T_{tgt}), \quad (5.14)$$

$$g_i^{\text{miss}} = g_i^{\text{eq}}(\rho_{tgt}, \mathbf{u}_{tgt}, T_{tgt}) + \delta t g_i^{(1)}(\rho_{tgt}, \mathbf{u}_{tgt}, T_{tgt}, \mathbf{u}_{tgt}, T_{tgt}), \quad (5.15)$$

where  $f_i^{\text{eq}}, g_i^{\text{eq}}$  are equilibrium parts computed from (4.7) and (4.8) to (4.11),  $f_i^{(1)}, g_i^{(1)}$  are non-equilibrium parts and  $\rho_{tgt}, \mathbf{u}_{tgt}$  and  $T_{tgt}$  are target values which need to be specified.

The non-equilibrium parts are obtained based on the Grad's approximation and using the general formula (3.45) with the non-equilibrium moments given in Table 5.1 [79, 132],



$G_i$	$M_0$	$M_\alpha$	$M_{\alpha\beta}$
$f_i^{(1)}$	0	0	$P_{\alpha\beta}^{(1)}$
$g_i^{(1)}$	0	$q_\alpha^{(1)}$	$R_{\alpha\beta}^{(1)}$

TABLE 5.1: Moments needed for the computation of  $f_i^{(1)}$  and  $g_i^{(1)}$ .

$$P_{\alpha\beta}^{(1)} = -\frac{1}{\omega} \rho T \left( S_{\alpha\beta} - \frac{1}{C_v} \partial_\gamma u_\gamma \delta_{\alpha\beta} \right), \quad (5.16)$$

$$q_\alpha^{(1)} = -\frac{1}{\omega_1} \rho C_p T \partial_\alpha T + u_\beta P_{\alpha\beta}^{(1)}, \quad (5.17)$$

$$R_{\alpha\beta}^{(1)} = -\frac{1}{\omega_1} \rho T [S_{\alpha\beta} (E + 2T) + u_\alpha \partial_\beta E + u_\beta \partial_\alpha E], \quad (5.18)$$

where  $S_{\alpha\beta}$  is the strain rate tensor.

For computing target values, if missing populations belong to points on the wall (black circles in Fig. 5.2), target velocities are zero,  $\mathbf{u}_{tgt} = \mathbf{0}$  and target density and temperature (for adiabatic wall) are obtained by setting,

$$\frac{\partial \rho}{\partial \mathbf{n}}|_{wall} = 0, \quad (5.19)$$

$$\frac{\partial T}{\partial \mathbf{n}}|_{wall} = 0, \quad (5.20)$$

where  $\mathbf{n}$  is the normal direction to the wall boundary  $\partial\Omega$ . Given the normal direction  $\mathbf{n}$ , its end point  $B$  and considering the distance from  $A$  to  $B$  as  $||\mathbf{n}|| = \delta t$ , the values of density and temperature at  $B$  can be evaluated using a finite element interpolation. For example for the density, we can write,

$$\rho_B = \sum_{s=1}^9 \rho_s N_s, \quad (5.21)$$

where  $N_s$  are shape functions and  $\rho_s$  are the magnitude of density at nine collocation points (circles in Fig. 5.2). Once  $\rho_B$  is found, the first-order approximation for the normal derivative is assumed,

$$\frac{\partial \rho}{\partial \mathbf{n}}|_{wall} = \frac{\rho_B - \rho_A}{||\mathbf{n}||} = 0. \quad (5.22)$$

Therefore, the target value can be approximated as,

$$\rho_{tgt} = \rho_A = \rho_B. \quad (5.23)$$

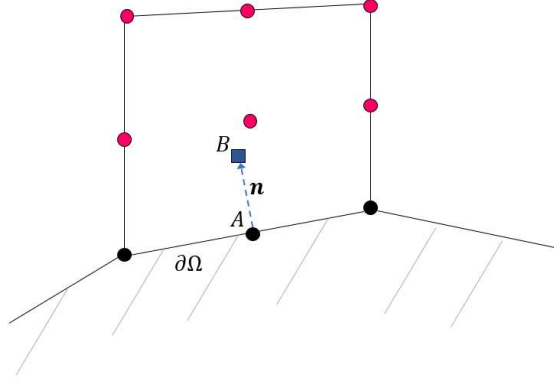


FIGURE 5.2: Schematic representation of the wall boundary condition implementation.

It is important to note that if missing populations belong to points which do not lie on the wall boundaries (red circles in Fig. 5.2), the local quantities of the previous time step are used as target values.

The evaluation of spatial gradients in non-equilibrium moments is performed using (5.10). It was demonstrated in [114] that the first-order accurate evaluation of spatial derivatives is sufficient.

### 5.2.2 Numerical results

In this section, the model presented above is validated numerically through simulation of four benchmark cases. All simulations are performed with  $\gamma = 1.4$ ,  $\text{Pr} = 0.71$ ,  $D2Q9$  lattice model and adiabatic wall assumption. The time step used in this study is  $\delta t = \delta x_{\min}/1.5$  which corresponds to the  $\text{CFL} = \frac{\max |v_i| \delta t}{\delta x_{\min}} = 0.66$ , where  $\delta x_{\min}$  is the minimum spacing between any two points of the computational mesh.

Element size( $\Delta x/L_x$ )	$L_\infty$ error	Order
0.1	0.033958	—
0.05	0.010144	1.75
0.025	0.002953	1.78
0.0125	0.000841	1.82

TABLE 5.2: Accuracy test for the propagation of density perturbation.

### 5.2.2.1 Accuracy test

The smooth density propagation [133] is solved in order to test the accuracy of the present model on unstructured mesh. The initial condition of the flow field is given by,

$$\rho = \rho_{ref} + 0.2\sin(2\pi x/L_x)\sin(2\pi y/L_y), \quad (5.24)$$

$$u = \text{Ma}\sqrt{\gamma T_{ref}}, \quad (5.25)$$

$$v = 0, \quad (5.26)$$

$$T = \rho_{ref}T_{ref}/\rho, \quad (5.27)$$

with the domain size  $L_x = L_y = 8000$ , reference density  $\rho_{ref} = 1$ , reference temperature  $T_{ref} = 0.2$  and  $\text{Ma} = 0.2$ . We compute the solution after two periods of propagation in order to evaluate the convergence order of the scheme using four different uniform grids and based on the  $L_\infty$  error of density. As shown in Table 5.2, the accuracy in space is slightly below second-order. This is consistent with previous results on semi-Lagrangian LB for incompressible flows as reported in Refs. [105, 129].

### 5.2.2.2 Sod's shock tube

The Sod's shock tube problem [101] is a classical Riemann problem to test the capability of the model when shock and expansion waves are present in the flow field. The initial flow field for this problem is given by

$$(\rho, u_x, u_y, P) = \begin{cases} (1.0, 0, 0, 0.2), & x/L_x \leq 0.5, \\ (0.125, 0, 0, 0.02), & x/L_x > 0.5, \end{cases} \quad (5.28)$$

where  $L_x = 20$  is the domain length. A uniform grid with  $400 \times 5$  elements is used with the viscosity  $\mu = 0.0001$ . Simulation results for the density

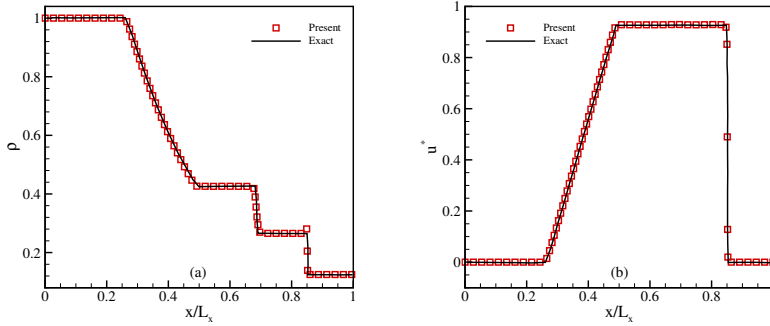


FIGURE 5.3: Density (left) and velocity (right) distributions for Sod shock tube problem at non-dimensional time  $t^* = 0.2$ . Symbols: present model; line: exact solution.

and reduced velocity  $u^* = u/\sqrt{T_l}$  ( $T_l$  is temperature on the left side of tube) at non-dimensional time  $t^* = t\sqrt{T_l}/L_x = 0.2$ , are shown in Fig. 5.3. It is observed that, apart from small oscillations, the results are in excellent agreement with the exact solutions.

### 5.2.2.3 Subsonic flow over NACA0012 airfoil

This test-case involves a subsonic flow over a NACA0012 airfoil at a Mach number  $Ma = u_\infty/\sqrt{\gamma T_\infty} = 0.5$ , incoming temperature  $T_\infty = 0.2$ , an angle of attack of  $\alpha = 0^\circ$ , and a Reynolds number of  $Re = \rho_\infty u_\infty c/\mu = 5000$  based on the chord length of the airfoil  $c$ . The simulation is performed on an unstructured quadrilateral mesh with 43235 elements as shown in Fig. 5.4 (Mesh-1), where a layer of orthogonal grid is used near the airfoil surface and anisotropic grid is used elsewhere. The minimum size of the elements near the airfoil surface  $\delta/c \approx 0.0015$ . In this case, the flow separation occurs near the trailing edge, which causes the formation of two small re circulation bubbles in the wake, as shown by the Mach number contours in Fig. 5.5. Pressure coefficient  $c_p = (P - P_\infty)/(0.5\rho_\infty u_\infty^2)$  and skin friction coefficient  $c_f = \tau_w/(0.5\rho_\infty u_\infty^2)$ , where  $\tau_w$  is the local wall shear stress, on the airfoil surface are compared in Fig. 5.6 with the discontinuous Galerkin (DG) solution of the compressible NS equations [134]. Moreover, the comparison of the drag coefficient with other numerical results is shown in Table 5.3. It can be seen that the present results are in good agreement with all reference data.

To further validate the solver, the numerical results computed at angle of attack  $\alpha = 2^\circ$  are also compared in Fig. 5.7 with the reference solution reported in [135]. Note that in this case the flow becomes unsteady in the wake.

Moreover, in order to investigate the effect of grid quality on the solution, we repeat the simulation with another mesh, but with irregular elements close to the airfoil surface, with the same element size near the wall ( $\delta/c \approx 0.0015$ ), as shown in Fig. 5.8 (Mesh-2). The results obtained are shown in Fig. 5.7 in comparison with the results of Mesh-1 and the reference solution [135]. It is observed that, the results are almost identical. We can therefore conclude that in this case, the mesh quality does not have significant effect on the results. However, the effect of grid quality needs to be further investigated in problems with higher Reynolds number, as it might be necessary to employ a high quality orthogonal grid near the surface in order to correctly capture the boundary layer.

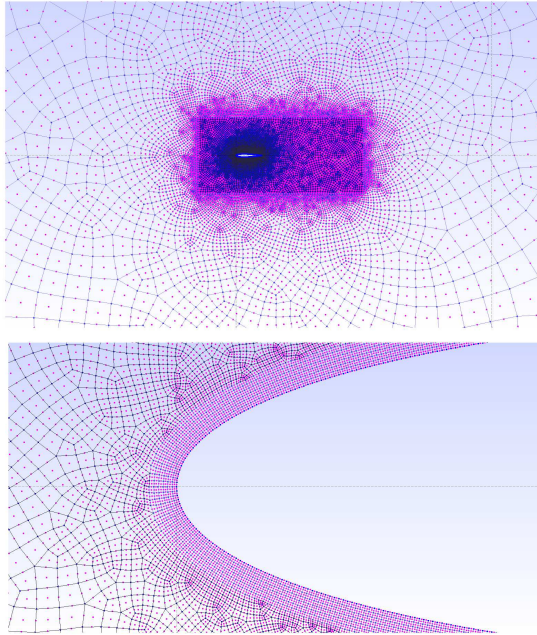


FIGURE 5.4: Second-order finite element mesh (Mesh-1) used for the simulation of subsonic flow over NACA0012 airfoil. Bottom is the zoom near leading edge of the airfoil.

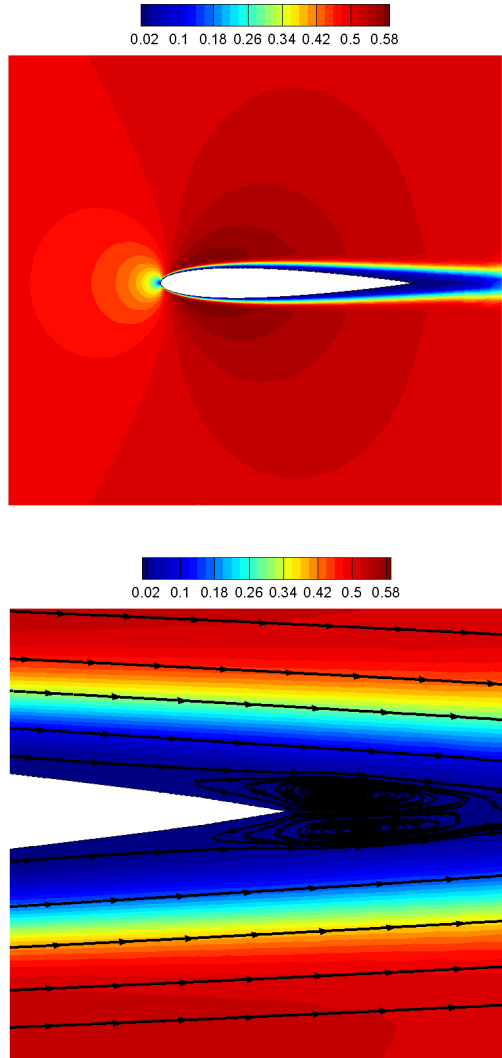


FIGURE 5.5: Mach contour for subsonic flow over NACA0012 airfoil at  $Ma = 0.5$ ,  $Re = 5000$  and  $\alpha = 0^\circ$ . Bottom figure shows streamlines near trailing edge.

Method	$c_d$
Direct DG [134]	0.05543
Reconstructed DG [136]	0.05534
Spectral difference [137]	0.05476
Present	0.05568

TABLE 5.3: Drag coefficient for subsonic flow over NACA0012 airfoil at  $Ma = 0.5$ ,  $Re = 5000$  and  $\alpha = 0^\circ$ .

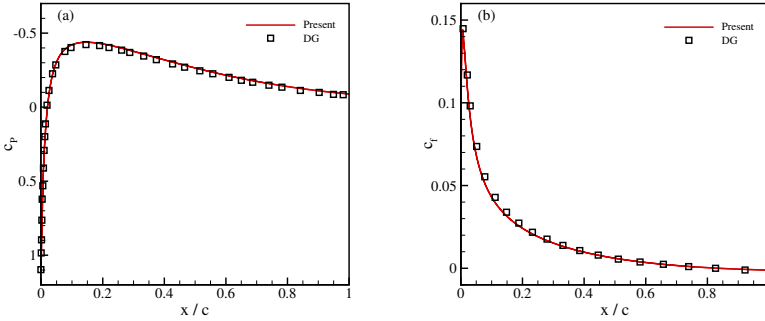


FIGURE 5.6: Distribution of (a) pressure coefficient and (b) skin friction coefficient, on the NACA0012 airfoil surface for subsonic flow at  $Ma = 0.5$ ,  $Re = 5000$  and  $\alpha = 0^\circ$ . Line: present model; symbols: DG solver [134].

#### 5.2.2.4 Unsteady supersonic flow over NACA0012 airfoil

In order to test the capability of the present model in capturing shock waves on unstructured mesh, the Mach number of the previous setup was increased to  $Ma = 1.5$  and the Reynolds number was set to  $Re = 10000$ . As flow is supersonic, shifted lattice with  $U_x = 0.3$  was used and unstructured mesh with 143123 quadrilateral elements and minimum element size of  $\delta/c = 0.0015$  was employed.

Figure 5.9 shows the temperature and Mach contours. It is observed that a bow shock is formed in front of the airfoil and oblique shocks appear from the trailing edge. Moreover, vortex shedding is started downstream, due to the shear layer developing from the trailing edge boundary layer of the airfoil. To quantify the results, in Fig. 5.10 the pressure coefficient upstream,

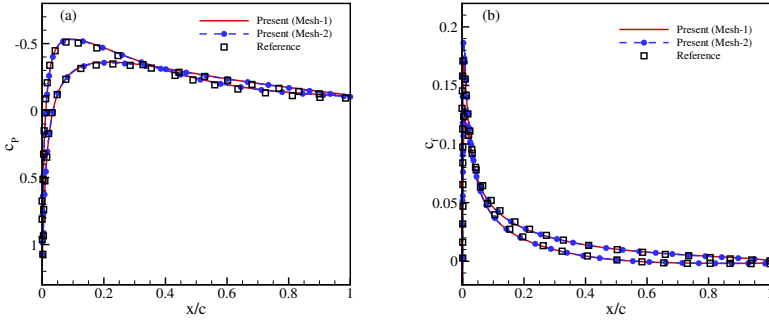


FIGURE 5.7: Distribution of (a) pressure coefficient and (b) skin friction coefficient, on the NACA0012 airfoil surface for subsonic flow at  $Ma = 0.5$ ,  $Re = 5000$  and  $\alpha = 2^\circ$ . Lines: present model; symbols: reference solution [135].

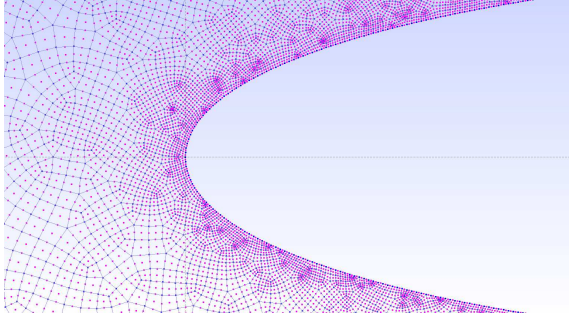


FIGURE 5.8: Mesh-2 used for the simulation of subsonic flow over NACA0012 airfoil.

downstream and on the airfoil surface is compared to the numerical solution reported in [138] and also with the solution of the entropic LBM (ELBM) with D2Q49 lattice model [110]. Good agreement is observed and the present method captures the pre/post shock values and the shock location with good accuracy.

#### 5.2.2.5 Shock-vortex interaction in Schardin's problem

Finally, the so called Schardin's problem [139, 140] is considered in which a planar shock wave impinges on a finite wedge is reflected and diffracted.



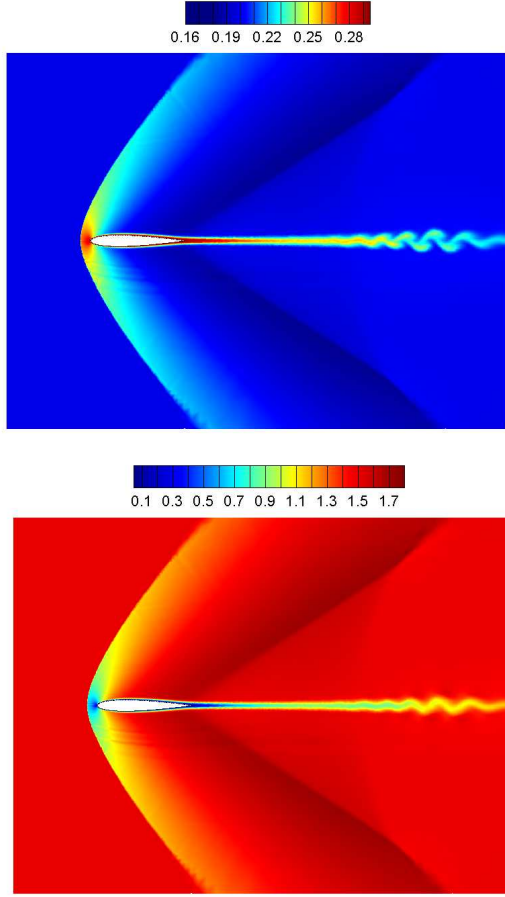


FIGURE 5.9: Temperature (top) and Mach number (bottom) contours for supersonic flow over NACA0012 airfoil at  $Ma = 1.5$ ,  $Re = 10000$ .

The impingement creates a complex shock-shock and shock-vortex interaction [140]. This test-case shows the ability of the scheme in handling complex geometries at high-speed flows. Here, a shock Mach number  $Ma_s = 1.34$  is considered and the Reynolds number based on wedge length  $L$  is set to  $Re = 2000$ . Further details on this setup can be found in [140]. Moreover, shifted lattice with  $U_x = 0.3$  is used.

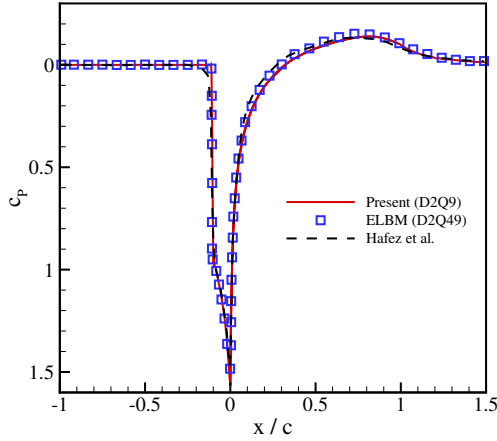


FIGURE 5.10: Pressure coefficient upstream, downstream and on the NACA0012 airfoil surface for supersonic flow at  $Ma = 1.5$ ,  $Re = 10000$ . Line: present model with  $D2Q9$  lattice; symbols: ELBM solution with  $D2Q49$  lattice; dashed line: results reported in [138].

Figure 5.11 shows the evolution of flow field by plotting the density distribution over time. It is observed that the traveling shock wave creates two vortices at the two corners and then interacts with its mirrored counterpart, and refracts. Moreover, the time evolution of the position of the triple points  $T_1$  and  $T_2$  (shown in Fig. 5.11), where the reflected and the travelling shocks meet, is compared in Fig. 5.12 with the experimental results [140] and numerical results of ELBM with  $D2Q49$  lattice model [79]. Once again, the results obtained are in good agreement with those solutions, which shows the accuracy of the present model.

### 5.3 ARBITRARY LAGRANGIAN EULERIAN APPROACH FOR MOVING GEOMETRIES

In recent years, there is a growing interest in studying both numerically [141] and experimentally [142], fluid flows in moving and deforming geometries pertinent to many physical phenomena and novel engineering applications. For example, in flapping flights of birds and insects, it is the motion of aerodynamic surfaces that produces thrust for forward motion

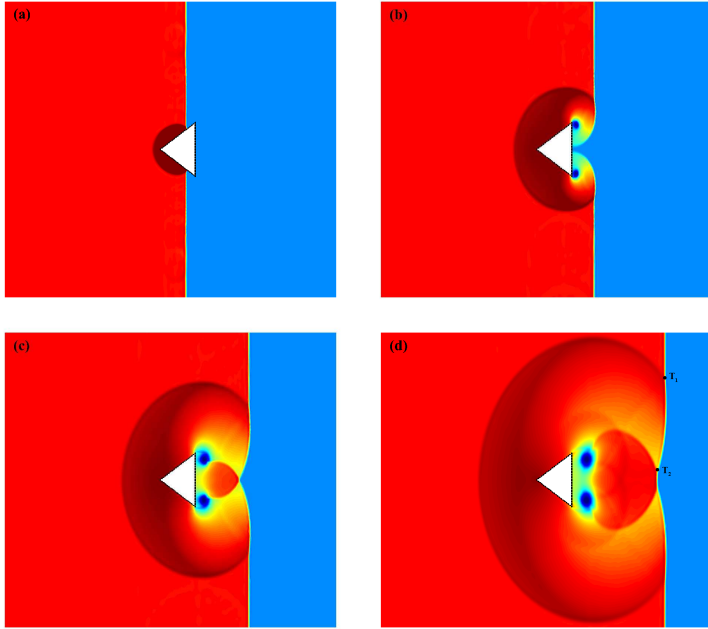


FIGURE 5.11: Evolution of the density for the Schardin's problem at shock Mach number  $Ma_s = 1.34$ .  $T_1$  and  $T_2$  are triple points.

and sustainable lift for airborne; or in marine animals such flapping motion generates propulsive and manoeuvring forces [143]. Understanding the underlying aerodynamics of these phenomena provides researchers with valuable insight into the origin of flight and its subsequent evolution in different species [144]. Moreover, these natural phenomena have been a rich source of inspiration in design of engineering devices such as robotic devices, micro-air vehicles or in novel turbines that extract energy from wind and tidal waves using flapping foil motion. The flapping foil turbine concept is promising in turbine technologies as it is expected to be more efficient than vertical- and horizontal-axis turbines [145] (for a review see Young, Lai & Platzer [143] and Xiao & Zhu [146]). Other applications of flows with moving geometries appear in fluid-solid interactions (FSI) and rotor-stator flows to name a few.

Presence of moving/deforming geometries in a flow adds another level of complexity to the computations, as one requires the numerical scheme not only to be able to handle moving domains, but also to maintain accuracy

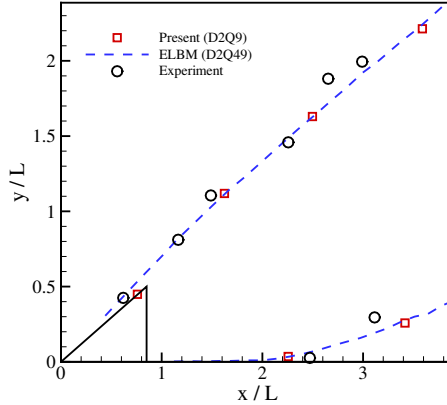


FIGURE 5.12: Comparison of the position of triple points  $T_1$  and  $T_2$  for the Schardin's problem. Squares: present model with  $D2Q9$  lattice; dashed Line: ELBM solution with  $D2Q49$  lattice [79]; circles: experiment [140].

and efficiency [147]. From a physical point of view, moving boundary problems usually involve vortex dominated unsteady flow with turbulence, separation and reattachment of the boundary layer. Numerically, capturing such a complex physics requires the numerical scheme to be accurate with small numerical dissipation.

For handling moving complex geometries, most of the existing LB realizations employ a fixed background regular Cartesian grid which cuts the immersed moving object. Imposing no-slip boundary condition on the moving object is then achieved either through adding a force term into the equations [148–150] or by replacing missing populations with some suitable approximation like non-equilibrium extrapolation [151] or Grad's approximation [114].

Another approach which has widely been used in the Navier-Stokes (NS) framework for simulating moving domain problems is based on the so-called arbitrary Lagrangian-Eulerian (ALE) method [152–157]. In this method, the governing equations in the physical domain which is moving in space and time, are mapped into a fixed computational domain and then the resulting transformed equations are solved numerically [153]. ALE method thus gives flexibility in handling moving domain problems as

the physical mesh can move with arbitrary velocity independent of the fluid velocity [156]. Another advantage of the ALE method is that it can handle moving/deforming domains with body-fitted mesh which is of crucial importance for high-Reynolds number flow simulations where small scale structures need to be resolved accurately. For problems involving rigid motion of objects and also problems with small deformation, it is possible to derive an analytical formula for the mapping function between physical and computational domains and that, in turn, greatly simplifies the computations. However, in problems with very large deformation, mapping function can become highly nontrivial and re-meshing might be required, which is computationally expensive and can easily make the simulation unfeasible.

While numerous studies have been done on the ALE-NS solvers, limited number of works can be found in the literature about applying ALE method in the context of LBM. Noteworthy is the model proposed by Meldi, Vergnault & Sagaut [158], which is based on the combination of ALE and over-set grid methods and was used for simulation of low-speed incompressible flow.

In this section, we apply the ALE method to the compressible LB model I, as it gives us a unified flow solver which covers subsonic to moderately supersonic regimes. To the best of our knowledge, LBM has not been investigated for the simulation of compressible flows with moving bodies. It should, however, be emphasized that the ALE formulation given below [159] is general and, in principle, can be applied to any lattice kinetic model, including incompressible [160, 161], thermal [97] or compressible models [79].

### 5.3.1 ALE formulation of LBM

Consider the discrete Boltzmann equation in a physical domain  $(\mathbf{x}, t)$ ,

$$\frac{\partial f_i}{\partial t} + \mathbf{c}_i \cdot \nabla_{\mathbf{x}} f_i = \Omega_i, \quad (5.29)$$

where  $f_i(\mathbf{x}, t)$  are populations of discrete velocities  $\mathbf{c}_i, i = 0, \dots, Q - 1$ , and  $\Omega_i$  is the collision operator. The goal here is to transform (5.29) from a physical domain  $(\mathbf{x}, t)$  to a fixed computational domain  $(\mathbf{X}, t_0)$ .

We assume that there exists a continuous time dependent mapping between physical and computational domains, denoted by  $G$ , such that  $\mathbf{x} = G(\mathbf{X}, t)$  [153]. The time derivative in (5.29) can then be re-written as,

$$\frac{\partial f_i}{\partial t} = \frac{df_i}{dt} - \mathbf{V}_G \cdot \nabla_{\mathbf{X}} f_i = \frac{\partial f_i}{\partial t} \Big|_{\mathbf{X}} - \mathbf{V}_G \cdot \nabla_{\mathbf{X}} f_i, \quad (5.30)$$

where the time derivative  $\frac{\partial f_i}{\partial t} \Big|_{\mathbf{X}}$  is at constant  $\mathbf{X}$ , spatial derivatives are taken with respect to  $\mathbf{X}$ , and  $\mathbf{V}_G$  denotes the mapping velocity as,

$$\mathbf{V}_G = \frac{\partial G}{\partial t} \Big|_{\mathbf{X}}. \quad (5.31)$$

Using a simple chain rule, the spatial terms in (5.29) can also be written as,

$$\nabla_{\mathbf{x}} f_i = \mathbf{g}^{-1} \nabla_{\mathbf{X}} f_i. \quad (5.32)$$

Here,  $\mathbf{g}^{-1}$  is the inverse of the Jacobian matrix of mapping, which for two-dimensional problems can be computed as,

$$\mathbf{g}^{-1} = \frac{1}{\det \mathbf{g}} \begin{bmatrix} y_Y & -y_X \\ -x_Y & x_X \end{bmatrix}, \quad (5.33)$$

where  $x_X, x_Y, y_X$  and  $y_Y$  are mapping metrics and

$$\det \mathbf{g} = x_X y_Y - y_X x_Y, \quad (5.34)$$

is the determinant of the Jacobian matrix. Substituting (5.30) and (5.32) into (5.29),

$$\frac{\partial f_i}{\partial t} \Big|_{\mathbf{X}} + \mathbf{c}_i \cdot \mathbf{g}^{-1} \nabla_{\mathbf{X}} f_i - \mathbf{V}_G \cdot \nabla_{\mathbf{X}} f_i = \Omega_i, \quad (5.35)$$

which can be further simplified as,

$$\frac{\partial f_i}{\partial t} \Big|_{\mathbf{X}} + \left( \mathbf{g}^{-1, \dagger} \mathbf{c}_i - \mathbf{V}_G \right) \cdot \nabla_{\mathbf{X}} f_i = \Omega_i, \quad (5.36)$$

where the superscript  $\dagger$  denotes the transpose of a matrix. By defining transformed discrete velocities  $\hat{\mathbf{c}}_i$  as,

$$\hat{\mathbf{c}}_i = \left( \mathbf{g}^{-1, \dagger} \mathbf{c}_i - \mathbf{V}_G \right), \quad (5.37)$$

the discrete Boltzmann equation in a fixed computational domain can be written in a simple form as,

$$\frac{\partial f_i}{\partial t} |_{\mathbf{X}} + \hat{\mathbf{c}}_i \cdot \nabla_{\mathbf{X}} f_i = \Omega_i. \quad (5.38)$$

As it can be seen, the only difference between (5.38) and (5.29) is in discrete velocities. We can therefore conclude that, the ALE method is applicable to any lattice kinetic model just by using the transformed discrete velocities as defined in (5.37).

Now, Eq. (5.38) can be discretized using conventional scheme used in the standard LB, i.e. through propagation and collision steps,

$$f_i(\mathbf{X}, t) - f_i(\mathbf{X} - \hat{\mathbf{c}}_i \delta t, t - \delta t) = \Omega_i. \quad (5.39)$$

It is evident from (5.37) that the discrete velocities  $\hat{\mathbf{c}}_i$  are not necessarily integer numbers anymore. Thus, unlike standard LB, exact propagation on space-filling lattice is not possible here and interpolation is required during the propagation step. We, therefore, use a second-order accurate finite-element interpolation introduced in the previous section. Thus, the propagation step can be written as,

$$f_i(\mathbf{X}, t) = f_i(\mathbf{X} - \hat{\mathbf{c}}_i \delta t, t - \delta t) = \sum_{s=1}^9 N_s(\boldsymbol{\xi}_{dp}) f_i(\boldsymbol{\xi}_s, t - \delta t), \quad (5.40)$$

where, as before,  $N_s(\boldsymbol{\xi}_{dp})$  is the values of the shape functions [130], written in the local coordinate system  $\boldsymbol{\xi} = (\zeta, \eta)$ ,  $(-1 \leq \zeta, \eta \leq 1)$ , at the departure point (red square in Fig. 5.1),  $f_i(\boldsymbol{\xi}_s, t - \delta t)$  are the values of populations at the collocation nodes (red circles in Fig. 5.1), and  $s = 9$  is the number of collocation points.

Semi-Lagrangian propagation on unstructured moving finite-element mesh requires two steps:

First, computing the local coordinates of the departure point  $\boldsymbol{\xi}_{dp}$  (see Fig. 5.1). Here, a bi-linear transformation is used to transform the computational cells into a reference unit cell. Thus, finding the local coordinates requires solving a non-linear system of equations resulting from

$$\mathbf{X}_{dp} = \sum_{s=1}^4 N_s(\boldsymbol{\xi}_{dp}) \mathbf{X}_s. \quad (5.41)$$

Unlike the stationary case where the location of departure point for each node remains fixed during the simulation, in the non-stationary simulation,

the departure point is moving, and therefore the non-linear equation (5.41) should be solved at each time step. Furthermore, in the second step, the values of the populations at the departure point are computed by means of the shape functions and the values of the populations at collocation nodes (red circles), i.e. by using (5.40).

After the propagation step is completed, the post-collision populations are computed in a standard way.

Final note is about computation of spatial derivatives in the ALE framework. Spatial derivatives should also be transformed from the physical to the computational domain. This can be done using a chain rule similar to (5.32). For a generic variable  $K$ , we can write,

$$\partial_x K = g^{-1} \partial_X K. \quad (5.42)$$

Here,  $g^{-1}$  is computed using (5.34), and

$$\partial_X K = J^{-1} \sum_{s=1}^9 K_s \partial_\xi N_s, \quad (5.43)$$

where  $J^{-1}$  is the inverse of the Jacobian matrix of transformation of a computational cell to a unit cell,

$$J^{-1} = \frac{1}{\det J} \begin{bmatrix} \partial_\eta Y & -\partial_\xi Y \\ -\partial_\eta X & \partial_\xi X \end{bmatrix}, \quad (5.44)$$

and

$$\det J = (\partial_\xi X)(\partial_\eta Y) - (\partial_\xi Y)(\partial_\eta X), \quad (5.45)$$

is the determinant of the Jacobian. The metrics of transformation  $\partial_\xi X$ ,  $\partial_\eta X$ ,  $\partial_\xi Y$ ,  $\partial_\eta Y$  are computed with the following formula,

$$\partial_\xi X = \sum_{s=1}^9 X_s \partial_\xi N_s. \quad (5.46)$$

### 5.3.2 Geometric conservation law

The problem of geometric conservation law (GCL) was first introduced in Thomas & Lombard [162], where it was shown that the numerical discretization errors associated with mapping metrics can induce errors



in the computed flow field which might lead to numerical instabilities [162]. This problem has been widely studied in the NS solvers and different strategies have been proposed for satisfying the GCL in that context [153, 163, 164].

In order to mathematically check the GCL, a uniform flow should satisfy (5.39). As the collision term vanishes with constant uniform flow, we just need to insert a constant solution  $f_i(\mathbf{X}, t) = f_i^0$  into (5.40),

$$f_i^0 = \sum_{s=1} N_s f_i^0. \quad (5.47)$$

Since the summation of shape functions is, by construction, equal to one ( $\sum_{s=1} N_s = 1$ ), the RHS of (5.47) is simplified as,

$$\sum_{s=1} N_s f_i^0 = f_i^0 \sum_{s=1} N_s = f_i^0, \quad (5.48)$$

and, therefore, the present model satisfies the GCL exactly.

### 5.3.3 Numerical results

In this section, the model presented above is tested numerically in a set of benchmark problems with a moving boundary. First, the GCL of the model is validated. After that, we investigate the flapping airfoil under pure plunging and pitching motions which is relevant in many physical applications including the flight of small fliers [165] or micro air vehicles. All simulations are performed with  $\gamma = 1.4$ ,  $\text{Pr} = 0.71$ , the D2Q9 lattice model and the adiabatic wall assumption.

#### 5.3.3.1 Free-stream preservation

The first test-case is to check the GCL of the model, i.e. to ensure the exact conservation of the free-stream condition under arbitrary movement of the mesh. We consider a uniform flow with  $\text{Ma} = u_\infty / \sqrt{\gamma T} = 0.2$  and  $T = 0.2$  in a square domain of size  $L = 8000$ . The mesh motion is defined through the following mapping function,

$$x(t) = X + 500 \sin(2\pi X/L) \sin(2\pi Y/L) \sin(2\pi t/t_0), \quad (5.49)$$

$$y(t) = Y + 500 \sin(2\pi X/L) \sin(2\pi Y/L) \sin(2\pi t/t_0), \quad (5.50)$$

with the reference time  $t_0 = 1.5L/u_\infty$ . Fig. 5.13 shows the mesh at two different non-dimensional times  $t^* = tu_\infty/L$ . We compute the solution until

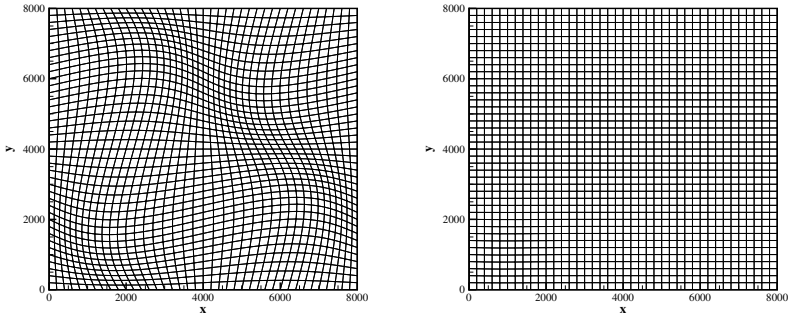


FIGURE 5.13: Motion of the mesh at non-dimensional time  $t^* = 0$  (top) and  $t^* = 1$  (bottom).

non-dimensional time  $t^* = 1$  using three different uniform grids, and the relative errors  $\epsilon = \sum |u - u_\infty| / \sum |u_\infty|$  of the velocity  $u$  are shown in Table 5.4. As it can be seen, the errors are found to be very small for different grids which demonstrate that the GCL is indeed satisfied in the present model.

Mesh( $\Delta x / L$ )	$\epsilon$
0.1	$1.117 \times 10^{-15}$
0.05	$4.028 \times 10^{-16}$
0.025	$3.872 \times 10^{-16}$

TABLE 5.4: Relative error  $\epsilon$  of the velocity  $u$  for the free-stream preservation problem.

### 5.3.3.2 Flow over NACA0012 airfoil in plunging motion

We consider a flow over an airfoil in a plunging motion to test the capability of the solver in handling complex vortex-dominated flows. It is known that the flow over plunging airfoil produces thrust over a wide range of oscillation frequencies [166], the phenomenon known as Knoller–Betz effect [167]. Another interesting phenomenon observed experimentally [167] is the formation of asymmetric deflected wake pattern at high Strouhal numbers, even in symmetrically plunging motions. Apart from the experiments [167–

169], several numerical studies [141, 166, 170–173] are also available which give insight into the physics behind the plunging airfoil and the mechanism of thrust generation.

Here, in order to take into account the effect of compressibility, the numerical setup is chosen identical to the numerical study by Liang *et al.* [170] based on the higher-order accurate spectral difference ALE solution of the compressible NS equations (SD-NS). A NACA0012 airfoil with chord length  $c = 200$  is placed in the center of a domain with the size  $[40c \times 40c]$ . The airfoil is undergoing a sinusoidal plunging motion prescribed as,

$$x(t) = X, \quad (5.51)$$

$$y(t) = Y - h \sin(\omega t), \quad (5.52)$$

where  $h$  and  $\omega$  are plunge motion amplitude and frequency, respectively. The Strouhal number is defined as,

$$Sr = h\omega/u_\infty, \quad (5.53)$$

and  $u_\infty$  is the free-stream velocity.

Two different scenarios are considered here: slow plunging and fast plunging motions. For both cases, the Reynolds number based on the free-stream velocity  $u_\infty$  is set to  $Re = \rho_\infty u_\infty c / \mu = 1850$ , the Mach number is  $Ma = u_\infty / \sqrt{\gamma T_\infty} = 0.2$  and the free-stream temperature is  $T_\infty = 0.3$ .

- *Slow plunging motion*

In the slow plunging motion, the plunge amplitude is  $h = 0.08c$  and the Strouhal number is  $Sr = 0.46$ . We first compute this case using two different meshes with minimum cell sizes of  $\delta \approx 0.7$  (Mesh-1) and  $\delta \approx 0.5$  (Mesh-2), in order to investigate grid independence. Part of the mesh is shown in Fig. 5.14, where orthogonal grid is used close to the wall to accurately resolve the boundary layer and anisotropic unstructured grid is used elsewhere. In order to correctly capture the vortical patterns in the wake area, a high resolution mesh with cell size of  $\delta \approx 10$  is used in the rectangular domain around the airfoil. Moreover, to minimize the computational cost, the mesh outside of the rectangular domain is highly coarse which makes the ratio between the largest and the smallest cell size to be of approximately  $\sim 1000$ .

The time evolution of the aerodynamic forces predicted by both grids are compared in Fig. 5.15. The lift coefficient is defined as  $c_L = F_L / (0.5\rho_\infty u_\infty^2 c)$ , where  $F_L$  is the total lift force acting on the airfoil and the drag coefficient is

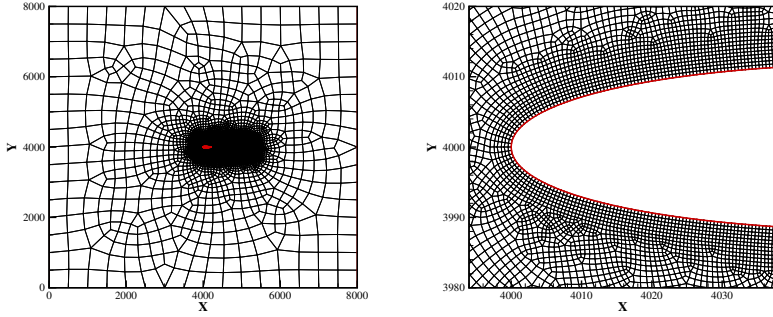


FIGURE 5.14: Mesh-2 used for the flow over plunging NACA0012 airfoil. Top: overall view; Bottom: zoom near leading edge of the airfoil.

given by  $c_D = F_D / (0.5\rho_\infty u_\infty^2 c)$ , where  $F_D$  denotes the total drag force. As it can be seen in Fig. 5.15, the lift coefficient varies symmetrically about zero mean, however, the drag coefficient oscillates around a negative average value which means that a small thrust is generated in this case. Moreover, the two grids give almost identical results which shows convergence to a grid independent solution. To validate the solver, the numerical results

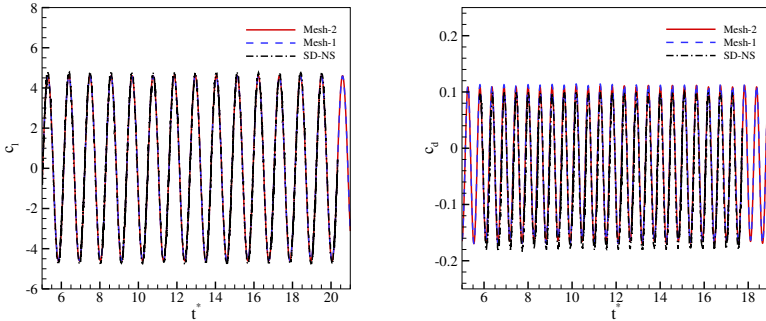


FIGURE 5.15: Time evolution of lift (top) and drag (bottom) coefficients for slow plunging motion of NACA0012 airfoil with  $h = 0.08c$ ,  $Sr = 0.46$ ,  $Ma = 0.2$  and  $Re = 1850$ .

of [170] over a few cycles are also shown in Fig. 5.15. It is observed that results are in good agreement.

Figure 5.16 shows the vorticity contours obtained by the present model in comparison with the experimental results reported by Jones, Dohring & Platzer [167]. Due to a relatively low Strouhal number in this case, the leading and trailing edges separation leads to in an almost symmetric flow pattern, which is very similar to what is observed in the experiment.

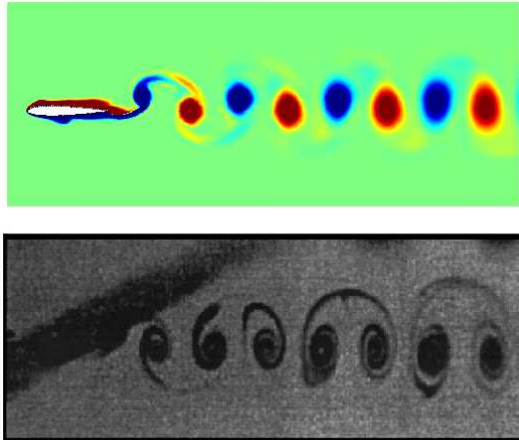


FIGURE 5.16: Vorticity computed by the present model (top) and the experimental results reported by Jones, Dohring & Platzer [167] (bottom), for slow plunging motion of NACA0012 airfoil with  $h = 0.08c$  and  $Sr = 0.46$ . Contour levels are bounded between  $-6 \leq \Omega c / u_\infty \leq 6$ .

- *Fast plunging motion*

Next we consider the fast plunging motion of the NACA0012 airfoil which corresponds to a motion with  $h = 0.12c$  and  $Sr = 1.5$ . The computation is performed using the mesh with the minimum cell size of  $\delta \approx 0.5$ .

Fig. 5.17 compares the vorticity contour obtained from the present model with the experimental results of [167]. It can be seen that in this case, the spatial symmetry of the wake vortex pattern is lost and a deflected vortex street is generated. The deflected vortex pattern is travelling upward because, according to (5.52), the first stroke is directed downward. Fig. 5.17 also shows that the present model is able to capture a dual-mode vortex street, in close resemblance with the experiment. The formation of dynamic stall vortex (DSV) [174] near the leading edge of the airfoil is also observed

in Fig. 5.17. Dynamic stall vortices convect towards the trailing edge of the airfoil.

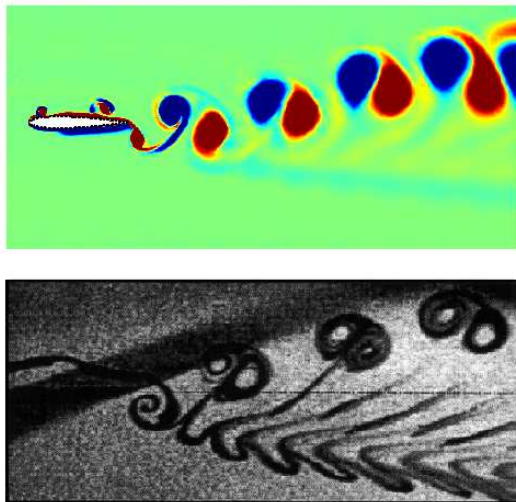


FIGURE 5.17: Vorticity computed by the present model (top) and the experimental results reported by Jones, Dohring & Platzer [167] (bottom), for fast plunging motion of NACA0012 airfoil with  $h = 0.12c$  and  $Sr = 1.5$ . Contour levels are bounded between  $-6 \leq \Omega c / u_\infty \leq 6$ .

In order to validate the results quantitatively, we compare the time history of the aerodynamic forces computed over several periods by the present model with that of the SD-NS solver [170]; excellent agreement is observed. As it is shown in Fig. 5.18, the maximum value of lift is larger than that in the slow plunging case and it oscillates symmetrically around a small mean value of about 1.43. The drag coefficient, on the other hand, is asymmetric and mainly negative which results in a net mean thrust.

### 5.3.3.3 Flow over NACA0012 airfoil in pitching motion

We now turn our attention to a flow over the pitching airfoil. The experimental works by Koochesfahani [175], Bohl & Koochesfahani [176] and Mackowski & Williamson [142] are among the most comprehensive studies of the flow over pitching airfoil in the incompressible regime; the authors studied the vortical patterns in the wake and measured the thrust coefficient as a function of the reduced frequency. Experiments show that the thrust

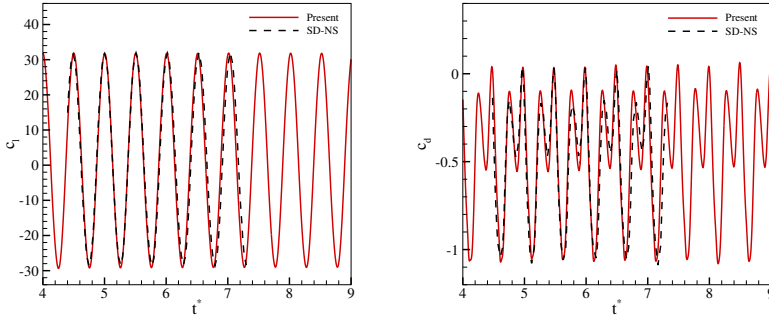


FIGURE 5.18: Time evolution of lift (top) and drag (bottom) coefficients for fast plunging motion of NACA0012 airfoil with  $h = 0.12c$ ,  $Sr = 1.5$ ,  $Ma = 0.2$  and  $Re = 1850$ .

coefficient increases monotonically with pitching frequency. However, the pure pitching motion is not, in general, an effective mechanism for producing thrust [142]. There are also several numerical studies in the literature focusing on different aspects of underlying fluid dynamics involved in the pitching airfoil [141, 170, 177, 178].

We consider the flow past NACA0012 airfoil in the pure pitching motion along its quarter chord axis ( $c/4$ ). The motion was prescribed by the following expression,

$$x(t) = (X - X_c) \cos(\theta) - (Y - Y_c) \sin(\theta), \quad (5.54)$$

$$y(t) = (X - X_c) \sin(\theta) + (Y - Y_c) \cos(\theta), \quad (5.55)$$

where  $(X_c, Y_c)$  is the center of rotation,  $\theta = A \sin(\omega t)$  is the pitching angle,  $A$  denotes the pitch amplitude and  $\omega$  is pitching frequency. The reduced frequency of pitching is defined as

$$k = \omega c / 2u_\infty. \quad (5.56)$$

In the first set of numerical experiments, the Mach number was considered to be  $Ma = 0.08$  in order to avoid significant effect of compressibility and to compare the results with the water tunnel experiment of [142, 176]. The simulation was performed at pitch amplitude of  $A = 2^\circ$ , reduced frequencies of  $k = 0$  (stationary),  $k = 6.68$  and  $k = 10$  and at Reynolds number  $Re = 12000$ . The high Reynolds number makes this test-case more challenging, although the flow is still considered to be laminar. The mesh

used for the computations has minimum cell size of  $\delta \approx 0.2$  in the near-wall region.

The vortical pattern obtained by the present model is shown in Fig. 5.19 in comparison with the experimental results of Koochesfahani [175], where a similar pattern can be observed. To quantitatively investigate the velocity field in the wake area, in Fig. 5.20, the mean streamwise velocity profile at a location of one chord downstream of the airfoil trailing edge is compared with the experimental result of Bohl & Koochesfahani [176] at the reduced frequency  $k = 5.2$ . The time averaging was performed after discarding an initial transient of  $t^* = 10$  and statistics collected until  $t^* = 40$ . It is apparent that the agreement is reasonable and the present model predicts a wake with velocity deficit similar to the experiment. However, the magnitude of the maximum velocity differs slightly from the experiment [176]. This difference could be due to compressibility or to three-dimensional effects, or insufficient resolution in the wake area.

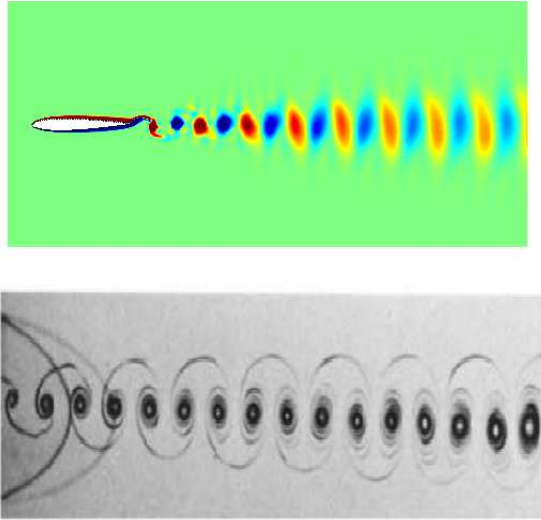


FIGURE 5.19: Vorticity computed by the present model (top) and the experimental results reported by Koochesfahani [175] (bottom) for pitching motion of NACA0012 airfoil with  $A = 2^\circ$  and  $k = 6.68$ . Contour levels are bounded between  $-11.5 \leq \Omega c / u_\infty \leq 11.5$ .

The time history of aerodynamic forces are presented in Fig. 5.21 and Fig. 5.22 for reduced frequencies of  $k = 6.68$  and  $k = 10$ , respectively.



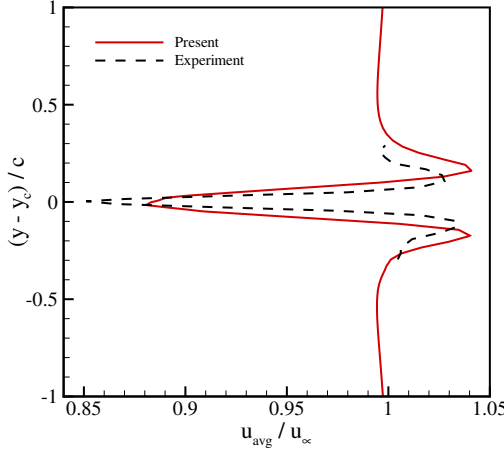


FIGURE 5.20: Mean streamwise velocity profile at a location one chord downstream of the airfoil trailing edge, for pitching motion of NACA0012 airfoil with  $A = 2^\circ$ ,  $k = 5.2$  and  $Re = 12600$ . Comparison is made with the experimental results of Bohl & Koochesfahani [176].

In both cases, the lift force acting on the airfoil is only due to pressure term ( $c_{l-p}$ ) while the contribution from the viscous force ( $c_{l-v}$ ) vanishes. Under this condition, the average lift is zero. However, the drag force has non-vanishing contributions from both the pressure ( $c_{d-p}$ ) and the viscous forces ( $c_{d-v}$ ). There is an average drag force acting on the airfoil in the case of  $k = 6.68$  and a small thrust in the case of  $k = 10$ .

To compare the results with the experimental measurements, we repeat the simulations at a slightly higher Reynolds number  $Re = 16600$  to match the experiment of Mackowski & Williamson [142]. Fig. 5.23 shows the comparison of the amplitude of lift and thrust forces acting on the airfoil at different reduced frequencies. It is observed that the simulation results show good agreement with experiment.

To investigate the effect of compressibility and in accordance with the numerical simulation of Young & S. Lai [177] based on the finite-difference discretization of compressible NSF equations, we repeated the simulations at higher Mach number  $Ma = 0.2$ . The time histories of lift and drag coefficients in this case at reduced frequency of  $k = 10$  are shown in Fig. 5.22; results for the low Mach number case are also shown for comparison. It can

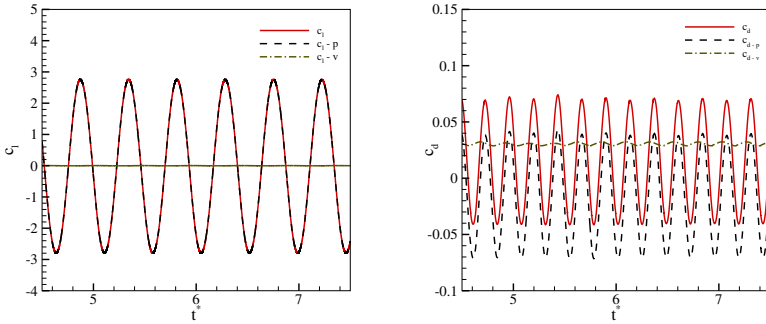


FIGURE 5.21: Time evolution of lift (top) and drag (bottom) coefficients for pitching motion of NACA0012 airfoil with  $A = 2^\circ$ ,  $k = 6.68$ ,  $Ma = 0.08$  and  $Re = 12000$ .

be seen that the compressibility effect significantly changes the distribution of pressure force while the viscous force remains almost the same.

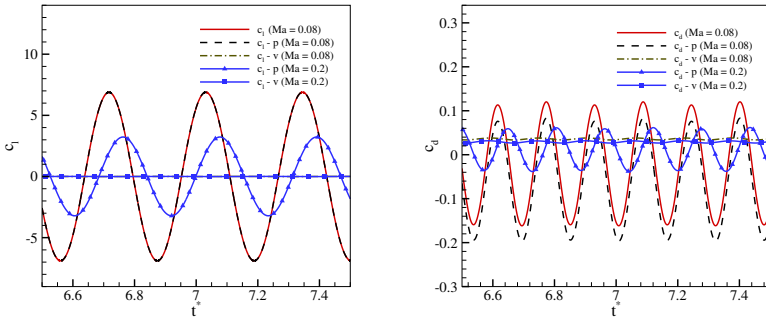


FIGURE 5.22: Time evolution of lift (top) and drag (bottom) coefficients for pitching motion of NACA0012 airfoil with  $A = 2^\circ$ ,  $k = 10$  and  $Re = 12000$ . Lines:  $Ma = 0.08$ ; lines with symbols:  $Ma = 0.2$ .

Finally, Fig. 5.24 shows the mean thrust coefficient of the present model at different frequencies in comparison with the experimental and numerical results. For computing the mean thrust coefficient, the result is time averaged after discarding the initial transients. In the low Mach number case, the thrust coefficient shows monotonic behaviour with frequency. However,

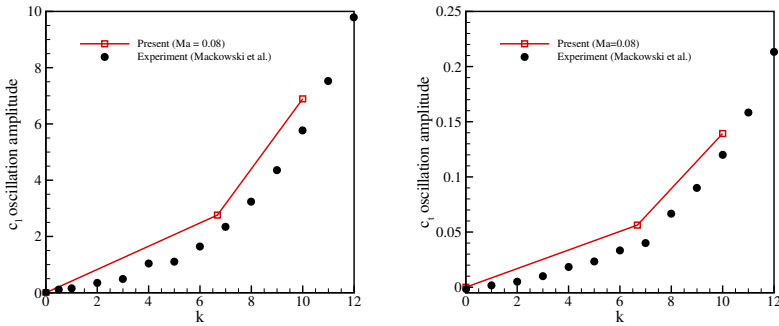


FIGURE 5.23: Amplitude of the lift (top) and thrust (bottom) forces acting on the NACA0012 airfoil under pitching motion with  $A = 2^\circ$  at different reduced frequencies and  $Re = 16600$ . Comparison is made with the experimental results of Mackowski and Williamson [142].

the case with  $Ma = 0.2$  shows a significantly different behaviour due to the effect of compressibility. We therefore conclude that pure pitching motion is even less efficient in producing thrust when the flow speed increases and the compressibility effects become important.

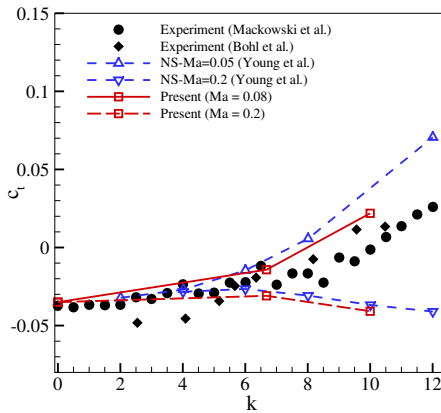


FIGURE 5.24: Comparison of the mean thrust coefficient with experimental and numerical results.

### 5.3.3.4 Transonic flow over NACA0012 airfoil in pitching motion

Finally, we address a challenging problem of a transonic flow over NACA0012 airfoil in pitching motion. Accurate computations of unsteady transonic flow is relevant in many applications such as wing flutter analysis or rotor-blade design [179].

We set the free-stream Mach number to  $Ma = u_\infty / \sqrt{\rho T_\infty} = 0.85$ , with  $T_\infty = 0.3$ , Reynolds number  $Re = 10000$ , pitching amplitude  $A = 2^\circ$  and reduced frequency of  $k = 3$ . Due to the high Mach number in this simulation, we need to employ the shifted lattices. In our application, we use the lattice with a shift in the free-stream direction as  $U = (U_x, U_y) = (0.3, 0)$ .

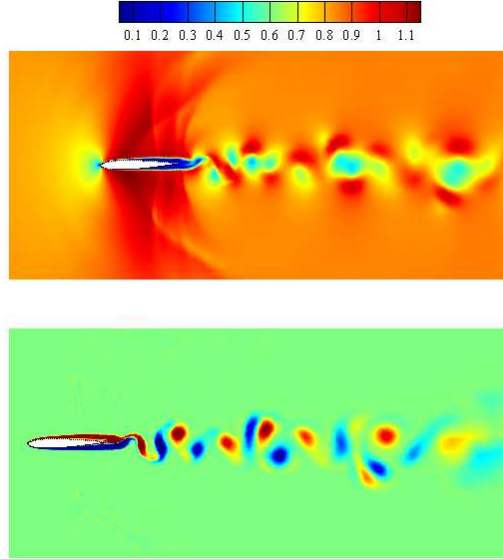


FIGURE 5.25: Mach number (top) and Vorticity (bottom) computed by the present model for pitching motion of NACA0012 airfoil with  $A = 2^\circ$ ,  $k = 3.0$  and  $Ma = 0.85$ . Vorticity contour levels are bounded between  $-11 \leq \Omega_c / u_\infty \leq 11$ .

Fig. 5.25 shows the Mach number distribution over the airfoil and vorticity contours computed by the present model. It is observed that in this case, a complex flow field is formed with multiple shock waves interacting with

the boundary and shear layers. Downstream of the leading edge, the flow accelerates causing a formation of weak oblique shock when it reaches the boundary layer. Weak shock waves in the form of lambda-shocks appear further downstream as well. These shock waves interact with the boundary layer, causing the flow separation, and will also be influenced by the vortex shedding downstream of the airfoil [180]. The vortex shedding associated with the shear layer instabilities combines with the vortex shedding due to the airfoil movement, resulting in a complex vortex pattern in the wake region.

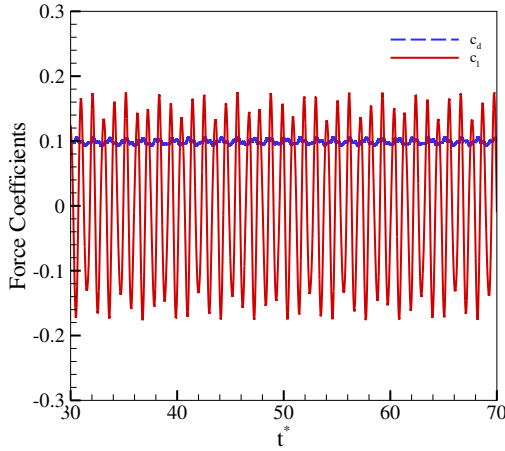


FIGURE 5.26: Time evolution of lift and drag coefficients for pitching motion of NACA0012 airfoil with  $A = 2^\circ$ ,  $k = 3$ ,  $Ma = 0.85$  and  $Re = 10000$ .

Time histories of lift and drag coefficients are presented in Fig. 5.26. Similar to the previous pitching cases with smaller Mach number, the average lift force is close to zero. However, there is a mean drag force of  $c_d \approx 0.0986$  acting on the airfoil, which is significantly larger than its counterpart in the low Mach number case. This confirms the previous observation about the effect of compressibility on increasing the drag force.

## 5.4 CONCLUSION

We presented an extension of the compressible lattice Boltzmann model on standard lattices, for the simulation of compressible flows over complex

geometries on unstructured mesh. The extension was based on the semi-Lagrangian propagation on unstructured finite element mesh and Grad's approximation for replacing missing populations near the wall boundaries. The model was validated by simulating four benchmark test-cases including: Sod's shock tube, subsonic/supersonic flow over NACA0012 airfoil and shock-vortex interaction in Schardin's problem. It was shown that the results obtained with the present model on standard lattice are in good agreement with the available numerical and experimental results in the literature. Moreover, it was demonstrated that the present model with shifted lattice can successfully capture moderately supersonic shock waves on fully anisotropic meshes without using any artificial dissipation or limiters.

We then proposed a solution methodology for the simulation of compressible flows on unstructured moving meshes based on the arbitrary Lagrangian-Eulerian (ALE) technique. To that end, the kinetic equations were mapped from a physical moving domain to a fixed computational domain. The analysis of the model was conducted through simulation of compressible flow over NACA0012 airfoil undergoing plunging and pitching motions at different Mach numbers. It was demonstrated that the model is able to properly predict the relevant features of the complex flow over flapping airfoil. In particular, the vortical patterns of the wake, the time histories of lift and drag coefficients and their mean values agreed well with the experimental and numerical results in the literature. Both slow and fast plunging motion of airfoil produce a net mean thrust with very small average lift. Pitching motion, however, is not as effective as plunge motion and a thrust is generated at higher frequencies, and only when the compressibility effects are small. It was also observed that the impact of compressibility is mainly on the distribution of pressure force rather than the viscous force. Finally, in order to show the model's performance in simulating high-speed flows, transonic flow over pitching airfoil was considered, where complex flow pattern involving multiple shock waves interacting with the boundary and shear layers were observed in the flow field.

## COMPRESSIBLE TURBULENT SIMULATIONS

---

### 6.1 INTRODUCTION

Compressible turbulence concerns with turbulent flows where density and temperature fluctuations and also a dilatational velocity component cannot be ignored. Typical examples of compressible turbulence can be found in aerodynamic applications. The presence of shock waves in such flows also imposes severe challenges for an accurate numerical simulation. Shock waves are sharp discontinuities of the flow properties across a thin region with the thickness of the order of mean free path. Since in practical simulations, it is impossible to use a grid size fine enough to resolve the physical shock structure defined by the molecular viscosity, most numerical schemes rely on some numerical dissipation to stabilize the simulation and capture the shock over a few grid points [2, 3]. The additional numerical dissipation of shock capturing schemes, however, is problematic in smooth turbulent regions of the flow, where a non-dissipative scheme is required to capture the complex physics accurately. Therefore, in recent years, much effort has been devoted to developing numerical schemes capable of treating shocks and turbulence, simultaneously. This has resulted in various improvements of the Weighted essentially non-oscillatory (WENO) scheme [181–184], artificial diffusivity approaches [185] and hybrid schemes [186], to name a few.

A proper numerical methodology to deal with compressible turbulent flows, thus, requires a low-dissipative scheme for the accurate representation of turbulent field and, at the same time, enough dissipation to reduce nonphysical oscillations near shocks. As such, the extended lattice Boltzmann model II, introduced in Chapter 3 and extended to supersonic flow in Chapter 4, is a suitable candidate, as the low-dissipative nature of the exact on-lattice propagation is coupled with the dissipation of correction term computed with the first-order upwind scheme.

In this chapter, we investigate the accuracy and performance of that model for compressible turbulent flows by considering the decaying of a compressible homogeneous isotropic turbulence in a periodic box at different turbulent Mach numbers and Reynolds numbers. This problem has been studied extensively [115, 187–193] and is a challenging test-case, as

it contains both compressibility effects and shocks, as well as turbulent structures in the flow field [189]. It will be demonstrated that computing the correction terms with the upwind scheme provides enough numerical dissipation to avoid the Gibbs oscillations, and to effectively capture the shock waves without degrading the accuracy of the scheme and overwhelming the physical dissipation in smooth regions.

## 6.2 DECAYING OF COMPRESSIBLE HOMOGENEOUS ISOTROPIC TURBULENCE

To demonstrate that the present compressible model is a reliable method for the simulation of complex flows involving both turbulence and shocks, decaying compressible homogeneous isotropic turbulence in a periodic box is considered.

The initial condition in a cubic domain with the side  $L$  is set to be unit density and constant temperature along with a divergence-free velocity field which follows the specified energy spectrum,

$$\mathcal{E}(\kappa) = A\kappa^4 \exp\left(-2(\kappa/\kappa_0)^2\right), \quad (6.1)$$

where  $\kappa$  is the wave number,  $\kappa_0$  is the wave number at which the spectrum peaks and the amplitude  $A$  controls the initial kinetic energy [115]. The method of kinematic simulation [194] is used to generate the velocity field.

Control parameters for this problem are the turbulent Mach number,

$$\text{Ma}_t = \frac{\sqrt{\langle \mathbf{u} \cdot \mathbf{u} \rangle}}{\langle c_s \rangle}, \quad (6.2)$$

and the Reynolds number based on the Taylor microscale,

$$\text{Re}_\lambda = \frac{\langle \rho \rangle u_{rms} \lambda}{\mu_0}, \quad (6.3)$$

where  $u_{rms} = \sqrt{\langle \mathbf{u} \cdot \mathbf{u} \rangle/3}$  is the root mean square (rms) of the velocity and notation  $\langle \dots \rangle$  stands for the volume averaging over the entire computational domain, while  $\lambda$  is the Taylor microscale,

$$\lambda = \frac{\langle u_x^2 \rangle}{\langle (\partial_x u_x)^2 \rangle}. \quad (6.4)$$

The dynamic viscosity is following a power law dependence on temperature,

$$\mu = \mu_0 \left( \frac{T}{T_0} \right)^{0.76}, \quad (6.5)$$



with  $T_0$  being the initial temperature. The Prandtl number for all the simulations is  $\text{Pr} = 0.7$  in accordance with the DNS [115].

### 6.2.0.1 Low turbulent Mach number

The simulation is first performed at a relatively low turbulent Mach number  $\text{Ma}_t = 0.3$  with  $\text{Re}_\lambda = 72$ ,  $\kappa_0 = 8(2\pi/L)$  and initial temperature  $T_0 = 0.15$ . Fig. 6.1 illustrates the instantaneous iso-surface of the velocity divergence

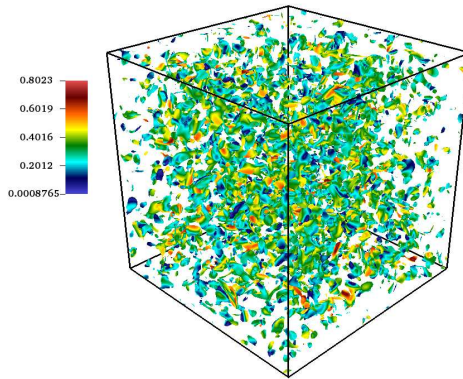


FIGURE 6.1: Iso-surface of velocity divergence  $\nabla \cdot \mathbf{u} = 0.005$ , colored by local Mach number for compressible decaying turbulence at  $\text{Ma}_t = 0.3$ ,  $\text{Re}_\lambda = 72$  and  $t^* = 0.4$ .

$\nabla \cdot \mathbf{u}$  colored with the local Mach number at the non-dimensional time  $t^* = t/\tau = 0.4$ , where  $\tau = L_I/u_{\text{rms},0}$  is the large eddy turnover time defined based on the initial rms of the velocity and the integral length scale,

$$L_I = \frac{3\pi \int_0^\infty [E(\kappa)/\kappa] d\kappa}{4 \int_0^\infty E(\kappa) d\kappa} = \frac{\sqrt{2\pi}}{\kappa_0}. \quad (6.6)$$

It is observed that in this case, the flow is in a moderately compressible to a high-subsonic regime, with the maximum local Mach number  $\text{Ma}_{\text{max}} \sim 0.8$ .

In order to quantify the validity of the model, a grid convergence study is performed by using three domain sizes,  $64^3$ ,  $128^3$  and  $256^3$ . The decay of the turbulent Mach number and of the turbulent kinetic energy  $K = 1/2 \langle \rho u^2 \rangle$  are shown in Fig. 6.2 and Fig. 6.3, where the convergence to the DNS results [115] can be observed.

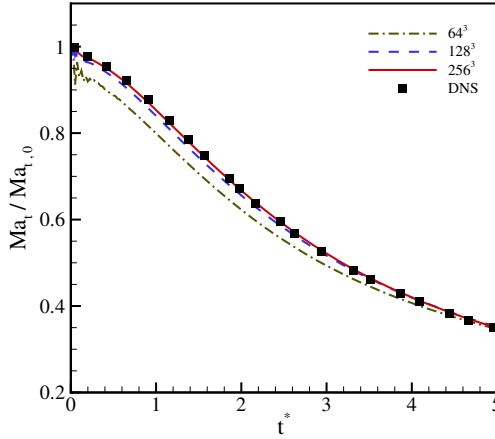


FIGURE 6.2: Decay of the turbulent Mach number for compressible decaying turbulence at  $Ma_t = 0.3$  and  $Re_\lambda = 72$ . Lines: present model; symbol: DNS [115].

To assess the effect of compressibility, time evolution of the rms of dilatation,

$$\theta_{rms} = \sqrt{\langle (\nabla \cdot \mathbf{u})^2 \rangle}, \quad (6.7)$$

is compared in Fig. 6.4 with the DNS, where dilatation is normalized with the initial rms of vorticity,  $\omega_{rms,0} = \sqrt{\langle |\boldsymbol{\omega}_0|^2 \rangle}$ , and  $\boldsymbol{\omega} = \nabla \times \mathbf{u}$ . Strong compressibility effects can be seen at the initial stage, where dilatation rapidly increases from its initial value  $\theta_{rms,0} = 0$ , followed by a monotonic decay. Furthermore, the rms of the density  $\rho_{rms} = \sqrt{\langle \rho^2 \rangle - \langle \rho \rangle^2}$  normalized by  $Ma_{t,0}^2$  is shown in Fig. 6.5. Also here the agreement with the DNS is quite satisfactory with  $256^3$  grid points.

The enstrophy defined as,

$$\Omega = \frac{1}{2} \langle \omega^2 \rangle, \quad (6.8)$$

is a sensitive variable to analyze the performance of a numerical scheme for turbulent flows, as it is closely related to small-scale turbulence motions [195, 196]. The temporal evolution of the enstrophy normalized with its initial value is compared in Fig. 6.6 with the DNS results of the spectral

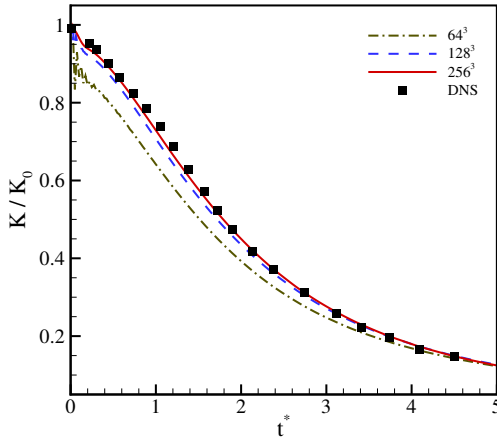


FIGURE 6.3: Decay of the turbulent kinetic energy for compressible decaying turbulence at  $Ma_f = 0.3$  and  $Re_\lambda = 72$ . Lines: present model; symbol: DNS [115].

method reported in Fang *et al.* [195]. It can be seen that in all cases the enstrophy increases in the beginning due to vortex stretching, which generates small-scale turbulence structures. This makes the viscous dissipation stronger, which leads to a decrease of enstrophy [196]. Furthermore, coarse simulations result in under-prediction of peak value and also fast decay rate, due to strong suppression of small-scale fluctuations. Here, contrary to the previous cases,  $256^3$  grid size is not enough to accurately capture the statistics. By increasing the resolution to  $512^3$ , the peak value and decay rate of enstrophy can be captured with good accuracy. This further confirms the accuracy of the present model in capturing the physics of compressible turbulence.

Moreover, the convergence order of the model is evaluated based on the  $L_\infty$  error of enstrophy with respect to the DNS results. As shown in Fig. 6.7, the overall accuracy in space is slightly below second-order.

#### 6.2.0.2 Effect of deviation discretization on the accuracy

As pointed out earlier, first-order upwind discretization of the deviation term is necessary for preventing the Gibbs phenomenon and maintaining the stability of the model in supersonic regime. Here, we investigate the

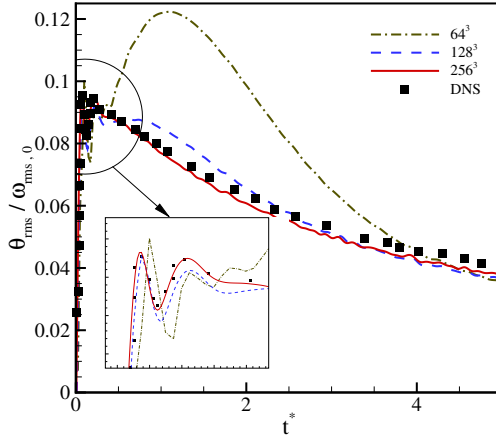


FIGURE 6.4: Time history of root mean square of dilatation for compressible decaying turbulence at  $Ma_t = 0.3$  and  $Re_\lambda = 72$ . Lines: present model; symbol: DNS [115].

effect of the discretization scheme on the accuracy in subsonic turbulent regime, by comparing the results to the case with second-order central evaluation of derivatives of deviation term.

It can be seen from Fig. 6.8 that, the time history of enstrophy is almost insensitive to the evaluation of deviation term. All other turbulence statistics showed similar behaviour, but are not presented here for the sake of brevity. This indicates that the use of first-order scheme does not degrade the formal accuracy of the solver (shown in Fig. 6.7), although it provides sufficient dissipation for stabilizing the solver and capturing the shock.

### 6.2.0.3 High turbulent Mach number

We now move on to a higher turbulent Mach number. It is well known that at sufficient high turbulent Mach numbers, random shock waves commonly known as eddy-shocklets appear in the flow [115, 187, 189], due to compressibility and turbulent motions. This scenario can, therefore, be considered as a rigorous test case for the validity of the present model.

We increase the turbulent Mach number to  $Ma_t = 0.5$  and perform the simulation with  $256^3$  and  $512^3$  grid points and the same Reynolds number  $Re_\lambda = 72$ . The iso-surface of the velocity divergence colored by local Mach

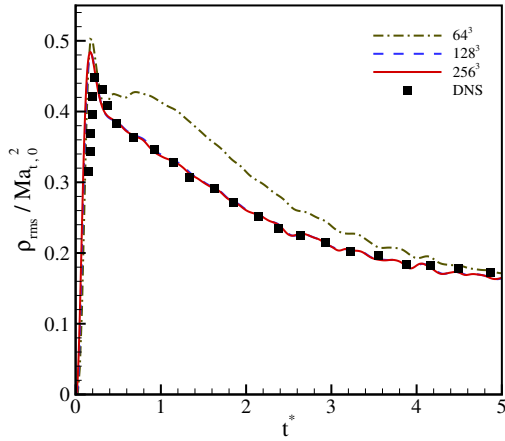


FIGURE 6.5: Time history of root mean square of density for compressible decaying turbulence at  $\text{Ma}_t = 0.3$  and  $\text{Re}_\lambda = 72$ . Lines: present model; symbol: DNS [115].

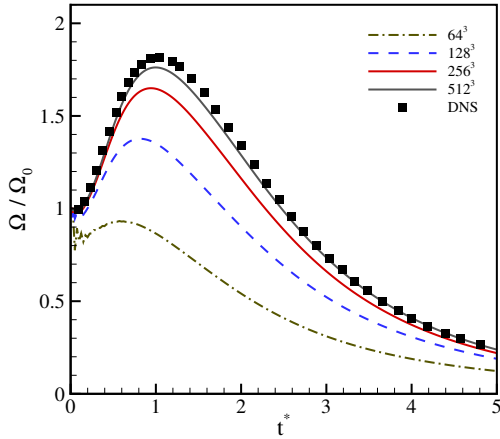


FIGURE 6.6: Time history of enstrophy for compressible decaying turbulence at  $\text{Ma}_t = 0.3$  and  $\text{Re}_\lambda = 72$ . Lines: present model; symbol: DNS [195].

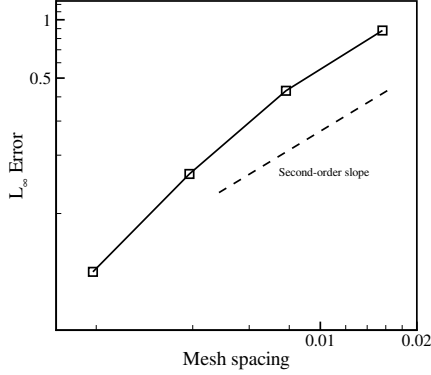


FIGURE 6.7: Convergence rate of enstrophy for grid resolutions  $64^3$  to  $512^3$ . Symbols:  $L_\infty$  error of enstrophy with respect to the DNS results; dashed line: second-order slope.

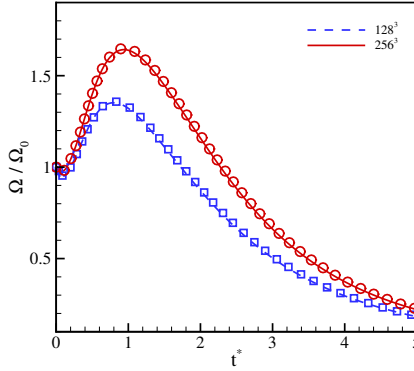


FIGURE 6.8: Effect of deviation discretization on the enstrophy evolution for compressible decaying turbulence at  $Ma_t = 0.3$  and  $Re_\lambda = 72$ . Lines: present model with first-order upwind discretization of deviation term; symbols: present model with second-order central difference discretization of deviation term.

number is shown in Fig. 6.9, which confirms the presence of local supersonic regions during the decay. Moreover, to show that the model can accurately

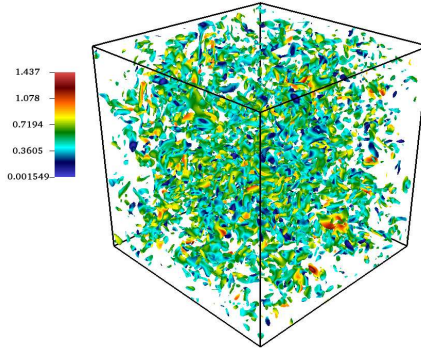


FIGURE 6.9: Iso-surface of velocity divergence  $\nabla \cdot \mathbf{u} = 0.015$ , colored by local Mach number for compressible decaying turbulence at  $\text{Ma}_t = 0.5$ ,  $\text{Re}_\lambda = 72$  and  $t^* = 0.4$ .

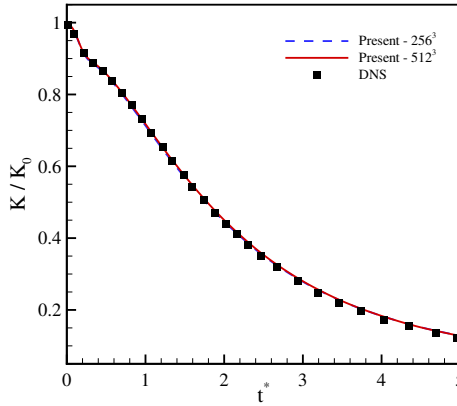


FIGURE 6.10: Decay of the turbulent kinetic energy for compressible decaying turbulence at  $\text{Ma}_t = 0.5$  and  $\text{Re}_\lambda = 72$ . Lines: present model; symbol: DNS [115].

predict turbulent statistics in the presence of shocks, time evolution of the turbulent kinetic energy, rms of density and Taylor microscale Reynolds number are plotted in Figs. 6.10, 6.11 and 6.12, respectively. Here also the results agree well with the reference DNS results.

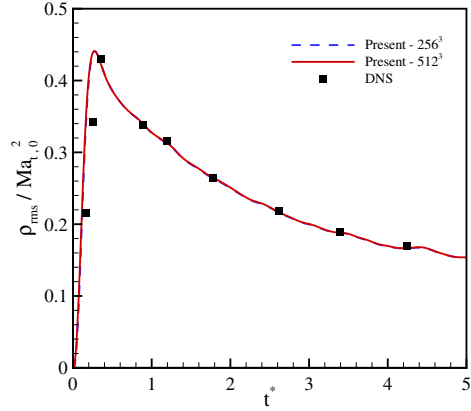


FIGURE 6.11: Time history of root mean square of density for compressible decaying turbulence at  $Ma_t = 0.5$  and  $Re_\lambda = 72$ . Lines: present model; symbol: DNS [115].

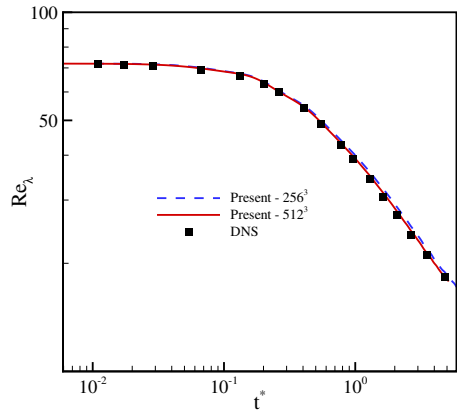


FIGURE 6.12: Time history of Taylor microscale Reynolds number for compressible decaying turbulence at  $Ma_t = 0.5$  and  $Re_\lambda = 72$ . Lines: present model; symbol: DNS [115].

As a final validation case, we investigate the performance of the model at a relatively high Reynolds number of  $Re_\lambda = 175$ , while keeping the



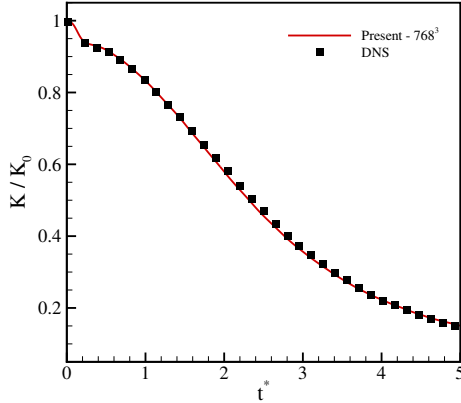


FIGURE 6.13: Decay of the turbulent kinetic energy for compressible decaying turbulence at  $Ma_t = 0.488$  and  $Re_\lambda = 175$ . Line: present model; symbol: DNS [115].

turbulent Mach number high enough  $Ma_t = 0.488$ . The initial spectrum peaks at  $\kappa_0 = 4(2\pi/L)$  in this case.

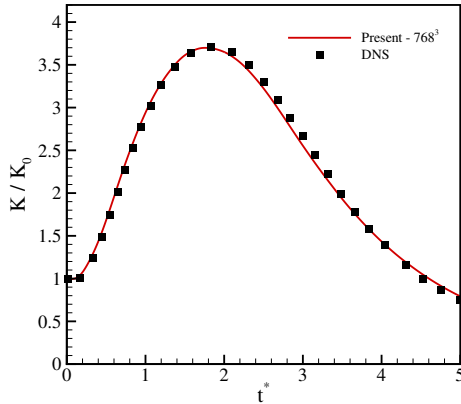


FIGURE 6.14: Time history of the dissipation rate for compressible decaying turbulence at  $Ma_t = 0.488$  and  $Re_\lambda = 175$ . Line: present model; symbol: DNS [115].

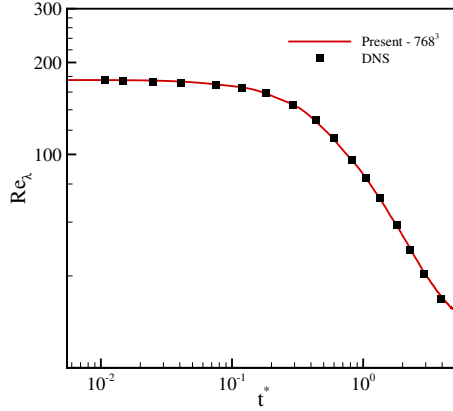


FIGURE 6.15: Time history of Taylor microscale Reynolds number for compressible decaying turbulence at  $Ma_t = 0.488$  and  $Re_\lambda = 175$ . Line: present model; symbol: DNS [115].

History of turbulent kinetic energy, solenoidal dissipation rate  $\epsilon = \langle \mu \omega^2 \rangle$  and Taylor microscale Reynolds number (6.3) are plotted in Figs. 6.13, 6.14 and 6.15, using  $768^3$  grid points. The results agree well with the reference DNS solution [115].

The energy spectrum at various times is shown in Fig. 6.16. It is observed that initially, large scales contain most of the energy and as time evolves the energy is transferred to small scales. Moreover, since the Reynolds number is high enough, the spectrum shows the inertial range with slope of  $\kappa^{-5/3}$  which further confirms the accuracy of the results and shows the ability of the model in capturing broadband turbulent motions in the presence of shocks.

### 6.3 CONCLUSION

It was demonstrated that the fully on-lattice extended model II with the single relaxation time LBGK collision term (introduced in Chapter 3) is able to properly predict the relevant features of the compressible turbulent flows. In particular, the simulation of compressible decaying turbulence demonstrated that the model can accurately capture compressibility effects, turbulence fluctuations and shocks. It was shown that the model performs well even at high turbulent Mach number, where eddy-shocklets exist in

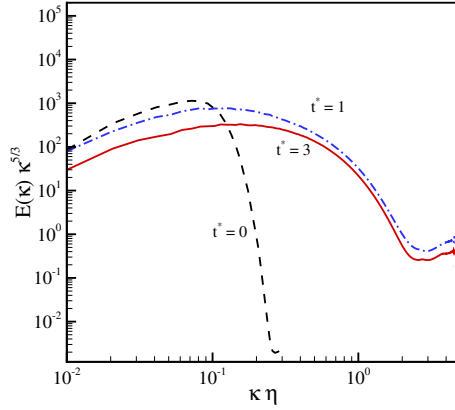


FIGURE 6.16: Energy spectrum at various times ( $t^* = 0, 1$  and  $3$ ) for compressible decaying turbulence at  $\text{Ma}_t = 0.488$  and  $\text{Re} = 175$ . Dashed line is the initial spectrum ( $t^* = 0$ ). Here,  $\eta$  is the Kolmogorov length scale.

the flow field and interact with turbulence. The results of the model were found to be in good agreement with DNS results.



## KINETIC THEORY IN A CO-MOVING REFERENCE FRAME: A PROMISING APPROACH

---

### 7.1 INTRODUCTION

Recently, a new representation of the kinetic theory named particles-on-demand (PonD) method [126] has been proposed which provides promising results in improving the inherent limitations of the LB models in terms of flow speed and temperature range. While the classical LB models work with populations in a fixed reference frame, in PonD the populations are formulated in a way to be in the optimal reference frame [126, 197], so that the equilibrium seen by the populations do not depend on the flow velocity and temperature [126]. This feature makes PonD a suitable candidate for the simulation of high-speed nonequilibrium flows which were impossible before with the LBM, such as the shock structure problem. PonD can also be considered as an alternative to hybrid solvers [198] for multi-scale flows, where the flow experiences a broad range of Knudsen numbers, from rarefied to continuum regimes.

In this chapter, we briefly present a two-population realization of the PonD with adjustable Prandtl number and adiabatic exponent for the simulation of classical shock structure problem.

### 7.2 KINETIC THEORY IN A CO-MOVING REFERENCE FRAME

We begin with a brief review. In PonD, the discrete speeds  $c_i$  are interpreted as peculiar velocities relative to a reference frame velocity  $\mathbf{u}_{\text{ref}}$  and temperature  $T_{\text{ref}}$ . Therefore, the discrete velocities are generally defined as [126],

$$\mathbf{v}_i = \sqrt{\frac{T_{\text{ref}}}{T_L}} \mathbf{c}_i + \mathbf{u}_{\text{ref}}, \quad (7.1)$$

where  $T_L$  is the constant lattice reference temperature specific for any set of discrete speeds  $\mathcal{C} = \{\mathbf{c}_i, i = 0, \dots, Q-1\}$  [70] and  $Q$  is the number of discrete speeds. By specifying the frame velocity and temperature in (7.1), one can set the reference frame  $\lambda(\mathbf{x}, t) = \{\mathbf{u}_{\text{ref}}, T_{\text{ref}}\}$  for the discrete

velocities. For example, The standard lattice Boltzmann with the discrete velocities  $c_i$ , is recovered by setting the reference frame at rest,  $\mathbf{u}_{ref} = 0$  and choosing the fixed temperature  $T_{ref} = T_L$ , i.e.  $\lambda(\mathbf{x}, t) = \{0, T_L\}$ .

With the discrete velocities (7.1), the two-population kinetic equations which enable variable Prandtl number and adiabatic exponent can be written in the standard propagation-collision form as [79],

$$f_i(\mathbf{x}, t) = f_i(\mathbf{x} - \mathbf{v}_i \delta t, t - \delta t) + \omega_1 (f_i^{eq} - f_i) + (\omega_1 - \omega_2) f_i^*, \quad (7.2)$$

$$g_i(\mathbf{x}, t) = g_i(\mathbf{x} - \mathbf{v}_i \delta t, t - \delta t) + \omega_1 (g_i^{eq} - g_i) + (\omega_1 - \omega_2) g_i^*, \quad (7.3)$$

where  $f_i(\mathbf{x}, t)$  and  $g_i(\mathbf{x}, t)$  are populations at a monitoring point  $\mathbf{x}$  and time  $t$ ,  $f_i^{eq}$ ,  $g_i^{eq}$  are local equilibria,  $f_i^*$ ,  $g_i^*$  are quasi-equilibrium populations and  $\omega_1$ ,  $\omega_2$  are relaxation parameters related to the dynamic viscosity and thermal conductivity,

$$\mu = \left( \frac{1}{\omega_1} - \frac{1}{2} \right) \rho T \delta t, \quad (7.4)$$

$$\kappa = \left( \frac{1}{\omega_2} - \frac{1}{2} \right) C_p \rho T \delta t. \quad (7.5)$$

Here, using the units where universal gas constant  $R = 1$ ,  $C_p = C_v + R$  is the specific heat of ideal gas at constant pressure,  $C_v$  is the specific heat at constant volume, the Prandtl number is  $Pr = C_p \mu / \kappa$  and  $\gamma = C_p / C_v$  is the adiabatic exponent.

The local conservation laws for the density  $\rho$ , momentum  $\rho \mathbf{u}$ , and total energy  $\rho E$  are

$$\rho = \sum_{i=0}^{Q-1} f_i = \sum_{i=0}^{Q-1} f_i^{eq}, \quad (7.6)$$

$$\rho \mathbf{u} = \sum_{i=0}^{Q-1} \mathbf{v}_i f_i = \sum_{i=0}^{Q-1} \mathbf{v}_i f_i^{eq}, \quad (7.7)$$

$$\rho E = \sum_{i=0}^{Q-1} \left( \frac{v_i^2}{2} f_i + g_i \right) = \sum_{i=0}^{Q-1} \left( \frac{v_i^2}{2} f_i^{eq} + g_i^{eq} \right), \quad (7.8)$$

and the temperature is defined by  $T = (1/C_v) (E - u^2/2)$ . Note also that, the higher-order moments, stress tensor  $\sigma$  and heat flux vector  $q$  can be computed as,

$$\sigma = \sum_{i=0}^{Q-1} e_i \otimes e_i (f_i - f_i^{\text{eq}}), \quad (7.9)$$

$$q = \frac{1}{2} \sum_{i=0}^{Q-1} \left[ e_i^2 (f_i - f_i^{\text{eq}}) + (g_i - g_i^{\text{eq}}) \right] e_i, \quad (7.10)$$

where the relative velocity  $e_i$  is

$$e_i = v_i - u. \quad (7.11)$$

The distinctive feature of the PonD is that the kinetic equations (7.2) and (7.3) are formulated in the reference frame moving with the local fluid velocity  $u(x, t)$  and temperature  $T(x, t)$ , i.e.  $\lambda(x, t) = \{u, T\}$ . In this co-moving reference frame, the equilibrium populations are functions of the local density  $\rho(x, t)$  and temperature  $T(x, t)$  only,

$$f_i^{\text{eq}} = \rho W_i, \quad (7.12)$$

$$g_i^{\text{eq}} = \rho W_i (C_v - \frac{D}{2}) T, \quad (7.13)$$

where  $D$  is dimension and the weights  $W_i$  are known for different speed sets  $\mathcal{C}$  and listed in Table 2.1. The equilibrium (7.13) make PonD with the simple Bhatnagar-Gross-Krook (BGK) collision term, stable and accurate for the computation of high-speed flows [126], as there is no error proportional to fluid velocity in the equilibrium moments.

The quasi-equilibrium populations in the co-moving reference frame can also be written as [79],

$$f_i^* = W_i \frac{Q : \left( \theta^{3/2} e_i \otimes e_i \otimes e_i - T \theta^{1/2} \text{sym}(e_i \otimes I) \right)}{6T^3}, \quad (7.14)$$

$$g_i^* = W_i \frac{\theta^{1/2} \zeta \cdot e_i}{T}, \quad (7.15)$$

where  $\text{sym}(\dots)$  denotes symmetrization,  $''\cdot''$  indicates full contraction,  $\theta = T/T_L$  is the reduced temperature,  $Q$  is the nonequilibrium third-order flux

tensor, and  $\varsigma$  is the energy flux associated with the internal degrees of freedom,

$$\mathbf{Q} = \sum_{i=0}^{Q-1} \mathbf{e}_i \otimes \mathbf{e}_i \otimes \mathbf{e}_i \left( f_i - f_i^{eq} \right), \quad (7.16)$$

$$\varsigma = \sum_{i=0}^{Q-1} \mathbf{e}_i \left( g_i - g_i^{eq} \right). \quad (7.17)$$

The crucial part of the PonD algorithm is the propagation step. In order for the equilibrium populations to be exact (see (7.12) and (7.13)), propagation should be performed in the local co-moving reference frame  $\lambda = \{\mathbf{u}, T\}$ , which is undetermined before the propagation. Nevertheless, it is possible to find that during the propagation step and through a predictor-corrector procedure: the propagation is first performed with an initial predictor reference frame (usually the velocity and temperature of the previous time step) leading to find the corrector reference frame, with which the propagation is executed again. This predictor-corrector process continues until convergence and ensures that the propagation is performed in the local co-moving reference frame, and that makes the local equilibrium populations exact. For the detailed description of the propagation step in PonD, see [126, 199, 200].

### 7.3 THE SHOCK STRUCTURE PROBLEM

Shock structure is one of the classical problems in the kinetic theory of gases [201]. It is known that the conventional continuum models, such as the NSF equations, fail to ensure a correct description of the shock wave structure [202], as the thermodynamic variables vary on the scale of a few mean free paths and nonequilibrium effects are dominant. Important to note that, shock structure is a one-dimensional steady-state problem without wall boundaries which eliminates the issues regarding gas-wall interactions. Therefore, it is particularly interesting to consider the applicability of the PonD for solving this nonequilibrium problem.

A classical experimental study of shock wave structure accompanied with DSMC results has been done by Alsmeyer [202]. Particle methods like molecular dynamics (MD) and DSMC [64] provide the most accurate results in a wide range of Mach numbers compared to experimental results. Numerous high-order hydrodynamic models have also been used for studying shock structure problem [see 56, 203–205]. Moreover, there are



numerical methods that solve the Boltzmann equation, noteworthy is the work of Ohwada [206] who calculated the full non-linear collision integral for the hard sphere molecules. However, so far no LB model has succeeded in computing the shock structure problem. Therefore, to demonstrate the advantage of PonD for simulation of high-speed flows, we investigate its accuracy and performance for computing the structure of a plane shock wave.

A one-dimensional plane shock wave is considered. The initial condition is a step at the center of the computational domain, where the flow values upstream and downstream of the shock wave are related by the Rankine-Hugoniot conditions [99]. The upstream mean free path for the hard sphere molecules is defined as,

$$\lambda_1 = \frac{16}{5\sqrt{2\pi}\gamma} \frac{\mu_1 a_1}{P_1}, \quad (7.18)$$

where  $\gamma = 5/3$  is the adiabatic exponent for monatomic gases and  $P_1$ ,  $a_1$  and  $\mu_1$  are the pressure, speed of sound, and dynamic viscosity of the gas upstream of the shock, respectively. The viscosity-temperature relation is

$$\mu = \mu_1 (T/T_1)^s, \quad (7.19)$$

and the hard sphere molecules correspond to  $s = 0.5$ .

The results are produced with a quasi one-dimensional setup and  $D2Q16$ ,  $D2Q25$  lattices. The steady-state non-dimensional density, temperature, normal stress and heat flux, defined as,

$$\rho_n = \frac{\rho - \rho_1}{\rho_2 - \rho_1}, \quad T_n = \frac{T - T_1}{T_2 - T_1}, \quad \hat{\sigma}_{xx} = \frac{\sigma_{xx}}{p_1}, \quad \hat{q}_x = \frac{q_x}{p_1 \sqrt{2T_1}},$$

through the shock wave are compared with the numerical results of solving the Boltzmann collision integral presented by Ohwada [206]. The subscript 2, denotes the downstream of the shock wave. The origin of the coordinate system is adjusted to the point with  $\rho_n = 0.5$  and  $x$  is non-dimensionalized as  $x_n = x/0.5\sqrt{\pi}\lambda_1$ .

The numerical computation has been carried out for  $Ma = 1.2$ , 2 and the results are shown in Figs. 7.1. For  $Ma = 1.2$ , both  $D2Q16$  and  $D2Q25$  lattices give identical results which are in excellent agreement with Ohwada [206]. This demonstrates that the PonD is able to resolve the structure of shock wave. At  $Ma = 2$ , in spite of some deviations at upstream flow part, the results of  $D2Q25$  lattice are still in reasonable agreement with the results of solving the Boltzmann equation. We can, therefore, conclude that PonD is able to resolve the shock structure with good accuracy.

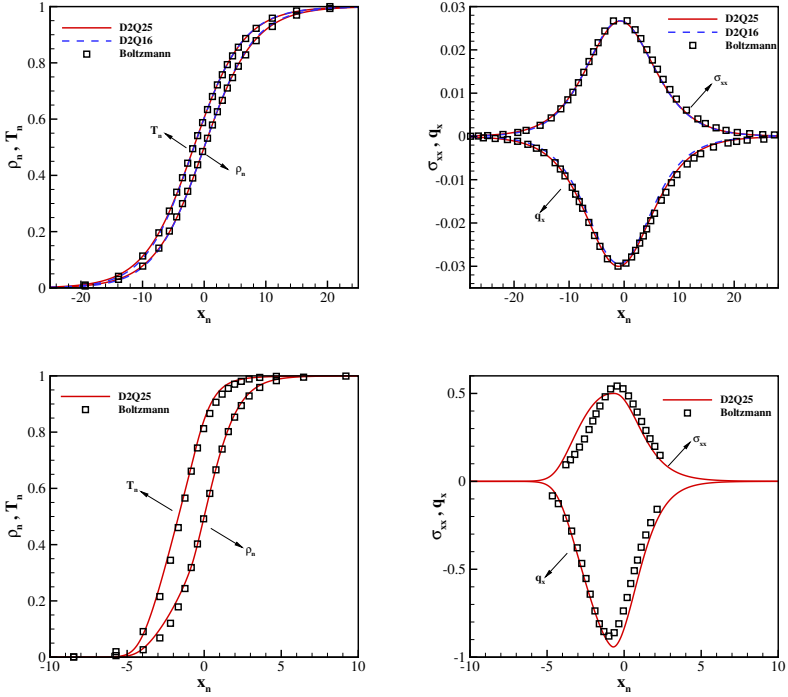


FIGURE 7.1: The density and temperate profiles (left) and the normal stress and heat flux profiles (right) for the shock structure at  $Ma = 1.2$  (top) and  $Ma = 2$  (bottom) using PonD method. Comparisons are made with the results of Ohwada [206].

## 7.4 CONCLUSION

The recently introduced Particles on Demand (PonD) method solves the kinetic equations in a co-moving reference frame which is optimal in terms of equilibrium accuracy, making it attractive for the simulation of high-speed nonequilibrium flows. The classical shock structure problem was computed and the numerical results were compared with the results of solving the full non-linear Boltzmann collision integral. The results show that the PonD is able to resolve the shock structure with good accuracy.



## SUMMARY AND FUTURE WORKS

-*"Let's go."*  
 -*"We can't."*  
 -*"Why not?"*  
 -*"We're waiting for Godot."*

— Samuel Beckett

## 8.1 SUMMARY

With the standard discrete velocities, it is possible to develop an error-free, fully Galilean invariant kinetic model in the co-moving reference frame. However, this requires off-lattice particles' velocities. Sticking with the fixed, lattice-conform velocities, one is faced with an inevitable and persistent error in the stress tensor, which spoils the hydrodynamic equations whenever the flow velocity is increased or the temperature deviates from the lattice reference value. The origin of this anomaly is the geometric constraint of the standard lattices  $c_i^3 = c_i$ , which leads to a deviation in the diagonal components of the third-order equilibrium moment.

In this thesis, we proposed two LB models to address this issue and enlarge the operating range of the classical LBM to fully compressible flows. Both models were based on the two-population framework, where conservation laws are split between two sets of populations: one represents the mass and momentum, while another one is earmarked for the energy conservation. In particular, in model I, a non-local correction term was directly introduced into the kinetic equations in the form of a force term to remove the spurious terms in the stress tensor. Moreover, the construction of energy equilibrium population was based on minimally required moments for recovering the correct energy equation in the hydrodynamic limit. In model II, on the other hand, we annihilated the anomaly by suggesting an extended equilibrium. The extended equilibrium was realized through a product-form, which allows us to compensate the diagonal third-order moment anomaly in the hydrodynamic limit by adding consistent correction terms to the diagonal elements of the second-order moment. As a result, the formulation of correction terms was simpler compared to model I. Furthermore, the construction of energy equilibrium population was improved by using the

product-form formulation which recovers all Maxwell-Boltzmann moments supported by the lattice stencil. Model II, thus, provides a kinetically consistent model with simpler formulation of correction terms compared to model I. Both models, however, were shown to restore the Galilean invariance and temperature independence in a sufficiently wide range and recover the full Navier–Stokes–Fourier equations with variable Prandtl number and adiabatic exponent in the hydrodynamic limit.

Two different strategies then proposed to increase the operating range of the models to supersonic flows involving shock waves. The first strategy relied on the concept of the shifted lattices, a general approach which extends the operating range of any lattice kinetic model by formulating the kinetic equations in a reference frame moving with a constant predefined velocity. While shifted lattice increases the stability domain to Mach number range up-to  $Ma \approx 2.5$ , its drawback is the necessity of off-lattice propagation. The second strategy, only applicable to model II, was based on the upwind discretization of correction term as opposed to central scheme. Consequently, this approach provides a way to simulate moderately supersonic flows up-to  $Ma \approx 1.5$ , while maintaining the simplicity and efficiency of the on-lattice propagation.

The model formulation was extended to compressible flows over complex geometries on unstructured body-fitted meshes. The extension was based on the semi-Lagrangian propagation on unstructured finite element mesh and Grad's approximation for replacing missing populations near the wall boundaries. It was validated by simulating benchmark cases including: subsonic/supersonic flow over airfoil and shock-vortex interaction in Schardin's problem. A solution methodology based on the Arbitrary Lagrangian-Eulerian technique was then proposed for handling moving objects with unstructured body-fitted mesh and interesting applications such as plunging/pitching airfoil with different amplitudes and frequencies were thoroughly investigated.

As a rigorous test for validity of the extended compressible model developed, its accuracy and performance in dealing with challenging case of compressible turbulence was investigated. Extended model II with on-lattice propagation was used for the simulation of decaying of compressible homogeneous isotropic turbulence. It was demonstrated that the model can accurately capture compressibility effects, turbulence fluctuations and shocks. It was shown that the model performs well even at high turbulent Mach number, where eddy-shocklets exist in the flow field and interact with

turbulence. The results of the model were found to be in good agreement with DNS results.

## 8.2 FUTURE WORKS

In order to further validate the suitability of the extended models proposed for compressible turbulent applications, more benchmark cases need to be simulated. The promising results of the proposed models on standard lattices open interesting prospects towards the numerical simulation of more complex applications such as compressible jet flow [207], shock turbulence [208, 209] or shock boundary-layer interactions [210, 211]. The range of applications can also go in the direction of multi-phase flows or magnetohydrodynamics, where compressibility effects play an important role.

Furthermore, with the model formulation on unstructured moving meshes, one can also tackle interesting applications, such as the dynamic stall problem in compressible flows [174], flows involving multiple moving/deforming objects or fluid-solid interaction (FSI) problems. For problems including deformation or relative motion of multiple objects, a blending function is needed to construct the mapping function, as it was proposed in Persson, Bonet & Peraire [153].

The main limitation of the proposed models is the restriction in Mach number range, where with shifted lattices Mach number is in a range up to  $Ma \approx 2.5$  and with on-lattice scheme up to  $Ma \approx 1.5$ . Widening the Mach number range is, however, a challenging task. One way, nonetheless, could be to incorporate additional correction terms in order to compensate the effect of deviations in higher-order equilibrium moments (higher than three).

Future model development should also be directed towards increasing the stability domain in terms of Reynolds number. This can be achieved by augmenting the model with more advanced collision models such as multiple-relaxation-time (MRT) schemes, since the BGK collision term used in this work, is well known to suffer from numerical instabilities at high Reynolds numbers.





## APPENDIX

---

### A.1 COMPARISON OF EXTENDED LBGK TO LOCALLY CORRECTED LBM [44]

Below, we compare the locally corrected lattice Boltzmann model (LC LBM) [44] with both the standard and the present extended LBGK [102]. To that end, it suffices to consider the one-dimensional  $D1Q3$  lattice. In order to introduce the LC LBM, we begin with the standard LBGK ( $\delta t = 1$ ,  $R = 1$ ),

$$f_i(x + v_i, t + 1) - f_i(x, t) = \omega(f_i^{\text{eq}} - f_i). \quad (\text{A.1})$$

The equilibrium populations in (A.1) are given by (3.199) and (3.35),

$$f_i^{\text{eq}} = \rho \Psi_i(u_x, \mathcal{P}_{xx}^{\text{eq}}, 1), \quad \mathcal{P}_{xx}^{\text{eq}} = T + u_x^2, \quad i \in \{-1, 0, 1\}. \quad (\text{A.2})$$

Thanks to the diagonal anomaly, the second-order asymptotic analysis results in the following viscous stress in the one-dimensional version of the Navier–Stokes equation (3.94),

$$\Pi_{xx} = -2 \left( \frac{1}{\omega} - \frac{1}{2} \right) \rho T \partial_x u_x + \tilde{\Pi}_{xx}. \quad (\text{A.3})$$

For the LBGK model, the anomalous (second) term in (A.3) reads,

$$\tilde{\Pi}_{xx}^{\text{LBGK}} = - \left( \frac{1}{\omega} - \frac{1}{2} \right) \left[ \left( \frac{1 - 3T}{2T} - \frac{3u_x^2}{2T} \right) 2\rho T \partial_x u_x + \left( u_x(1 - 3T) - u_x^3 \right) \partial_x \rho \right]. \quad (\text{A.4})$$

Upon realizing that the first term of the anomalous contribution (A.4) is similar in its structure to the relevant (first) term in the LBGK stress (A.3), the locally corrected (LC) LBGK groups these two terms together and replaces the relaxation parameter  $\omega$  in (A.1) with a new relaxation  $\omega_{\text{LC}}$ , which depends on the flow velocity. While the original work [44] addressed the case of the lattice temperature,  $T = T_L = 1/3$  (3.206), we first consider a slightly more general formulation for a flexible temperature parameter.

Consequently, the locally corrected relaxation parameter  $\omega_{\text{LC}}$  in the LBGK equation (A.1) is defined as,

$$\frac{1}{\omega_{\text{LC}}} - \frac{1}{2} = \left( \frac{1}{\omega} - \frac{1}{2} \right) X, \quad (\text{A.5})$$

where the renormalization factor  $X$  reads,

$$X = \left( 1 + \frac{1-3T}{2T} - \frac{3u_x^2}{2T} \right)^{-1}. \quad (\text{A.6})$$

The LBGK model with the locally corrected relaxation parameter  $\omega_{\text{LC}}$  (A.5) results in the viscous stress of the form (A.3), with the remaining error term,

$$\tilde{\Pi}_{xx}^{\text{LC}} = - \left( \frac{1}{\omega} - \frac{1}{2} \right) X \left( u_x(1-3T) - u_x^3 \right) \partial_x \rho. \quad (\text{A.7})$$

For the sake of a discussion, let us introduce the local Mach number,  $\text{Ma}_x = u_x / \sqrt{T}$ . For a quasi-incompressible (slow) flow, the density variation scales as  $\partial_x \rho \sim \text{Ma}_x^2$ . Thus, for  $T \neq T_L$ , the error (A.7) can be estimated as,  $\tilde{\Pi}_{xx}^{\text{LC}} \sim \text{Ma}_x^3$ . This is two orders of magnitude lower than the error of the original LBGK at  $T \neq T_L$ , cf. Eq. (A.4), at small Mach number. Moreover, by setting the temperature  $T = T_L = 1/3$ , it was first realized in Ref. [44] that the error (A.7) reduces to,

$$\tilde{\Pi}_{xx}^{\text{LC}} = \left( \frac{1}{\omega} - \frac{1}{2} \right) \left( \frac{T_L^{3/2} \text{Ma}_x^3}{1 - (3/2) \text{Ma}_x^2} \right) \partial_x \rho. \quad (\text{A.8})$$

In this case, the scaling at  $\text{Ma}_x \rightarrow 0$  becomes,  $\tilde{\Pi}_{xx}^{\text{LC}} \sim \text{Ma}_x^5$ . In other words, the local correction at  $T = T_L$  provides a gain of two orders of magnitude in accuracy with respect to the standard LBGK under the quasi-incompressible flow conditions [44]. This consideration extends straightforwardly to the  $D2Q9$  and  $D3Q27$  lattices by constructing a multiple relaxation time LBM that corrects the relaxation of each diagonal component of the pressure tensor [44].

However, for a generic isothermal flow, the error (A.7) becomes amplified through the renormalization factor (A.6) as the velocity increases and eventually diverges when  $u_x^2 \rightarrow (1-T)/3$ . This error persists also for the special case  $T = T_L$  (A.8). On the other hand, the second-order analysis of Chapman-Enskog reveals that the present LBGK with the extended equilibrium (3.207) removes the entire anomalous term,  $\tilde{\Pi}_{xx}^{\text{ex}} = 0$ . Thus, the

difference between the extended LBGK and the LC LBM [44] is expected beyond the asymptotic  $\text{Ma}_x \rightarrow 0$ .

In order to demonstrate this point, a spectral analysis was performed for the two-dimensional  $D2Q9$  lattice (see [88] for details of the spectral analysis in the LBM context). The normalized spectral dissipation of acoustic modes  $\Im(\omega_\kappa)/\nu\kappa_x^2$ , is shown in Fig. A.1, for  $T = T_L$  and the background flow velocity  $(u_x, u_y) = (0.3, 0)$ , for the three models, the standard LBGK, the present extended LBGK and the LC LBM of Ref. [44]. It can be seen that, the

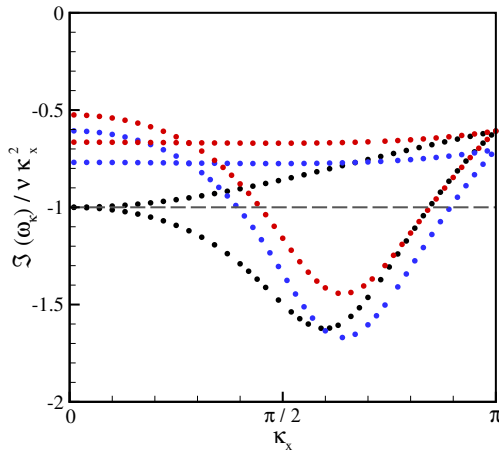


FIGURE A.1: Spectral dissipation of acoustic modes for different models. Red symbols: LBGK; black symbols: extended LBM (3.207); blue symbols: LC LBM [44]; dashed line: Navier–Stokes. The velocity and temperature are set to  $u_x = 0.3$  and  $T = T_L$ .

extended LBGK recovers the correct dissipation rate in the continuum limit (vanishing wave number  $\kappa_x$ ), confirming its Galilean invariance. However, both the standard LBGK and the LC LBM show deviations in the form of under-dissipation at low wave numbers, while the deviation for the LC LBM is indeed smaller. This non-vanishing deviation is amplified in cases with different working temperature and/or non-unit stretching factor for both the standard LBGK and the LC LBM, which makes their applications limited to the quasi-incompressible flow regime at the lattice temperature. Finally, it is interesting to note that, in the case of shock capturing, all the three models are expected to behave similarly, given that their respective

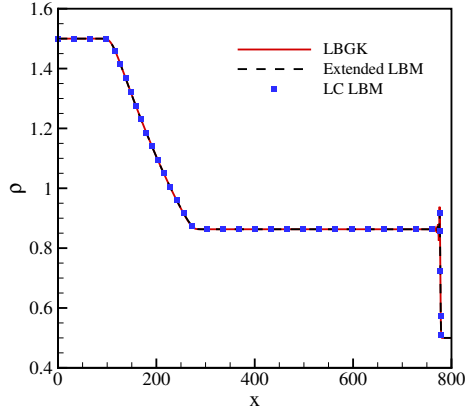


FIGURE A.2: Comparison of density profile for shock tube problem at density ratio  $\rho_l/\rho_r = 3$ , after 500 iterations. Solid line: LBGK; dashed line: extended LBM (3.207); symbols: LC LBM [44].

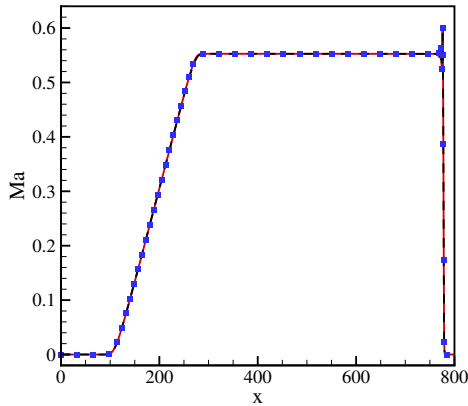


FIGURE A.3: Mach number profile,  $Ma = u/\sqrt{T_L}$ , for the shock tube problem at density ratio  $\rho_l/\rho_r = 3$ , after 500 iterations. Solid line: LBGK; dashed line: extended LBM (3.207); symbols: LC LBM [44].

dissipation rates at the wave number  $\kappa_x = \pi$  are close in value, see Fig. A.1.

This observation is confirmed by the simulation of a shock tube with the following initial condition,

$$(\rho, u_x, T) = \begin{cases} (\rho_l, 0, 1/3), & x \leq L/2, \\ (\rho_r, 0, 1/3), & x > L/2, \end{cases} \quad (\text{A.9})$$

with  $L = 800$  grid points and viscosity  $\nu = 0.04$ . Results are presented in Figs. A.2 and A.3 for  $\rho_l = 1.5$ ,  $\rho_r = 0.5$ , corresponding to the initial density ratio  $\rho_l/\rho_r = 3$ . Figs. A.2 and A.3 demonstrate that all models produce almost indistinguishable results, with a similar oscillation pattern at the shock front.



## A.2 TRANSFER MATRIX FOR EQUILIBRIUM POPULATIONS WITH D2Q9 LATTICE

The transform of the equilibrium populations from rest reference frame to the moving reference frame with velocity  $U$  is done by matching  $Q$  linearly independent moments,

$$M_{mn} = M'_{mn}, \quad (\text{A.10})$$

where  $M_{mn}$  and  $M'_{mn}$  are defined as (see Eq. (4.2) in the main text):

$$M_{mn} = \sum_{i=0}^8 f_i^{eq} c_{ix}^m c_{iy}^n, \quad (\text{A.11})$$

$$M'_{mn} = \sum_{i=0}^8 f_i'^{eq} c_{ix}'^m c_{iy}'^n. \quad (\text{A.12})$$

By considering the following nine linearly independent moments for the D2Q9 lattice,

$$M = (M_{00}, M_{10}, M_{01}, M_{11}, M_{20}, M_{02}, M_{21}, M_{12}, M_{22})^T, \quad (\text{A.13})$$

the matching condition (A.10) can be written in a matrix form as

$$M = \mathcal{M} f^{eq} = \mathcal{M}' f'^{eq}, \quad (\text{A.14})$$

where  $\mathcal{M}$  and  $\mathcal{M}'$  are

$$\mathcal{M} = \begin{bmatrix} 1 & 1 & 1 & 1 & 1 & 1 & 1 & 1 & 1 \\ 0 & 1 & 0 & -1 & 0 & 1 & -1 & -1 & 1 \\ 0 & 0 & 1 & 0 & -1 & 1 & 1 & -1 & -1 \\ 0 & 0 & 0 & 0 & 0 & 1 & -1 & 1 & -1 \\ 0 & 1 & 0 & 1 & 0 & 1 & 1 & 1 & 1 \\ 0 & 0 & 1 & 0 & 1 & 1 & 1 & 1 & 1 \\ 0 & 0 & 0 & 0 & 0 & 1 & 1 & -1 & -1 \\ 0 & 0 & 0 & 0 & 0 & 1 & -1 & -1 & 1 \\ 0 & 0 & 0 & 0 & 0 & 1 & 1 & 1 & 1 \end{bmatrix}, \quad (\text{A.15})$$

$$\mathcal{M}' = \begin{bmatrix} 1 & 1 & 1 & 1 & 1 & 1 & 1 & 1 & 1 \\ U & U+1 & U & U-1 & U & U+1 & U-1 & U-1 & U+1 \\ 0 & 0 & 1 & 0 & -1 & 1 & 1 & -1 & -1 \\ 0 & 0 & U & 0 & -U & U+1 & U-1 & 1-U & -U-1 \\ U^2 & (U+1)^2 & U^2 & (U-1)^2 & U^2 & (U+1)^2 & (U-1)^2 & (U-1)^2 & (U+1)^2 \\ 0 & 0 & 1 & 0 & 1 & 1 & 1 & 1 & 1 \\ 0 & 0 & U^2 & 0 & -U^2 & (U+1)^2 & (U-1)^2 & -(U-1)^2 & -(U+1)^2 \\ 0 & 0 & U & 0 & U & U+1 & U-1 & U-1 & U+1 \\ 0 & 0 & U^2 & 0 & U^2 & (U+1)^2 & (U-1)^2 & (U-1)^2 & (U+1)^2 \end{bmatrix}, \quad (\text{A.16})$$

and  $U$  is the velocity of the moving reference frame. Note that, the enumeration of the discrete velocities  $c_i$  is evident from the second and third row of these matrices. Then, the equilibrium populations in the moving reference frame is computed as,

$$f'^{eq} = \mathcal{G}f^{eq} = \mathcal{M}'^{-1}\mathcal{M}f^{eq}, \quad (\text{A.17})$$

where the transfer matrix  $G$  can be written in the following explicit form

$$\mathcal{G} = \begin{bmatrix} 1-U^2 & -U^2+2U & 0 & -U^2-2U & 0 & 0 & 0 & 0 & 0 \\ \frac{U^2}{2}-\frac{U}{2} & \frac{U^2}{2}-\frac{3U}{2}+1 & 0 & \frac{U^2}{2}+\frac{U}{2} & 0 & 0 & 0 & 0 & 0 \\ 0 & 0 & 1-U^2 & 0 & 0 & -U^2+2U & -U^2-2U & 0 & 0 \\ \frac{U^2}{2}+\frac{U}{2} & \frac{U^2}{2}-\frac{U}{2} & 0 & \frac{U^2}{2}+\frac{3U}{2}+1 & 0 & 0 & 0 & 0 & 0 \\ 0 & 0 & 0 & 0 & 1-U^2 & 0 & 0 & -U^2-2U & -U^2+2U \\ 0 & 0 & \frac{U^2}{2}-\frac{U}{2} & 0 & 0 & \frac{U^2}{2}-\frac{3U}{2}+1 & \frac{U^2}{2}+\frac{U}{2} & 0 & 0 \\ 0 & 0 & \frac{U^2}{2}+\frac{U}{2} & 0 & 0 & \frac{U^2}{2}-\frac{U}{2} & \frac{U^2}{2}+\frac{3U}{2}+1 & 0 & 0 \\ 0 & 0 & 0 & 0 & \frac{U^2}{2}+\frac{U}{2} & 0 & 0 & \frac{U^2}{2}+\frac{3U}{2}+1 & \frac{U^2}{2}-\frac{U}{2} \\ 0 & 0 & 0 & 0 & \frac{U^2}{2}-\frac{U}{2} & 0 & 0 & \frac{U^2}{2}+\frac{U}{2} & \frac{U^2}{2}-\frac{3U}{2}+1 \end{bmatrix}. \quad (\text{A.18})$$



## LIST OF TABLES

---

Table 2.1	Roots of Hermite polynomials $c_{i\alpha}$ , weights of the Gauss–Hermite quadrature $W_{i\alpha}$ and lattice reference temperature $T_L$ . 14
Table 3.1	Moments needed for the computation of $g_i^{eq}$ and $g_i^*$ . 27
Table 5.1	Moments needed for the computation of $f_i^{(1)}$ and $g_i^{(1)}$ . 81
Table 5.2	Accuracy test for the propagation of density perturbation. 83
Table 5.3	Drag coefficient for subsonic flow over NACA0012 airfoil at $Ma = 0.5$ , $Re = 5000$ and $\alpha = 0^\circ$ . 87
Table 5.4	Relative error $\epsilon$ of the velocity $u$ for the free-stream preservation problem. 98



## LIST OF FIGURES

---

- Figure 3.1 Numerical measurement of the fluid viscosity for axis-aligned shear wave setup at temperature  $T = 0.1$  for different velocities. 35
- Figure 3.2 Numerical measurement of the fluid viscosity for rotated shear wave setup at temperature  $T = 0.1$  for different velocities. 36
- Figure 3.3 Numerical measurement of the fluid thermal diffusivity for axis-aligned shear wave setup at Prandtl numbers  $Pr = 0.5, Pr = 1.0$ . 37
- Figure 3.4 Numerical measurement of the speed of sound at three different adiabatic exponents  $\gamma$ . 38
- Figure 3.5 Shock tube simulation results after  $t = 1273$  time steps. (a) Density, (b) temperature and (c) pressure. Line: analytical solution; symbols: present model. 39
- Figure 3.6 Temperature profile for the thermal Couette flow at various Eckert numbers and fixed Prandtl number  $Pr = 0.71$ . Lines: analytical solution; symbols: present model. 40
- Figure 3.7 Temperature profile for the thermal Couette flow at various Prandtl numbers and fixed Eckert number  $Ec = 4.0$ . Lines: analytical solution; symbols: present model. 41
- Figure 3.8 Comparison of temperature profile for the thermal Couette flow with and without correction terms at  $Ec = 4.0$  and  $Pr = 0.71$ . 42
- Figure 3.9 Density (left) and reduced velocity (right) profiles for Sod's shock tube simulation at non-dimensional time  $t^* = 0.2$ . Symbols: present model; line: exact solution. 50
- Figure 3.10 Numerical measurement of viscosity for rotated setup at temperature  $T = 1/3$  for different velocities and stretching ratios. The exact solution corresponds to  $\nu_{num}/\nu = 1$ . 55

- Figure 3.11 Velocity magnitude in lattice units for the decaying homogeneous isotropic turbulence at  $Ma_t = 0.1$ ,  $Re_\Lambda = 72$  and  $t^* = 1.0$  with temperature  $T = 0.55$ . 57
- Figure 3.12 Time evolution of the turbulent kinetic energy for decaying isotropic turbulence at  $Ma_t = 0.1$ ,  $Re_\Lambda = 72$ . Lines: present model; symbol: DNS [115]. 57
- Figure 3.13 Time evolution of the Taylor microscale Reynolds number for decaying isotropic turbulence at  $Ma_t = 0.1$ ,  $Re_\Lambda = 72$ . Lines: present model; symbol: DNS [115] 58
- Figure 3.14 Vorticity field for double shear layer flow at  $t^* = 1$  with regular lattice (left) and stretched lattice (right). Vorticity magnitude is normalized by its maximum value. 59
- Figure 3.15 Evolution of kinetic energy (left) and enstrophy (right) for double shear layer flow at  $Re = 10^4$ . 60
- Figure 3.16 Comparison of the velocity profile at  $x = L_x$  for flow over a flat plate at different stretching ratios. Lines: present model; symbols: Blasius solution. 61
- Figure 3.17 Comparison of the skin friction coefficient for flow over a flat plate at different stretching ratio. Lines: present model; symbols: analytical solution. 62
- Figure 3.18 Snapshot of the velocity magnitude in lattice units for turbulent channel flow at  $Re_\tau = 180$  with  $\lambda_x = 1.4$ . 63
- Figure 3.19 Comparison of the mean velocity profile in a turbulent channel flow at  $Re_\tau = 180$  with  $\lambda_x = 1.4$ . 63
- Figure 3.20 Comparison of the rms of the velocity fluctuations in a turbulent channel flow at  $Re_\tau = 180$  with  $\lambda_x = 1.4$ . Symbols: present model; lines: DNS [120]. 64
- Figure 4.1 Comparison of radial sound pressure distribution  $\Delta P$  for  $Ma_a = 1.2$ ,  $Ma_v = 0.25$  and  $Re = 800$  with the DNS results at three different times  $t^* = 6, 8, 10$ . Lines: present model I; symbol: DNS [127]. 72

- Figure 4.2 Snapshot of sound pressure  $\Delta p$  contours for a passing vortex pair with  $Ma_a = 1.2$ ,  $Ma_v = 0.25$  and  $Re = 800$  at  $t^* = 5$ . Contour levels are from  $\Delta P_{min} = -0.14$  to  $\Delta P_{max} = 0.12$  with an increment of 0.0039. Top: DNS [127],  $\oplus$  denotes the compression region ( $\Delta P > 0$ ) while  $\ominus$  denotes the rarefaction region ( $\Delta P < 0$ ); Bottom: present model I. 73
- Figure 4.3 The sound pressure field  $\Delta P$  of model II for the shock-vortex interaction with  $Ma_a = 1.2$ ,  $Ma_v = 0.25$  and  $Re = 800$  at  $t^* = 6$ . The contour levels are from  $\Delta P_{min} = -0.48$  to  $\Delta P_{max} = 0.16$  with an increment of 0.003216. 74
- Figure 4.4 Comparison of radial sound pressure distribution  $\Delta P$  for  $Ma_a = 1.2$ ,  $Ma_v = 0.25$  and  $Re = 800$  with the DNS results at three different times  $t^* = 6, 8, 10$ . Lines: present model II; symbol: DNS [127]. 75
- Figure 5.1 Schematic of a second-order finite element mesh, the semi-Lagrangian propagation along the discrete velocity  $v_i$  and mapping from the global coordinate  $(x, y)$  to local coordinate  $(\xi, \eta)$ . 78
- Figure 5.2 Schematic representation of the wall boundary condition implementation. 82
- Figure 5.3 Density (left) and velocity (right) distributions for Sod shock tube problem at non-dimensional time  $t^* = 0.2$ . Symbols: present model; line: exact solution. 84
- Figure 5.4 Second-order finite element mesh (Mesh-1) used for the simulation of subsonic flow over NACA0012 airfoil. Bottom is the zoom near leading edge of the airfoil. 85
- Figure 5.5 Mach contour for subsonic flow over NACA0012 airfoil at  $Ma = 0.5$ ,  $Re = 5000$  and  $\alpha = 0^\circ$ . Bottom figure shows streamlines near trailing edge. 86
- Figure 5.6 Distribution of (a) pressure coefficient and (b) skin friction coefficient, on the NACA0012 airfoil surface for subsonic flow at  $Ma = 0.5$ ,  $Re = 5000$  and  $\alpha = 0^\circ$ . Line: present model; symbols: DG solver [134]. 87

- Figure 5.7 Distribution of (a) pressure coefficient and (b) skin friction coefficient, on the NACA0012 airfoil surface for subsonic flow at  $Ma = 0.5$ ,  $Re = 5000$  and  $\alpha = 2^\circ$ . Lines: present model; symbols: reference solution [135]. 88
- Figure 5.8 Mesh-2 used for the simulation of subsonic flow over NACA0012 airfoil. 88
- Figure 5.9 Temperature (top) and Mach number (bottom) contours for supersonic flow over NACA0012 airfoil at  $Ma = 1.5$ ,  $Re = 10000$ . 89
- Figure 5.10 Pressure coefficient upstream, downstream and on the NACA0012 airfoil surface for supersonic flow at  $Ma = 1.5$ ,  $Re = 10000$ . Line: present model with  $D2Q9$  lattice; symbols: ELBM solution with  $D2Q49$  lattice; dashed line: results reported in [138]. 90
- Figure 5.11 Evolution of the density for the Schardin's problem at shock Mach number  $Ma_s = 1.34$ .  $T_1$  and  $T_2$  are triple points. 91
- Figure 5.12 Comparison of the position of triple points  $T_1$  and  $T_2$  for the Schardin's problem. Squares: present model with  $D2Q9$  lattice; dashed Line: ELBM solution with  $D2Q49$  lattice [79]; circles: experiment [140]. 92
- Figure 5.13 Motion of the mesh at non-dimensional time  $t^* = 0$  (top) and  $t^* = 1$  (bottom). 98
- Figure 5.14 Mesh-2 used for the flow over plunging NACA0012 airfoil. Top: overall view; Bottom: zoom near leading edge of the airfoil. 100
- Figure 5.15 Time evolution of lift (top) and drag (bottom) coefficients for slow plunging motion of NACA0012 airfoil with  $h = 0.08c$ ,  $Sr = 0.46$ ,  $Ma = 0.2$  and  $Re = 1850$ . 100
- Figure 5.16 Vorticity computed by the present model (top) and the experimental results reported by Jones, Dohring & Platzler [167] (bottom), for slow plunging motion of NACA0012 airfoil with  $h = 0.08c$  and  $Sr = 0.46$ . Contour levels are bounded between  $-6 \leq \Omega c/u_\infty \leq 6$ . 101

- Figure 5.17 Vorticity computed by the present model (top) and the experimental results reported by Jones, Dohring & Platzter [167] (bottom), for fast plunging motion of NACA0012 airfoil with  $h = 0.12c$  and  $Sr = 1.5$ . Contour levels are bounded between  $-6 \leq \Omega c/u_\infty \leq 6$ . 102
- Figure 5.18 Time evolution of lift (top) and drag (bottom) coefficients for fast plunging motion of NACA0012 airfoil with  $h = 0.12c$ ,  $Sr = 1.5$ ,  $Ma = 0.2$  and  $Re = 1850$ . 103
- Figure 5.19 Vorticity computed by the present model (top) and the experimental results reported by Koochesfahani [175] (bottom) for pitching motion of NACA0012 airfoil with  $A = 2^\circ$  and  $k = 6.68$ . Contour levels are bounded between  $-11.5 \leq \Omega c/u_\infty \leq 11.5$ . 104
- Figure 5.20 Mean streamwise velocity profile at a location one chord downstream of the airfoil trailing edge, for pitching motion of NACA0012 airfoil with  $A = 2^\circ$ ,  $k = 5.2$  and  $Re = 12600$ . Comparison is made with the experimental results of Bohl & Koochesfahani [176]. 105
- Figure 5.21 Time evolution of lift (top) and drag (bottom) coefficients for pitching motion of NACA0012 airfoil with  $A = 2^\circ$ ,  $k = 6.68$ ,  $Ma = 0.08$  and  $Re = 12000$ . 106
- Figure 5.22 Time evolution of lift (top) and drag (bottom) coefficients for pitching motion of NACA0012 airfoil with  $A = 2^\circ$ ,  $k = 10$  and  $Re = 12000$ . Lines:  $Ma = 0.08$ ; lines with symbols:  $Ma = 0.2$ . 106
- Figure 5.23 Amplitude of the lift (top) and thrust (bottom) forces acting on the NACA0012 airfoil under pitching motion with  $A = 2^\circ$  at different reduced frequencies and  $Re = 16600$ . Comparison is made with the experimental results of Mackowski and Williamson [142]. 107
- Figure 5.24 Comparison of the mean thrust coefficient with experimental and numerical results. 107

- Figure 5.25 Mach number (top) and Vorticity (bottom) computed by the present model for pitching motion of NACA0012 airfoil with  $A = 2^\circ$ ,  $k = 3.0$  and  $Ma = 0.85$ . Vorticity contour levels are bounded between  $-11 \leq \Omega c/u_\infty \leq 11$ . 108
- Figure 5.26 Time evolution of lift and drag coefficients for pitching motion of NACA0012 airfoil with  $A = 2^\circ$ ,  $k = 3$ ,  $Ma = 0.85$  and  $Re = 10000$ . 109
- Figure 6.1 Iso-surface of velocity divergence  $\nabla \cdot \mathbf{u} = 0.005$ , colored by local Mach number for compressible decaying turbulence at  $Ma_t = 0.3$ ,  $Re_\lambda = 72$  and  $t^* = 0.4$ . 113
- Figure 6.2 Decay of the turbulent Mach number for compressible decaying turbulence at  $Ma_t = 0.3$  and  $Re_\lambda = 72$ . Lines: present model; symbol: DNS [115]. 114
- Figure 6.3 Decay of the turbulent kinetic energy for compressible decaying turbulence at  $Ma_t = 0.3$  and  $Re_\lambda = 72$ . Lines: present model; symbol: DNS [115]. 115
- Figure 6.4 Time history of root mean square of dilatation for compressible decaying turbulence at  $Ma_t = 0.3$  and  $Re_\lambda = 72$ . Lines: present model; symbol: DNS [115]. 116
- Figure 6.5 Time history of root mean square of density for compressible decaying turbulence at  $Ma_t = 0.3$  and  $Re_\lambda = 72$ . Lines: present model; symbol: DNS [115]. 117
- Figure 6.6 Time history of enstrophy for compressible decaying turbulence at  $Ma_t = 0.3$  and  $Re_\lambda = 72$ . Lines: present model; symbol: DNS [195]. 117
- Figure 6.7 Convergence rate of enstrophy for grid resolutions  $64^3$  to  $512^3$ . Symbols:  $L_\infty$  error of enstrophy with respect to the DNS results; dashed line: second-order slope. 118
- Figure 6.8 Effect of deviation discretization on the enstrophy evolution for compressible decaying turbulence at  $Ma_t = 0.3$  and  $Re_\lambda = 72$ . Lines: present model with first-order upwind discretization of deviation term; symbols: present model with second-order central difference discretization of deviation term. 118



- Figure 6.9 Iso-surface of velocity divergence  $\nabla \cdot \mathbf{u} = 0.015$ , colored by local Mach number for compressible decaying turbulence at  $\text{Ma}_t = 0.5$ ,  $\text{Re}_\lambda = 72$  and  $t^* = 0.4$ . 119
- Figure 6.10 Decay of the turbulent kinetic energy for compressible decaying turbulence at  $\text{Ma}_t = 0.5$  and  $\text{Re}_\lambda = 72$ . Lines: present model; symbol: DNS [115]. 119
- Figure 6.11 Time history of root mean square of density for compressible decaying turbulence at  $\text{Ma}_t = 0.5$  and  $\text{Re}_\lambda = 72$ . Lines: present model; symbol: DNS [115]. 120
- Figure 6.12 Time history of Taylor microscale Reynolds number for compressible decaying turbulence at  $\text{Ma}_t = 0.5$  and  $\text{Re}_\lambda = 72$ . Lines: present model; symbol: DNS [115]. 120
- Figure 6.13 Decay of the turbulent kinetic energy for compressible decaying turbulence at  $\text{Ma}_t = 0.488$  and  $\text{Re}_\lambda = 175$ . Line: present model; symbol: DNS [115]. 121
- Figure 6.14 Time history of the dissipation rate for compressible decaying turbulence at  $\text{Ma}_t = 0.488$  and  $\text{Re}_\lambda = 175$ . Line: present model; symbol: DNS [115]. 121
- Figure 6.15 Time history of Taylor microscale Reynolds number for compressible decaying turbulence at  $\text{Ma}_t = 0.488$  and  $\text{Re}_\lambda = 175$ . Line: present model; symbol: DNS [115]. 122
- Figure 6.16 Energy spectrum at various times ( $t^* = 0, 1$  and  $3$ ) for compressible decaying turbulence at  $\text{Ma}_t = 0.488$  and  $\text{Re}_\lambda = 175$ . Dashed line is the initial spectrum ( $t^* = 0$ ). Here,  $\eta$  is the Kolmogorov length scale. 123
- Figure 7.1 The density and temperate profiles (left) and the normal stress and heat flux profiles (right) for the shock structure at  $\text{Ma} = 1.2$  (top) and  $\text{Ma} = 2$  (bottom) using PonD method. Comparisons are made with the results of Ohwada [206]. 130
- Figure A.1 Spectral dissipation of acoustic modes for different models. Red symbols: LBGK; black symbols: extended LBM (3.207); blue symbols: LC LBM [44]; dashed line: Navier–Stokes. The velocity and temperature are set to  $u_x = 0.3$  and  $T = T_L$ . 139

- Figure A.2      Comparison of density profile for shock tube problem at density ratio  $\rho_l/\rho_r = 3$ , after 500 iterations. Solid line: LBGK; dashed line: extended LBM (3.207); symbols: LC LBM [44].      140
- Figure A.3      Mach number profile,  $Ma = u/\sqrt{T_L}$ , for the shock tube problem at density ratio  $\rho_l/\rho_r = 3$ , after 500 iterations. Solid line: LBGK; dashed line: extended LBM (3.207); symbols: LC LBM [44].      140

## BIBLIOGRAPHY

---

1. Jameson, A. Computational Fluid Dynamics: Past, Present and Future. *Future Directions in CDF Research, National Institute for Aerospace*, 75 (2012).
2. Caughey, D. A. *Computational aerodynamics* (Elsevier, 2003).
3. Von Neumann, J. & Richtmyer, R. D. A method for the numerical calculation of hydrodynamic shocks. *Journal of applied physics* **21**, 232 (1950).
4. McNamara, G. R. & Zanetti, G. Use of the Boltzmann equation to simulate lattice-gas automata. *Physical review letters* **61**, 2332 (1988).
5. Succi, S. *The lattice Boltzmann equation: for fluid dynamics and beyond* (Oxford university press, 2001).
6. d’Humières, D., Lallemand, P. & Frisch, U. Lattice gas models for 3D hydrodynamics. *EPL (Europhysics Letters)* **2**, 291 (1986).
7. Frisch, U., Hasslacher, B. & Pomeau, Y. Lattice-gas automata for the Navier-Stokes equation. *Physical review letters* **56**, 1505 (1986).
8. Shan, X. & He, X. Discretization of the velocity space in the solution of the Boltzmann equation. *Physical Review Letters* **80**, 65 (1998).
9. Shan, X., Yuan, X.-F. & Chen, H. Kinetic theory representation of hydrodynamics: a way beyond the Navier–Stokes equation. *Journal of Fluid Mechanics* **550**, 413 (2006).
10. Ansumali, S., Karlin, I., Arcidiacono, S., Abbas, A. & Prasianakis, N. Hydrodynamics beyond Navier-Stokes: Exact solution to the lattice Boltzmann hierarchy. *Physical review letters* **98**, 124502 (2007).
11. Higuera, F., Succi, S. & Benzi, R. Lattice gas dynamics with enhanced collisions. *EPL (Europhysics Letters)* **9**, 345 (1989).
12. Succi, S., Benzi, R. & Higuera, F. The lattice Boltzmann equation: a new tool for computational fluid-dynamics. *Physica D: Nonlinear Phenomena* **47**, 219 (1991).
13. Benzi, R., Succi, S. & Vergassola, M. The lattice Boltzmann equation: theory and applications. *Physics Reports* **222**, 145 (1992).

14. Chen, H., Kandasamy, S., Orszag, S., Shock, R., Succi, S. & Yakhot, V. Extended Boltzmann kinetic equation for turbulent flows. *Science* **301**, 633 (2003).
15. Chikatamarla, S., Ansumali, S. & Karlin, I. V. Entropic lattice Boltzmann models for hydrodynamics in three dimensions. *Physical review letters* **97**, 010201 (2006).
16. Geier, M., Greiner, A. & Korvink, J. G. Cascaded digital lattice Boltzmann automata for high Reynolds number flow. *Physical Review E* **73**, 066705 (2006).
17. Latt, J. & Chopard, B. Lattice Boltzmann method with regularized pre-collision distribution functions. *Mathematics and Computers in Simulation* **72**, 165 (2006).
18. Chikatamarla, S. S. & Karlin, I. V. Entropic lattice Boltzmann method for turbulent flow simulations: Boundary conditions. *Physica A: Statistical Mechanics and its Applications* **392**, 1925 (2013).
19. Karlin, I. V., Bösch, F., Chikatamarla, S. S. & Succi, S. Entropy-assisted computing of low-dissipative systems. *Entropy* **17**, 8099 (2015).
20. Geier, M., Schönherr, M., Pasquali, A. & Krafczyk, M. The cumulant lattice Boltzmann equation in three dimensions: Theory and validation. *Computers & Mathematics with Applications* **70**, 507 (2015).
21. Dorschner, B., Bösch, F., Chikatamarla, S. S., Boulouchos, K. & Karlin, I. V. Entropic multi-relaxation time lattice Boltzmann model for complex flows. *Journal of Fluid Mechanics* **801**, 623 (2016).
22. Lin, W.-J., Li, M.-J., Su, C.-W., Huang, X.-Y. & Lin, C.-A. Direct numerical simulations of turbulent periodic-hill flows with mass-conserving lattice Boltzmann method. *Physics of Fluids* **32**, 115122 (2020).
23. Shan, X. & Chen, H. Lattice Boltzmann model for simulating flows with multiple phases and components. *Physical review E* **47**, 1815 (1993).
24. Wagner, A. Thermodynamic consistency of liquid-gas lattice Boltzmann simulations. *Physical Review E* **74**, 056703 (2006).
25. Fakhari, A. & Rahimian, M. H. Phase-field modeling by the method of lattice Boltzmann equations. *Physical Review E* **81**, 036707 (2010).
26. Chikatamarla, S., Karlin, I., *et al.* Entropic lattice Boltzmann method for multiphase flows. *Physical review letters* **114**, 174502 (2015).

27. Mazloomi Moqaddam, A., Chikatamarla, S. S. & Karlin, I. V. Simulation of binary droplet collisions with the entropic lattice Boltzmann method. *Physics of Fluids* **28**, 022106 (2016).
28. Guo, Z. & Zhao, T. Lattice Boltzmann model for incompressible flows through porous media. *Physical review E* **66**, 036304 (2002).
29. Fattahi, E., Waluga, C., Wohlmuth, B., Rüde, U., Manhart, M. & Helmig, R. Lattice Boltzmann methods in porous media simulations: From laminar to turbulent flow. *Computers & Fluids* **140**, 247 (2016).
30. Pan, C., Luo, L.-S. & Miller, C. T. An evaluation of lattice Boltzmann schemes for porous medium flow simulation. *Computers & fluids* **35**, 898 (2006).
31. Marié, S., Ricot, D. & Sagaut, P. Comparison between lattice Boltzmann method and Navier–Stokes high order schemes for computational aeroacoustics. *Journal of Computational Physics* **228**, 1056 (2009).
32. Brogi, F., Malaspinas, O., Chopard, B. & Bonadonna, C. Hermite regularization of the lattice Boltzmann method for open source computational aeroacoustics. *The Journal of the Acoustical Society of America* **142**, 2332 (2017).
33. Gendre, F., Ricot, D., Fritz, G. & Sagaut, P. Grid refinement for aeroacoustics in the lattice Boltzmann method: A directional splitting approach. *Physical Review E* **96**, 023311 (2017).
34. Chen, S., Chen, H., Martinez, D. & Matthaeus, W. Lattice Boltzmann model for simulation of magnetohydrodynamics. *Physical Review Letters* **67**, 3776 (1991).
35. Dellar, P. J. Lattice Boltzmann magnetohydrodynamics with current-dependent resistivity. *Journal of Computational Physics* **237**, 115 (2013).
36. Agarwal, R. K. in *Computational Fluid Dynamics 2000* 511 (Springer, 2001).
37. Mendoza, M., Boghosian, B., Herrmann, H. J. & Succi, S. Fast lattice Boltzmann solver for relativistic hydrodynamics. *Physical review letters* **105**, 014502 (2010).
38. Mendoza, M., Boghosian, B., Herrmann, H. J. & Succi, S. Derivation of the lattice Boltzmann model for relativistic hydrodynamics. *Physical Review D* **82**, 105008 (2010).
39. Gabbana, A., Simeoni, D., Succi, S. & Tripiccione, R. Relativistic lattice Boltzmann methods: Theory and applications. *Physics Reports* (2020).

40. Succi, S. Lattice boltzmann 2038. *EPL (Europhysics Letters)* **109**, 50001 (2015).
41. Nishimura, S., Hayashi, K., Nakaye, S., Yoshimoto, M., Suga, K. & Inamuro, T. *Implicit Large-Eddy Simulation of rotating and non-rotating machinery with Cumulant Lattice Boltzmann method aiming for industrial applications in AIAA Aviation 2019 Forum* (2019), 3526.
42. Krause, M. J., Kummerländer, A., Avis, S. J., Kusumaatmaja, H., Dapelo, D., Klemens, F., Gaedtke, M., Hafen, N., Mink, A., Trunk, R., *et al.* OpenLB—Open source lattice Boltzmann code. *Computers & Mathematics with Applications* **81**, 258 (2021).
43. Latt, J., Malaspinas, O., Kontaxakis, D., Parmigiani, A., Lagrava, D., Brogi, F., Belgacem, M. B., Thorimbert, Y., Leclaire, S., Li, S., *et al.* Palabos: parallel lattice Boltzmann solver. *Computers & Mathematics with Applications* **81**, 334 (2021).
44. Dellar, P. J. Lattice Boltzmann algorithms without cubic defects in Galilean invariance on standard lattices. *Journal of Computational Physics* **259**, 270 (2014).
45. Chapman, S. & Cowling, T. G. *The mathematical theory of non-uniform gases: an account of the kinetic theory of viscosity, thermal conduction and diffusion in gases* (Cambridge university press, 1990).
46. Cercignani, C., Illner, R. & Pulvirenti, M. *The mathematical theory of dilute gases* (Springer Science & Business Media, 2013).
47. Villani, C. A review of mathematical topics in collisional kinetic theory. *Handbook of mathematical fluid dynamics* **1**, 3 (2002).
48. Grad, H. On the kinetic theory of rarefied gases. *Communications on pure and applied mathematics* **2**, 331 (1949).
49. Cercignani, C. in *The Boltzmann equation and its applications* 40 (Springer, 1988).
50. Bhatnagar, P. L., Gross, E. P. & Krook, M. A model for collision processes in gases. I. Small amplitude processes in charged and neutral one-component systems. *Physical review* **94**, 511 (1954).
51. Wagner, A. J. A practical introduction to the lattice Boltzmann method. *Adv. notes for Statistical Mechanics* **463**, 663 (2008).
52. Karlin, I. V., Gorban, A. N., Dukek, G. & Nonnenmacher, T. Dynamic correction to moment approximations. *Physical Review E* **57**, 1668 (1998).

53. Torrilhon, M. Modeling nonequilibrium gas flow based on moment equations. *Annual review of fluid mechanics* **48**, 429 (2016).
54. Bird, G. Aspects of the structure of strong shock waves. *The Physics of Fluids* **13**, 1172 (1970).
55. Struchtrup, H. & Torrilhon, M. Regularization of Grad's 13 moment equations: derivation and linear analysis. *Physics of Fluids* **15**, 2668 (2003).
56. Torrilhon, M. & Struchtrup, H. Regularized 13-moment equations: shock structure calculations and comparison to Burnett models. *Journal of Fluid Mechanics* **513**, 171 (2004).
57. McDonald, J. & Torrilhon, M. Affordable robust moment closures for CFD based on the maximum-entropy hierarchy. *Journal of Computational Physics* **251**, 500 (2013).
58. Thatcher, T., Zheng, Y. & Struchtrup, H. Boundary conditions for Grad's 13 moment equations. *Progress in Computational Fluid Dynamics, an International Journal* **8**, 69 (2008).
59. Bird, G. *Molecular Gas Dynamics and the Direct Simulation of Gas Flows*, Clarendon Press, Oxford, 1994 (1994).
60. Wagner, W. A convergence proof for Bird's direct simulation Monte Carlo method for the Boltzmann equation. *J. Stat. Phys.* **66**, 1011 (1992).
61. Gu, X.-J., Barber, R. W., John, B. & Emerson, D. R. Non-equilibrium effects on flow past a circular cylinder in the slip and early transition regime. *Journal of Fluid Mechanics* **860**, 654 (2019).
62. Homolle, T. M. & Hadjiconstantinou, N. G. A low-variance deviational simulation Monte Carlo for the Boltzmann equation. *Journal of Computational Physics* **226**, 2341 (2007).
63. Gorji, M. H., Torrilhon, M. & Jenny, P. Fokker-Planck model for computational studies of monatomic rarefied gas flows. *Journal of fluid mechanics* **680**, 574 (2011).
64. Ren, W., Liu, H. & Jin, S. An asymptotic-preserving Monte Carlo method for the Boltzmann equation. *Journal of Computational Physics* **276**, 380 (2014).
65. Gorji, M. H. & Jenny, P. Fokker-Planck-DSMC algorithm for simulations of rarefied gas flows. *Journal of Computational Physics* **287**, 110 (2015).

66. Enskog, D. The numerical calculation of phenomena in fairly dense gases. *Arkiv Mat. Astr. Fys* **16**, 1 (1921).
67. Chapman, S. V. On the kinetic theory of a gas. Part II.—A composite monatomic gas: diffusion, viscosity, and thermal conduction. *Philosophical Transactions of the Royal Society of London. Series A, Containing Papers of a Mathematical or Physical Character* **217**, 115 (1918).
68. Chapman, S. & Cowling, T. The Mathematical Theory of Non-uniform Gases: An Account of the Kinetic Theory of Viscosity, Thermal Conduction and Diffusion in Gases. Cambridge Mathematical Library. *Cambridge University Press* **1**, 27 (1970).
69. Zhong, X., MacCormack, R. W. & Chapman, D. R. Stabilization of the Burnett equations and application to hypersonic flows. *AIAA journal* **31**, 1036 (1993).
70. Chikatamarla, S. S. & Karlin, I. V. Lattices for the lattice Boltzmann method. *Physical Review E* **79**, 046701 (2009).
71. Succi, S. *The lattice Boltzmann equation: for complex states of flowing matter* (Oxford University Press, Oxford, UK, 2018).
72. Krüger, T., Kusumaatmaja, H., Kuzmin, A., Shardt, O., Silva, G. & Viggen, E. M. *The lattice Boltzmann method* (Springer International Publishing, 2017).
73. Karlin, I. & Asinari, P. Factorization symmetry in the lattice Boltzmann method. *Physica A: Statistical Mechanics and its Applications* **389**, 1530 (2010).
74. Alexander, F. J., Chen, S. & Sterling, J. Lattice boltzmann thermohydrodynamics. *Physical Review E* **47**, R2249 (1993).
75. Kataoka, T. & Tsutahara, M. Lattice Boltzmann model for the compressible Navier-Stokes equations with flexible specific-heat ratio. *Physical review E* **69**, 035701 (2004).
76. Li, Q., He, Y., Wang, Y. & Tao, W. Coupled double-distribution-function lattice Boltzmann method for the compressible Navier-Stokes equations. *Physical Review E* **76**, 056705 (2007).
77. Watari, M. Finite difference lattice Boltzmann method with arbitrary specific heat ratio applicable to supersonic flow simulations. *Physica A: Statistical Mechanics and its Applications* **382**, 502 (2007).
78. Lin, C. & Luo, K. H. MRT discrete Boltzmann method for compressible exothermic reactive flows. *Computers & Fluids* **166**, 176 (2018).



79. Frapolli, N., Chikatamarla, S. S. & Karlin, I. V. Entropic lattice Boltzmann model for gas dynamics: Theory, boundary conditions, and implementation. *Physical Review E* **93**, 063302 (2016).
80. Frapolli, N., Chikatamarla, S. & Karlin, I. Multispeed entropic lattice Boltzmann model for thermal flows. *Physical Review E* **90**, 043306 (2014).
81. Frapolli, N., Chikatamarla, S. S. & Karlin, I. V. Entropic lattice Boltzmann model for compressible flows. *Physical Review E* **92**, 061301 (2015).
82. Frapolli, N. *Entropic lattice Boltzmann models for thermal and compressible flows* PhD thesis (ETH Zurich, 2017).
83. Prasianakis, N. I. & Karlin, I. V. Lattice Boltzmann method for simulation of compressible flows on standard lattices. *Physical Review E* **78**, 016704 (2008).
84. Prasianakis, N. I., Karlin, I. V., Mantzaras, J. & Boulouchos, K. B. Lattice Boltzmann method with restored Galilean invariance. *Physical Review E* **79**, 066702 (2009).
85. Guo, Z., Zheng, C., Shi, B. & Zhao, T. Thermal lattice Boltzmann equation for low Mach number flows: decoupling model. *Physical Review E* **75**, 036704 (2007).
86. Feng, Y., Sagaut, P. & Tao, W. A three dimensional lattice model for thermal compressible flow on standard lattices. *Journal of Computational Physics* **303**, 514 (2015).
87. Saadat, M. H., Bösch, F. & Karlin, I. V. Lattice Boltzmann model for compressible flows on standard lattices: Variable Prandtl number and adiabatic exponent. *Physical Review E* **99**, 013306 (2019).
88. Hosseini, S. A., Darabiha, N. & Thévenin, D. Compressibility in lattice Boltzmann on standard stencils: effects of deviation from reference temperature. *Philosophical Transactions of the Royal Society A* **378**, 20190399 (2020).
89. Feng, Y., Sagaut, P. & Tao, W.-Q. A compressible lattice Boltzmann finite volume model for high subsonic and transonic flows on regular lattices. *Computers & Fluids* **131**, 45 (2016).
90. Feng, Y., Boivin, P., Jacob, J. & Sagaut, P. Hybrid recursive regularized thermal lattice Boltzmann model for high subsonic compressible flows. *Journal of Computational Physics* **394**, 82 (2019).

91. Guo, S., Feng, Y. & Sagaut, P. Improved standard thermal lattice Boltzmann model with hybrid recursive regularization for compressible laminar and turbulent flows. *Physics of Fluids* **32**, 126108 (2020).
92. Renard, F., Feng, Y., Boussuge, J.-F. & Sagaut, P. Improved compressible hybrid lattice Boltzmann method on standard lattice for subsonic and supersonic flows. *Computers & Fluids* **219**, 104867 (2021).
93. Zhao, S., Farag, G., Boivin, P. & Sagaut, P. Toward fully conservative hybrid lattice Boltzmann methods for compressible flows. *Physics of Fluids* **32**, 126118 (2020).
94. Farag, G., Zhao, S., Coratger, T., Boivin, P., Chiavassa, G. & Sagaut, P. A pressure-based regularized lattice-Boltzmann method for the simulation of compressible flows. *Physics of Fluids* **32**, 066106 (2020).
95. Guo, S., Feng, Y. & Sagaut, P. On the use of conservative formulation of energy equation in hybrid compressible lattice Boltzmann method. *Computers & Fluids* **219**, 104866 (2021).
96. Li, Q., Luo, K., He, Y., Gao, Y. & Tao, W. Coupling lattice Boltzmann model for simulation of thermal flows on standard lattices. *Physical Review E* **85**, 016710 (2012).
97. Karlin, I., Sichau, D. & Chikatamarla, S. Consistent two-population lattice Boltzmann model for thermal flows. *Physical Review E* **88**, 063310 (2013).
98. Frapolli, N., Chikatamarla, S. S. & Karlin, I. V. Theory, analysis, and applications of the entropic lattice Boltzmann model for compressible flows. *Entropy* **22**, 370 (2020).
99. Anderson, J. D. *Modern compressible flow: with historical perspective* (McGraw-Hill New York, 1990).
100. Saadat, M. H., Hosseini, S. A., Dorschner, B. & Karlin, I. Extended lattice Boltzmann model for gas dynamics. *Physics of Fluids* **33**, 046104 (2021).
101. Sod, G. A. A survey of several finite difference methods for systems of nonlinear hyperbolic conservation laws. *Journal of computational physics* **27**, 1 (1978).
102. Saadat, M. H., Dorschner, B. & Karlin, I. Extended lattice Boltzmann model. *Entropy* **23**, 475 (2021).
103. Patil, D. V. & Lakshmisha, K. Finite volume TVD formulation of lattice Boltzmann simulation on unstructured mesh. *Journal of Computational Physics* **228**, 5262 (2009).

104. Hejranfar, K. & Ghaffarian, A. A high-order accurate unstructured spectral difference lattice Boltzmann method for computing inviscid and viscous compressible flows. *Aerospace Science and Technology* **98**, 105661 (2020).
105. Krämer, A., Küllmer, K., Reith, D., Joppich, W. & Foysi, H. Semi-Lagrangian off-lattice Boltzmann method for weakly compressible flows. *Physical Review E* **95**, 023305 (2017).
106. Di Ilio, G., Dorschner, B., Bella, G., Succi, S. & Karlin, I. V. Simulation of turbulent flows with the entropic multirelaxation time lattice Boltzmann method on body-fitted meshes. *Journal of Fluid Mechanics* **849**, 35 (2018).
107. Saadat, M. H., Bösch, F. & Karlin, I. V. Semi-Lagrangian lattice Boltzmann model for compressible flows on unstructured meshes. *Physical Review E* **101**, 023311 (2020).
108. Wilde, D., Krämer, A., Reith, D. & Foysi, H. Semi-Lagrangian lattice Boltzmann method for compressible flows. *Physical Review E* **101**, 053306 (2020).
109. Lagrava, D., Malaspinas, O., Latt, J. & Chopard, B. Advances in multi-domain lattice Boltzmann grid refinement. *Journal of Computational Physics* **231**, 4808 (2012).
110. Dorschner, B., Frapolli, N., Chikatamarla, S. S. & Karlin, I. V. Grid refinement for entropic lattice Boltzmann models. *Physical Review E* **94**, 053311 (2016).
111. Zong, Y., Peng, C., Guo, Z. & Wang, L.-P. Designing correct fluid hydrodynamics on a rectangular grid using MRT lattice Boltzmann approach. *Computers & Mathematics with Applications* **72**, 288 (2016).
112. Peng, C., Min, H., Guo, Z. & Wang, L.-P. A hydrodynamically-consistent MRT lattice Boltzmann model on a 2D rectangular grid. *Journal of Computational Physics* **326**, 893 (2016).
113. Zecevic, V., Kirkpatrick, M. P. & Armfield, S. W. Rectangular lattice Boltzmann method using multiple relaxation time collision operator in two and three dimensions. *Computers & Fluids*, 104492 (2020).
114. Dorschner, B., Chikatamarla, S. S., Bösch, F. & Karlin, I. V. Grad's approximation for moving and stationary walls in entropic lattice Boltzmann simulations. *Journal of Computational Physics* **295**, 340 (2015).

115. Samtaney, R., Pullin, D. I. & Kosović, B. Direct numerical simulation of decaying compressible turbulence and shocklet statistics. *Physics of Fluids* **13**, 1415 (2001).
116. Ducasse, L. & Pumir, A. Inertial particle collisions in turbulent synthetic flows: quantifying the sling effect. *Physical Review E* **80**, 066312 (2009).
117. Guo, Z., Zhao, T. S. & Shi, Y. Preconditioned lattice-Boltzmann method for steady flows. *Physical Review E* **70**, 066706 (2004).
118. White, F. M. *Fluid Mechanics* (Tata McGraw-Hill Education, 1979).
119. Kim, J., Moin, P. & Moser, R. Turbulence statistics in fully developed channel flow at low Reynolds number. *Journal of Fluid Mechanics* **177**, 133 (1987).
120. Moser, R. D., Kim, J. & Mansour, N. N. Direct numerical simulation of turbulent channel flow up to  $Re_\tau = 590$ . *Physics of Fluids* **11**, 943 (1999).
121. Lee, M. & Moser, R. D. Direct numerical simulation of turbulent channel flow up to  $Re \approx 5200$ . *Journal of Fluid Mechanics* **774**, 395 (2015).
122. Eckelmann, H. The structure of the viscous sublayer and the adjacent wall region in a turbulent channel flow. *Journal of Fluid Mechanics* **65**, 439 (1974).
123. Kreplin, H.-P. & Eckelmann, H. Behavior of the three fluctuating velocity components in the wall region of a turbulent channel flow. *Physics of Fluids* **22**, 1233 (1979).
124. Wang, L.-P., Peng, C., Guo, Z. & Yu, Z. Lattice Boltzmann simulation of particle-laden turbulent channel flow. *Computers & Fluids* **124**, 226 (2016).
125. Frapolli, N., Chikatamarla, S. S. & Karlin, I. V. Lattice kinetic theory in a comoving galilean reference frame. *Physical review letters* **117**, 010604 (2016).
126. Dorschner, B., Bösch, F. & Karlin, I. V. Particles on Demand for Kinetic Theory. *Phys. Rev. Lett.* **121**, 130602 (13 2018).
127. Inoue, O. & Hattori, Y. Sound generation by shock-vortex interactions. *Journal of Fluid Mechanics* **380**, 81 (1999).

128. Zarghami, A., Ubertini, S. & Succi, S. Finite volume formulation of thermal lattice Boltzmann method. *International Journal of Numerical Methods for Heat & Fluid Flow* **24**, 270 (2014).
129. Di Ilio, G., Dorschner, B., Bella, G., Succi, S. & Karlin, I. Simulation of turbulent flows with the entropic multirelaxation time lattice Boltzmann method on body-fitted meshes. *Journal of Fluid Mechanics* **849**, 35 (2018).
130. Zienkiewicz, O. C., Taylor, R. L. & Zhu, J. Z. *The finite element method: its basis and fundamentals* (Elsevier, 2005).
131. Chikatamarla, S., Ansumali, S. & Karlin, I. Grad's approximation for missing data in lattice Boltzmann simulations. *EPL (Europhysics Letters)* **74**, 215 (2006).
132. Pareschi, G., Frapolli, N., Chikatamarla, S. S. & Karlin, I. V. Conjugate heat transfer with the entropic lattice Boltzmann method. *Physical Review E* **94**, 013305 (2016).
133. Ji, X., Zhao, F., Shyy, W. & Xu, K. A family of high-order gas-kinetic schemes and its comparison with Riemann solver based high-order methods. *Journal of Computational Physics* **356**, 150 (2018).
134. Cheng, J., Yang, X., Liu, T. & Luo, H. A direct discontinuous Galerkin method for the compressible Navier-Stokes equations on arbitrary grids. *Journal of Computational Physics* **327**, 484 (2016).
135. Swanson, R. & Langer, S. Steady-state laminar flow solutions for NACA 0012 airfoil. *Computers & Fluids* **126**, 102 (2016).
136. Yang, X., Cheng, J., Luo, H. & Zhao, Q. A reconstructed direct discontinuous Galerkin method for simulating the compressible laminar and turbulent flows on hybrid grids. *Computers & Fluids* **168**, 216 (2018).
137. Kannan, R. & Wang, Z. The direct discontinuous Galerkin (DDG) viscous flux scheme for the high order spectral volume method. *Computers & Fluids* **39**, 2007 (2010).
138. Hafez, M. & Wahba, E. Simulations of viscous transonic flows over lifting airfoils and wings. *Computers & fluids* **36**, 39 (2007).
139. Schardin, H. High frequency cinematography in the shock tube. *The Journal of Photographic Science* **5**, 17 (1957).
140. Chang, S.-M. & Chang, K.-S. On the shock-vortex interaction in Schardin's problem. *Shock Waves* **10**, 333 (2000).

141. Bose, C. & Sarkar, S. Investigating chaotic wake dynamics past a flapping airfoil and the role of vortex interactions behind the chaotic transition. *Physics of fluids* **30**, 047101 (2018).
142. Mackowski, A. & Williamson, C. Direct measurement of thrust and efficiency of an airfoil undergoing pure pitching. *Journal of Fluid Mechanics* **765**, 524 (2015).
143. Young, J., Lai, J. C. & Platzer, M. F. A review of progress and challenges in flapping foil power generation. *Progress in aerospace sciences* **67**, 2 (2014).
144. Dyke, G., De Kat, R., Palmer, C., Van Der Kindere, J., Naish, D. & Ganapathisubramani, B. Aerodynamic performance of the feathered dinosaur Microraptor and the evolution of feathered flight. *Nature Communications* **4**, 2489 (2013).
145. Boudreau, M., Dumas, G., Rahimpour, M. & Oshkai, P. Experimental investigation of the energy extraction by a fully-passive flapping-foil hydrokinetic turbine prototype. *Journal of Fluids and Structures* **82**, 446 (2018).
146. Xiao, Q. & Zhu, Q. A review on flow energy harvesters based on flapping foils. *Journal of fluids and structures* **46**, 174 (2014).
147. Nguyen, V.-T. An arbitrary Lagrangian–Eulerian discontinuous Galerkin method for simulations of flows over variable geometries. *Journal of Fluids and Structures* **26**, 312 (2010).
148. Feng, Z.-G. & Michaelides, E. E. The immersed boundary-lattice Boltzmann method for solving fluid–particles interaction problems. *Journal of Computational Physics* **195**, 602 (2004).
149. Chen, Z., Shu, C. & Tan, D. Immersed boundary-simplified lattice Boltzmann method for incompressible viscous flows. *Physics of Fluids* **30**, 053601 (2018).
150. Chen, Z., Shu, C., Yang, L., Zhao, X. & Liu, N. Immersed boundary-simplified thermal lattice Boltzmann method for incompressible thermal flows. *Physics of Fluids* **32**, 013605 (2020).
151. Guo, Z., Zheng, C. & Shi, B. An extrapolation method for boundary conditions in lattice Boltzmann method. *Physics of fluids* **14**, 2007 (2002).
152. Hirt, C. W., Amsden, A. A. & Cook, J. An arbitrary Lagrangian–Eulerian computing method for all flow speeds. *Journal of computational physics* **14**, 227 (1974).

153. Persson, P.-O., Bonet, J. & Peraire, J. Discontinuous Galerkin solution of the Navier–Stokes equations on deformable domains. *Computer Methods in Applied Mechanics and Engineering* **198**, 1585 (2009).
154. Berndt, M., Breil, J., Galera, S., Kucharik, M., Maire, P.-H. & Shashkov, M. Two-step hybrid conservative remapping for multimaterial arbitrary Lagrangian–Eulerian methods. *Journal of Computational Physics* **230**, 6664 (2011).
155. Su, X., Cao, Y. & Zhao, Y. An unstructured mesh arbitrary Lagrangian–Eulerian unsteady incompressible flow solver and its application to insect flight aerodynamics. *Physics of Fluids* **28**, 061901 (2016).
156. Boscheri, W. & Dumbser, M. Arbitrary-Lagrangian–Eulerian Discontinuous Galerkin schemes with a posteriori subcell finite volume limiting on moving unstructured meshes. *Journal of Computational Physics* **346**, 449 (2017).
157. Jin, P., Deng, X. & Xiao, F. An ALE formulation for compressible flows based on multi-moment finite volume method. *Engineering Applications of Computational Fluid Mechanics* **12**, 791 (2018).
158. Meldi, M., Vergnault, E. & Sagaut, P. An arbitrary Lagrangian–Eulerian approach for the simulation of immersed moving solids with Lattice Boltzmann Method. *Journal of Computational Physics* **235**, 182 (2013).
159. Saadat, M. H. & Karlin, I. V. Arbitrary Lagrangian–Eulerian formulation of lattice Boltzmann model for compressible flows on unstructured moving meshes. *Physics of Fluids* **32**, 046105 (2020).
160. Mattila, K. K., Philippi, P. C. & Hegele Jr, L. A. High-order regularization in lattice-Boltzmann equations. *Physics of Fluids* **29**, 046103 (2017).
161. Bösch, F., Chikatamarla, S. S. & Karlin, I. V. Entropic multirelaxation lattice Boltzmann models for turbulent flows. *Physical Review E* **92**, 043309 (2015).
162. Thomas, P. D. & Lombard, C. K. Geometric conservation law and its application to flow computations on moving grids. *AIAA journal* **17**, 1030 (1979).
163. Deng, X., Mao, M., Tu, G., Liu, H. & Zhang, H. Geometric conservation law and applications to high-order finite difference schemes with stationary grids. *Journal of Computational Physics* **230**, 1100 (2011).

164. Abe, Y., Nonomura, T., Iizuka, N. & Fujii, K. Geometric interpretations and spatial symmetry property of metrics in the conservative form for high-order finite-difference schemes on moving and deforming grids. *Journal of Computational Physics* **260**, 163 (2014).
165. Zhang, J.-d. & Huang, W.-X. On the role of vortical structures in aerodynamic performance of a hovering mosquito. *Physics of Fluids* **31**, 051906 (2019).
166. Zheng, Z. C. & Wei, Z. Study of mechanisms and factors that influence the formation of vortical wake of a heaving airfoil. *Physics of Fluids* **24**, 103601 (2012).
167. Jones, K., Dohring, C. & Platzer, M. Experimental and computational investigation of the Knoller-Betz effect. *AIAA journal* **36**, 1240 (1998).
168. Bratt, J. *Flow patterns in the wake of an oscillating aerofoil* 2773 (HM Stationery Office UK, 1953).
169. Heathcote, S. & Gursul, I. Jet switching phenomenon for a periodically plunging airfoil. *Physics of Fluids* **19**, 027104 (2007).
170. Liang, C., Ou, K., Premasathan, S., Jameson, A. & Wang, Z. High-order accurate simulations of unsteady flow past plunging and pitching airfoils. *Computers & Fluids* **40**, 236 (2011).
171. Calderon, D., Cleaver, D., Gursul, I. & Wang, Z. On the absence of asymmetric wakes for periodically plunging finite wings. *Physics of Fluids* **26**, 349 (2014).
172. Martín-Alcántara, A., Fernández-Feria, R. & Sanmiguel-Rojas, E. Vortex flow structures and interactions for the optimum thrust efficiency of a heaving airfoil at different mean angles of attack. *Physics of Fluids* **27**, 073602 (2015).
173. Deng, J., Sun, L., Teng, L., Pan, D. & Shao, X. The correlation between wake transition and propulsive efficiency of a flapping foil: A numerical study. *Physics of Fluids* **28**, 094101 (2016).
174. Sangwan, J., Sengupta, T. K. & Suchandra, P. Investigation of compressibility effects on dynamic stall of pitching airfoil. *Physics of Fluids* **29**, 076104 (2017).
175. Koochesfahani, M. M. Vortical patterns in the wake of an oscillating airfoil. *AIAA journal* **27**, 1200 (1989).
176. Bohl, D. G. & Koochesfahani, M. M. MTV measurements of the vortical field in the wake of an airfoil oscillating at high reduced frequency. *Journal of Fluid Mechanics* **620**, 63 (2009).



177. Young, J. & S. Lai, J. C. Oscillation frequency and amplitude effects on the wake of a plunging airfoil. *AIAA journal* **42**, 2042 (2004).
178. Li, X., Feng, L.-H. & Li, Z.-Y. Flow mechanism for the effect of pivot point on the aerodynamic characteristics of a pitching airfoil and its manipulation. *Physics of Fluids* **31**, 087108 (2019).
179. Chyu, W., Davis, S. & Chang, K. S. Calculation of unsteady transonic flow over an airfoil. *AIAA Journal* **19**, 684 (1981).
180. Mittal, S. Finite element computation of unsteady viscous compressible flows. *Computer Methods in Applied Mechanics and Engineering* **157**, 151 (1998).
181. Shu, C.-W. in *High-order methods for computational physics* 439 (Springer, 1999).
182. Subramaniam, A., Wong, M. L. & Lele, S. K. A high-order weighted compact high resolution scheme with boundary closures for compressible turbulent flows with shocks. *Journal of Computational Physics* **397**, 108822 (2019).
183. Fu, L., Hu, X. Y. & Adams, N. A. A new class of adaptive high-order targeted ENO schemes for hyperbolic conservation laws. *Journal of Computational Physics* **374**, 724 (2018).
184. Fu, L. A very-high-order TENO scheme for all-speed gas dynamics and turbulence. *Computer Physics Communications* **244**, 117 (2019).
185. Haga, T. & Kawai, S. On a robust and accurate localized artificial diffusivity scheme for the high-order flux-reconstruction method. *Journal of Computational Physics* **376**, 534 (2019).
186. Visbal, M. & Gaitonde, D. *Shock capturing using compact-differencing-based methods* in *43rd AIAA Aerospace Sciences Meeting and Exhibit* (2005), 1265.
187. Lee, S., Lele, S. K. & Moin, P. Eddy shocklets in decaying compressible turbulence. *Physics of Fluids A: Fluid Dynamics* **3**, 657 (1991).
188. Mansour, N. & Wray, A. Decay of isotropic turbulence at low Reynolds number. *Physics of Fluids* **6**, 808 (1994).
189. Johnsen, E., Larsson, J., Bhagatwala, A. V., Cabot, W. H., Moin, P., Olson, B. J., Rawat, P. S., Shankar, S. K., Sjögreen, B., Yee, H. C., *et al.* Assessment of high-resolution methods for numerical simulations of compressible turbulence with shock waves. *Journal of Computational Physics* **229**, 1213 (2010).

190. Kumar, G., Girimaji, S. S. & Kerimo, J. WENO-enhanced gas-kinetic scheme for direct simulations of compressible transition and turbulence. *Journal of Computational Physics* **234**, 499 (2013).
191. Tanaka, K., Watanabe, T., Nagata, K., Sasoh, A., Sakai, Y. & Hayase, T. Amplification and attenuation of shock wave strength caused by homogeneous isotropic turbulence. *Physics of Fluids* **30**, 035105 (2018).
192. Cao, G., Pan, L. & Xu, K. Three dimensional high-order gas-kinetic scheme for supersonic isotropic turbulence I: criterion for direct numerical simulation. *Computers & Fluids* **192**, 104273 (2019).
193. Chen, T., Wen, X., Wang, L.-P., Guo, Z., Wang, J. & Chen, S. Simulation of three-dimensional compressible decaying isotropic turbulence using a redesigned discrete unified gas kinetic scheme. *Physics of Fluids* **32**, 125104 (2020).
194. Meyer, D. W. & Eggersdorfer, M. L. Simulating particle collisions in homogeneous turbulence with kinematic simulation – A validation study. *Colloids and Surfaces A: Physicochemical and Engineering Aspects* **454**, 57 (2014).
195. Fang, J., Yao, Y., Li, Z. & Lu, L. Investigation of low-dissipation monotonicity-preserving scheme for direct numerical simulation of compressible turbulent flows. *Computers & Fluids* **104**, 55 (2014).
196. Garnier, E., Mossi, M., Sagaut, P., Comte, P. & Deville, M. On the use of shock-capturing schemes for large-eddy simulation. *Journal of Computational Physics* **153**, 273 (1999).
197. Sun, C. Lattice-Boltzmann models for high speed flows. *Physical review E* **58**, 7283 (1998).
198. Di Staso, G., Clercx, H., Succi, S. & Toschi, F. Lattice Boltzmann accelerated direct simulation Monte Carlo for dilute gas flow simulations. *Philosophical Transactions of the Royal Society A: Mathematical, Physical and Engineering Sciences* **374**, 20160226 (2016).
199. Kallikounis, N., Dorschner, B. & Karlin, I. Multiscale semi-Lagrangian lattice Boltzmann method. *Physical Review E* **103**, 063305 (2021).
200. Reyhanian, E., Dorschner, B. & Karlin, I. V. Thermokinetic lattice Boltzmann model of nonideal fluids. *Physical Review E* **102**, 020103 (2020).
201. Mott-Smith, H. M. The solution of the Boltzmann equation for a shock wave. *Physical Review* **82**, 885 (1951).

202. Alsmeyer, H. Density profiles in argon and nitrogen shock waves measured by the absorption of an electron beam. *Journal of Fluid Mechanics* **74**, 497 (1976).
203. Greenshields, C. J. & Reese, J. M. The structure of shock waves as a test of Brenner's modifications to the Navier–Stokes equations. *Journal of Fluid Mechanics* **580**, 407 (2007).
204. Timokhin, M. Y., Struchtrup, H., Kokhanchik, A. & Bondar, Y. A. Different variants of R13 moment equations applied to the shock-wave structure. *Physics of Fluids* **29**, 037105 (2017).
205. Paolucci, S. & Paolucci, C. A second-order continuum theory of fluids. *Journal of Fluid Mechanics* **846**, 686 (2018).
206. Ohwada, T. Structure of normal shock waves: Direct numerical analysis of the Boltzmann equation for hard-sphere molecules. *Physics of Fluids A: Fluid Dynamics* **5**, 217 (1993).
207. Vuorinen, V., Yu, J., Tirunagari, S., Kaario, O., Larmi, M., Duwig, C. & Boersma, B. Large-eddy simulation of highly underexpanded transient gas jets. *Physics of Fluids* **25**, 016101 (2013).
208. Larsson, J. & Lele, S. K. Direct numerical simulation of canonical shock/turbulence interaction. *Physics of fluids* **21**, 126101 (2009).
209. Hickel, S., Egerer, C. P. & Larsson, J. Subgrid-scale modeling for implicit large eddy simulation of compressible flows and shock-turbulence interaction. *Physics of Fluids* **26**, 106101 (2014).
210. Pirozzoli, S., Bernardini, M. & Grasso, F. Direct numerical simulation of transonic shock/boundary layer interaction under conditions of incipient separation. *Journal of Fluid Mechanics* **657**, 361 (2010).
211. Agostini, L., Larchevêque, L. & Dupont, P. Mechanism of shock unsteadiness in separated shock/boundary-layer interactions. *Physics of Fluids* **27**, 126103 (2015).



## COPYRIGHT DISCLAIMER

---

- Chapter 3 is partially reprinted from Saadat, Bösch & Karlin [87], Saadat, Dorschner & Karlin [102] and Saadat *et al.* [100].
- Chapter 4 is partially reprinted from Saadat, Bösch & Karlin [87] and Saadat *et al.* [100].
- Chapter 5 is partially reprinted from Saadat, Bösch & Karlin [107] and Saadat & Karlin [159].
- Chapter 6 is partially reprinted from Saadat *et al.* [100].